Dynamical Instabilities and High-Temperature Phase Stability in Ionic Crystals

by

Min-Hua Chen

A dissertation submitted in partial fulfillment
of the requirements for the degree of
Doctor of Philosophy
(Materials Science and Engineering)
in The University of Michigan
2015

Doctoral Committee:

Adjunct Professor Anton Van der Ven, Co-chair
Professor Katusyo S. Thornton, Co-chair
Professor John E. Allison
Professor Krishnakumar R. Garikipati
Assistant Professor Donald J. Siegel

ACKNOWLEDGEMENTS

I would like to begin by expressing my gratitude to my advisor Professor Anton Van der Ven for his guidance, patience, and most of all encouragement. Despite moments where I was less than enthusiastic about my research, his excitement always brought me back to point. I have truly learned a great deal these past few years.

I am also grateful to Professor Katsuyo Thornton for not only agreeing to be my co-chair, but also wholeheartedly committing time and effort to providing me with valuable feedback. My committee members Professors John Allison, Krishna Garikipati, and Donald Siegel have also been incredibly generous with their time, comments, and suggestions.

Much of this research would not have been possible without the insights and contributions of Dr. John C. Thomas. He has been a remarkable and supportive mentor over the years and is generally also fun to talk to. I must without a doubt thank past and current members of the Van der Ven group, including Drs. Anna Belak, Donghee Chang and Alex Emly for making this experience as enjoyable and educational as it was. I would also like to thank Dr. Alex Emly in particular for her contributions to the work on Li_3OCl and Dr. Brian Puchala for his help with the work on the Zr-O system. I thank Stefan Heinze here at UCSB for useful discussions on ferroelastic toughening. I would surely have lost my sanity if not for my office mates here at UCSB: John Goiri, Anirudh Raju Natarajan, Elizabeth Decolvenaere, and Michael Chu. Because of them, our working environment was the perfect balance of knowledge, exotic snacks, and sass. I thank Anirudh for his help with the work involving strains, and John Goiri for being a truly supportive friend, especially in this last difficult stretch.

My friends Smriti, Dev, Shalini, Nour, Rahul, and Varun made the long Ann Arbor winters more than bearable. If they had not insisted on periodically dragging me out of my hibernation, I might have sunk deep into depression.

Renée Hilgendorf has made doing everything remotely from California infinitely easier, and I thank her for patiently dealing with all my e-mails, requests, and paperwork. The staff at Rackham has also been extremely supportive and responsive. I thank Denise Edmund especially for her kind assistance in the recent months.

I am grateful to Milena and Valery for the kindness they have always shown me, for

welcoming me into their family, and for the generous graduation gift they gave me months in advance of my actual graduation.

Growing up, I often thought of my sisters Ellen and Jodi as impossible role models to live up to. As I got older, it became obvious that they were, and still are, two of my greatest supporters. I especially thank my parents for their daring trust and unwavering support of me and my decisions, even when I was younger. Through his work, my dad sparked an early curiosity of materials science. I also certainly would not have gone into a computational field if it were not for my mom. As a programmer herself, she encouraged me early on to learn programming, just in case I might need it some day.

Despite the difficulties of a long distance relationship, I am thankful every day to have Nasko in my life. His love, optimism, and humor have drawn me out of my darkest moments, and I am ecstatic about the possibilities of our future together.

TABLE OF CONTENTS

LIST OF FIGURES

Figure

LIST OF APPENDICES

Appendix

ABSTRACT

Dynamical Instabilities and High-Temperature Phase Stability in Ionic Crystals
by
Min-Hua Chen

Co-Chairs: Anton Van der Ven and Katsuyo S. Thornton

A large class of high-temperature phases become dynamically unstable at low temperatures and transform to lower symmetry phases upon cooling. In this thesis we seek to understand the energetics and vibrational thermodynamic properties associated with these transformation mechanisms in a variety of technologically important materials, including a newly discovered battery solid electrolyte, oxide phases in nuclear rod cladding, and thermal barrier coatings.

Using first-principles phonon calculations, we examine the dynamical stability and vibrational properties of Li_3OCl, a solid electrolyte material. We show that it is dynamically unstable with respect to octahedral rotations. Further examination of the anharmonic energy landscapes resulting from these rotations revealed that while rotations can lead to lower symmetry structures, the energy gained by these rotations are small. At low temperatures, the cubic form should persist due to anharmonic vibrational excitations. We also find that Li_3OCl is entropically stabilized with respect to LiCl and Li_2O at temperatures above 480 K.

Zirconium alloys used in nuclear fuel rod cladding experience corrosive and oxidizing environments. Understanding the phase stability of these oxide phases at high temperatures is crucial to designing corrosion-resistant materials. Vibrational free energies for several Zr-O compounds were calculated and incorporated into a previously calculated temperature composition phase diagram [1] to identify the temperature stability limit of the recently identified δ'-ZrO phase. We show that this phase is stable well beyond typical nuclear reactor temperatures.

Instabilities observed in cubic, tetragonal, and monoclinic ZrO_2 are also studied. The cubic instability leads to a transformation into the tetragonal phase. A volume-induced

instability in the tetragonal phase results in a transformation into a new orthorhombic phase. This instability has implications for the finite temperature stability of tetragonal ZrO_2 and the role of anharmonicity in high-temperature materials. Strain is shown to affect stabilities of the three tetragonal variants, as well as the relative stabilities of the tetragonal and monoclinic phases. These results suggest that strain can stabilize the high-temperature tetragonal phase, which is preferable for epitaxial thin films used in high-k dielectrics and for ferroelastic toughening in thermal barrier coatings.

CHAPTER I

Introduction

Introduction to materials science often begins with descriptions of atomic bonds and rigid crystal structures. In higher-level academic research, well-developed cluster expansion models [2–4], based on atomic occupancies on a periodic crystal lattice, are a rigorous way to account for configurational degrees of freedom. Combining these descriptions with statistical mechanics result in useful thermodynamic properties. To an extent, these models reinforce the notion of atoms sitting statically on specific crystal lattice sites. In reality, due to thermal energy at finite temperatures, atoms are in fact vibrating about their equilibrium positions. As temperature increases, the effect of these collective atomic movements, or phonons, on the thermodynamic properties and stabilities of materials increases as well. The underlying physics and thermodynamics arising from these vibrations as calculated by first principles can be used to study phase stabilities and phase transformations of materials with a broad range of applications. These techniques and principles will be used in this thesis to study the dynamical instabilities and phase stabilities of ionic materials used as Li-ion solid electrolytes, nuclear fuel rod cladding, or thermal barrier coatings.

Experimentally, inelastic neutron scattering measurements can provide a full description of phonon frequencies in the Brillouin zone resulting from these oscillations, but this technique requires large single-crystal specimen, which are not always possible to obtain [5]. Computational techniques can conveniently complement this experimental limitation. Atomic-scale modeling methods, such as first-principles calculations, are especially appropriate for modeling perturbations at this level, and the methodology will be reviewed in Chapter II.

First-principles calculations alone are able to provide information such as the energy of a static arrangement of atoms, or configuration, at zero Kelvin. Although these calculations can optimize the structure and minimize the energy of a material through an iterative, self-consistent process, the system may ultimately land on a saddle point of the energy landscape. Such a structure is considered to be dynamically unstable, as symmetry breaking distortions can push the system into a lower energy phase. Phonon studies can be used to

verify the presence of these dynamical instabilities. Inspection of the atomic displacement fields associated with these instabilities can also provide insight into how certain phase transformations occur.

Occasionally, first-principles calculations will predict an experimentally known compound that is stable at low temperatures to be metastable. While this result may be due to a fundamental deficiency in the first-principles description for this material, another possibility is that the material is entropically stabilized by phonons. Antiperovskite Li_3OCl, a solid electrolyte material [6], is an example. Although this material is predicted to be metastable at 0 K [7], it is experimentally stable at room temperatures. Using phonon calculations, we found that Li_3OCl is dynamically unstable with respect to octahedral rotations, and the energy landscape with respect to these rotational degrees of freedom is highly anharmonic. Our work also shows that Li_3OCl is vibrationally stabilized at temperatures above 480 K, which is consistent with the experimental synthesis temperatures of $330 - 360°C$ [6]. These results will be presented in Chapter III and have been previously published in *Physical Review B* [8].

At elevated temperatures, vibrational entropy begins to play a larger role in the relative phase stabilities of materials. In certain phases with near zero configurational disorder, such as line compounds, finite temperature vibrational effects dominate and determine their stabilities relative to neighboring phases. This is a concept around which Chapter IV is built, where we examine the stability of a recently identified δ'-ZrO phase [1] within the broader context of oxides in the Zr-O system. This system is of interest as zirconium alloys are used as nuclear fuel rod cladding and are subjected to harsh high-temperature and oxidizing environments [9, 10]. Using phonons to understand the high-temperature stability of δ'-ZrO is therefore important to engineering oxidation-resistant alloys. We also updated a previously published Zr-O temperature-composition phase diagram based on a cluster expansion Hamiltonian and Monte Carlo calculations [1] to include the effects of vibrational entropy.

As part of our Zr-O study, we also used vibrational free energies to predict the phase transition temperature of monoclinic to tetragonal ZrO_2. Further study of the three main ZrO_2 polymorphs (cubic, tetragonal, and monoclinic) showed that in addition to the well-known mechanical instability of the cubic phase [11–16], instabilities in the mechanically stable tetragonal [14–16] and monoclinic phases [15, 16] can be triggered by factors such as volume increases or strain. The volume-induced instability of tetragonal ZrO_2 resulted in the discovery of a new orthorhombic ZrO_2 phase. As the high-temperature tetragonal and cubic phases are often more desirable for applications in memory storage devices and thermal barrier coatings, understanding the effects of volume or strain on their stabilities

can ultimately aid and inform engineering efforts of these materials. The details of these different types of instabilities are presented in Chapter V.

Chapter VI discusses results on stable phases that are formed during intercalation of Li into trirutile $LiFe_2F_6$, a cathode material for Li-ion batteries. Using a cluster expansion Hamiltonian and Monte Carlo calculations, an intercalation voltage curve was calculated and intermediate stable phases were identified. Li diffusion barriers in the dilute limit were also calculated, and the Li diffusion behavior is discussed.

Lastly, Chapter VII summarizes the key findings in this thesis and identifies future research directions in these material systems.

CHAPTER II

Theoretical Background and Computational Methods

2.1 Phonons

2.1.1 Harmonic Approximation

Phonons are the cooperative motion of atoms in a crystal due to thermal excitations. These small vibrations of atoms around their equilibrium position can be modeled as a collection of atoms connected by springs. Considering that the classic potential energy of a molecule being separated as a function of separation distance is close to parabolic near the equilibrium separation distance, the potential energy of these small atomic vibrations can be modeled with a parabolic energy surface. This approach is known as the harmonic approximation, which is well established, extensively studied [5, 17–19] and implemented [12, 20–22]. An overview of the theory behind the harmonic approximation will be provided here.

The harmonic approximation model is constructed within the Born Oppenheimer approximation [23], where the movement of electrons and ions is treated separately due to the mass differences. Only the movement of the ions are considered, while the electrons are neglected as the electronic wave functions are expected to relax instantaneously into their ground state in response to changes in its environment. Beginning with a static, periodic arrangement of atoms at zero K with an equilibrium potential energy Φ_0, any perturbations from the equilibrium atomic positions due to finite temperature vibrations will result in a change in the Born Oppenheimer energy surface. A general description of the potential energy due to lattice vibrations can be obtained through a Taylor expansion with respect to deviations of

the atoms from their equilibrium positions

$$\begin{aligned}\Phi &= \Phi_0 + \sum_{lb\alpha} \left.\frac{\partial \Phi}{\partial \mathbf{u}_\alpha^b\left(\mathbf{R}_l\right)}\right|_0 \mathbf{u}_\alpha^b\left(\mathbf{R}_l\right) \\ &\quad + \frac{1}{2}\sum_{ll'}\sum_{bb'}\sum_{\alpha\beta} \left.\frac{\partial^2 \Phi}{\partial \mathbf{u}_\alpha^b\left(\mathbf{R}_l\right)\partial \mathbf{u}_\beta^{b'}\left(\mathbf{R}_{l'}\right)}\right|_0 \mathbf{u}_\alpha^b\left(\mathbf{R}_l\right)\mathbf{u}_\beta^{b'}\left(\mathbf{R}_{l'}\right) + \cdots \end{aligned} \tag{2.1}$$

$$\begin{aligned} &= \Phi_0 + \sum_{lb\alpha} \Phi_\alpha^b\left(\mathbf{R}_l\right)\mathbf{u}_\alpha^b\left(\mathbf{R}_l\right) \\ &\quad + \frac{1}{2}\sum_{ll'}\sum_{bb'}\sum_{\alpha\beta} \Phi_{\alpha\beta}^{bb'}\left(\mathbf{R}_l,\mathbf{R}_{l'}\right)\mathbf{u}_\alpha^b\left(\mathbf{R}_l\right)\mathbf{u}_\beta^{b'}\left(\mathbf{R}_{l'}\right) + \cdots, \end{aligned} \tag{2.2}$$

where a truncation after the second order term is applied, limiting the description to pairs and maintaining a parabolic energy landscape description. When anharmonicity is accounted for, higher order couplings are required. The crystal described here is composed of N unit cells indexed by l and l'. The n number of basis atoms within each unit cell are likewise indexed by b and b'. The indices α and β represent the x, y, z Cartesian directions. The position of an atom in the unperturbed crystal is defined by the position of the unit cell $\mathbf{R}_l$ to which it belongs, as well as the shift vector $\boldsymbol{\tau}_b$ representing its position within the unit cell. The perturbation of basis atom b in unit cell l from its equilibrium position $\mathbf{R}_l + \boldsymbol{\tau}_b$ is represented by $\mathbf{u}_\alpha^b\left(\mathbf{R}_l\right)$.

Each term in the Taylor expansion above is evaluated at the equilibrium configuration. The first order term $\Phi_\alpha^b\left(\mathbf{R}_l\right)$ represents the negative of the α-th component of the force felt by the atom at $\mathbf{R}_l + \boldsymbol{\tau}_i$. At equilibrium, there are no forces, resulting in the elimination of this term in the overall potential energy expression. The partial derivative in the second order term is defined as

$$\left.\frac{\partial^2 \Phi}{\partial \mathbf{u}_\alpha^b\left(\mathbf{R}_l\right)\partial \mathbf{u}_\beta^{b'}\left(\mathbf{R}_{l'}\right)}\right|_0 = \Phi_{\alpha\beta}^{bb'}\left(\mathbf{R}_l,\mathbf{R}_{l'}\right), \tag{2.3}$$

and this is the inter-atomic force constant that relates the force felt by an atom at $\mathbf{R}_{l'} + \boldsymbol{\tau}_{b'}$ due to a perturbation imposed on atom $\mathbf{R}_l + \boldsymbol{\tau}_b$. This relationship can be seen more clearly by taking the derivative of the Taylor-expanded potential energy in Equation 2.2

$$\frac{\partial \Phi}{\partial \mathbf{u}_\alpha^b\left(\mathbf{R}_l\right)} = \sum_{l'b'\beta} \Phi_{\alpha\beta}^{bb'}\left(\mathbf{R}_l,\mathbf{R}_{l'}\right)\mathbf{u}_\beta^{b'}\left(\mathbf{R}_{l'}\right), \tag{2.4}$$

from which we see a more explicit interpretation of the force constant as the spring constant that relates the force felt on an atom at $\mathbf{R}_l + \boldsymbol{\tau}_b$ due to a perturbation of an atom at $\mathbf{R}_{l'} + \boldsymbol{\tau}_{b'}$.

Using this potential energy description, the phonon Hamiltonian can be expressed as

$$H = \Phi_0 + \frac{1}{2}\sum_{lb\alpha} M_b \left[\dot{\mathbf{u}}^b_\alpha(\mathbf{R}_l)\right]^2 + \frac{1}{2}\sum_{ll'}\sum_{bb'}\sum_{\alpha\beta}\Phi^{bb'}_{\alpha\beta}(\mathbf{R}_l,\mathbf{R}_{l'})\,\mathbf{u}^b_\alpha(\mathbf{R}_l)\,\mathbf{u}^{b'}_\beta(\mathbf{R}_{l'}). \tag{2.5}$$

There are three distinct terms, corresponding to the static lattice, kinetic, and potential energies, respectively. The mass of basis atom b in the kinetic energy is represented as M_b. This Hamiltonian describes the crystal as a system of coupled harmonic oscillators, manifested in the coupling between perturbations at different sites, $\mathbf{u}^b_\alpha(\mathbf{R}_l)$ and $\mathbf{u}^{b'}_\beta(\mathbf{R}_{l'})$. By performing a diagonalization, this complex description can be simplified into a system of decoupled harmonic oscillators. To accomplish this, we begin by defining the Fourier transform of the displacements $\mathbf{u}^b_\alpha(\mathbf{R}_l)$ and $\mathbf{u}^{b'}_\beta(\mathbf{R}_{l'})$ as

$$\tilde{\mathbf{u}}^b_\alpha(\mathbf{k}) = \frac{1}{\sqrt{NM_b}}\sum_l \mathbf{u}^b_\alpha(\mathbf{R}_l)\exp\left[i\mathbf{k}\cdot(\mathbf{R}_l+\boldsymbol{\tau}_b)\right] \tag{2.6}$$

$$\tilde{\mathbf{u}}^{b'}_\beta\left(\mathbf{k}'\right) = \frac{1}{\sqrt{NM_{b'}}}\sum_{l'} \mathbf{u}^{b'}_\beta(\mathbf{R}_{l'})\exp\left[i\mathbf{k}'\cdot(\mathbf{R}_{l'}+\boldsymbol{\tau}_{b'})\right], \tag{2.7}$$

where a discretized sum is performed over each unit cell. The inverse Fourier transform can be expressed in terms of the Fourier transforms $\tilde{\mathbf{u}}^b_\alpha(\mathbf{k})$ and $\tilde{\mathbf{u}}^{b'}_\beta(\mathbf{k})$ according to

$$\mathbf{u}^b_\alpha(\mathbf{R}_l) = \frac{1}{\sqrt{NM_b}}\sum_k \tilde{\mathbf{u}}^b_\alpha(\mathbf{k})\exp\left[-i\mathbf{k}\cdot(\mathbf{R}_l+\boldsymbol{\tau}_b)\right] \tag{2.8}$$

$$\mathbf{u}^b_\beta(\mathbf{R}_{l'}) = \frac{1}{\sqrt{NM_{b'}}}\sum_{k'} \tilde{\mathbf{u}}^{b'}_\beta(\mathbf{k})\exp\left[-i\mathbf{k}'\cdot(\mathbf{R}_{l'}+\boldsymbol{\tau}_{b'})\right]. \tag{2.9}$$

The perturbations are expressed as a superposition of plane waves, where $\tilde{\mathbf{u}}(\mathbf{k})$ are the amplitudes of waves having wavelength $\lambda = \frac{2\pi}{|\mathbf{k}|}$. These perturbations can be substituted into both the kinetic and potential energy terms in the Hamiltonian to fully diagonalize the Hamiltonian. The potential energy term of our Hamiltonian upon this substitution is then

$$\begin{aligned}\frac{1}{2N}\sum_{ll'}\sum_{bb'}\sum_{\alpha\beta}\sum_{kk'}\frac{1}{\sqrt{M_bM_{b'}}}\Phi^{bb'}_{\alpha\beta}(\mathbf{R}_l,\mathbf{R}_{l'})\tilde{\mathbf{u}}^b_\alpha(\mathbf{k})\exp\left[-i\mathbf{k}\cdot(\mathbf{R}_l+\boldsymbol{\tau}_b)\right]\\ \tilde{\mathbf{u}}^{b'}_\beta\left(\mathbf{k}'\right)\exp\left[-i\mathbf{k}'\cdot(\mathbf{R}_{l'}+\boldsymbol{\tau}_{b'})\right].\end{aligned} \tag{2.10}$$

A change of variables can be performed, where we utilize the observation that the force constants $\Phi^{bb'}_{\alpha\beta}(\mathbf{R}_l,\mathbf{R}_{l'})$ depend only on the relative distance defined by $\mathbf{R}_{l''} = \mathbf{R}_{l'} - \mathbf{R}_l$ since the crystal is periodic. This allows for the elimination of index l, after which exponential

terms with the same $\mathbf{R}$ vectors can be grouped together

$$\frac{1}{2N}\sum_{l''}\sum_{bb'}\sum_{\alpha\beta}\sum_{kk'}\frac{1}{\sqrt{M_bM_{b'}}}\Phi_{\alpha\beta}^{bb'}\left(0,\mathbf{R}_{l''}\right)\tilde{\mathbf{u}}_{\alpha}^{b}\left(\mathbf{k}\right)\tilde{\mathbf{u}}_{\beta}^{b'}\left(\mathbf{k}^{'}\right)\exp\left[i\mathbf{k}\cdot\left(\mathbf{R}_{l''}-\boldsymbol{\tau}_b\right)-i\mathbf{k}'\boldsymbol{\tau}_{b'}\right]$$
$$\sum_{l'}\exp\left[-i\left(\mathbf{k}+\mathbf{k}'\right)\cdot\left(\mathbf{R}_{l'}+\boldsymbol{\tau}_{b'}\right)\right]. \tag{2.11}$$

All the terms dependent on l' have been gathered within the same sum, and we note that the sum over l' at the end is a delta function $N\delta\left(\mathbf{k}+\mathbf{k}'\right)=1$. Only terms $-\mathbf{k}=\mathbf{k}'$ survive, allowing further simplification of the expression as

$$\frac{1}{2}\sum_{k}\sum_{bb'}\sum_{\alpha\beta}\tilde{\mathbf{u}}_{\alpha}^{b}\left(-\mathbf{k}\right)\tilde{\mathbf{u}}_{\beta}^{b'}\left(\mathbf{k}\right)\frac{1}{\sqrt{M_bM_{b'}}}\sum_{l''}\Phi_{\alpha\beta}^{bb'}\left(0,\mathbf{R}_{l''}\right)\exp\left[i\mathbf{k}\cdot\left(\mathbf{R}_{l''}+\boldsymbol{\tau}_{b'}-\boldsymbol{\tau}_b\right)\right]. \tag{2.12}$$

By performing this mathematical manipulation, we have transformed the expression from real space to reciprocal space. In doing so, the potential energy is fully diagonalized and all coupled terms are eliminated. More importantly, the double sum at the end of this expression is the Fourier transform of the force constant, which is a quantity known as the dynamical matrix

$$D_{\alpha\beta}^{bb'}\left(\mathbf{k}\right)=\frac{1}{\sqrt{M_bM_{b'}}}\sum_{l''}\Phi_{\alpha\beta}^{bb'}\left(0,\mathbf{R}_{l''}\right)\exp\left[i\mathbf{k}\cdot\left(\mathbf{R}_{l''}+\boldsymbol{\tau}_{b'}-\boldsymbol{\tau}_b\right)\right]. \tag{2.13}$$

A similar diagonalization procedure can be performed on the kinetic energy term as well, such that the kinetic energy is also in reciprocal space

$$\frac{1}{2}\sum_{lb\alpha}M_b\left[\dot{\mathbf{u}}_{\alpha}^{b}\left(\mathbf{R}_l\right)\right]^2=\frac{1}{2}\sum_{kb\alpha}\dot{\tilde{\mathbf{u}}}_{\alpha}^{b}\left(-\mathbf{k}\right)\dot{\tilde{\mathbf{u}}}_{\alpha}^{b}\left(\mathbf{k}\right). \tag{2.14}$$

This process ultimately results in a fully diagonalized Hamiltonian

$$H=\Phi_0+\frac{1}{2}\sum_{k}\left[\sum_{b\alpha}\dot{\tilde{\mathbf{u}}}_{\alpha}^{b}\left(-\mathbf{k}\right)\dot{\tilde{\mathbf{u}}}_{\alpha}^{b}\left(\mathbf{k}\right)+\sum_{bb'}\sum_{\alpha\beta}\tilde{\mathbf{u}}_{\alpha}^{b}\left(-\mathbf{k}\right)\tilde{\mathbf{u}}_{\beta}^{b'}\left(\mathbf{k}\right)D_{\alpha\beta}^{bb'}\left(\mathbf{k}\right)\right], \tag{2.15}$$

where the same system of coupled harmonic oscillators is now described as decoupled harmonic oscillators, one for each wave number k, where the fluctuating variable is the amplitude of a collective sinusoidal vibrational mode with wavelength $\lambda=\frac{2\pi}{|\mathbf{k}|}$. These collective modes are called phonons.

Equation 2.15 can be further diagonalized to obtain frequencies $\omega_v(\mathbf{k})$,

$$\sum_{b'\beta} D^{bb'}_{\alpha\beta}(\mathbf{k})\,\mathbf{e}^{b'}_{\beta v}(\mathbf{k}) = \omega^2_v(\mathbf{k})\,\mathbf{e}^{b}_{\alpha v}(\mathbf{k}), \tag{2.16}$$

where $\mathbf{e}(\mathbf{k})$ and $\omega^2_v(\mathbf{k})$ are the eigenvectors and eigenvalues and v indexes the phonon branches. The eigenvectors of the dynamical matrix determine the direction in which the atoms are displaced by a particular mode. In addition, as the expression shows, the frequencies are simply the square root of the eigenvalues. While it is common to write the eigenvalue problem in terms of the angular frequency ω, dispersion curves are conventionally expressed in plain frequencies, ν, which is related to the angular frequency by a factor of 2π. Other unit conversion details needed for the implementation can be found in Appendix A.4.

The diagonalized Hamiltonian can be further expressed in terms of normal coordinates $\xi_v(\mathbf{k})$. The perturbations $\mathbf{u}(\mathbf{R})$ in terms of normal coordinates and eigenvectors of the dynamical matrix is

$$\mathbf{u}^b_\alpha(\mathbf{R}_l) = \frac{1}{\sqrt{NM_b}} \sum_{kv} \mathbf{e}^b_{\alpha v}(\mathbf{k})\,\xi_v(\mathbf{k}) \exp\left[-i\mathbf{k}\cdot(\mathbf{R}_l + \boldsymbol{\tau}_b)\right], \tag{2.17}$$

which in turn gives mode amplitudes of the form

$$\tilde{\mathbf{u}}^b_\alpha(\mathbf{k}) = \sum_v \mathbf{e}^b_{\alpha v}(\mathbf{k})\,\xi_v(\mathbf{k}). \tag{2.18}$$

Substituting this expression into Equation 2.15, we can express the entire Hamiltonian in terms of these normal coordinates. Performing this substitution into the potential energy term and rearranging terms results in

$$\frac{1}{2}\sum_k \sum_{vv'} \xi_v(-\mathbf{k})\,\xi_{v'}(\mathbf{k}) \sum_{b\alpha} \mathbf{e}^b_{\alpha v}(-\mathbf{k}) \left[\sum_{b'\beta} D^{bb'}_{\alpha\beta}(\mathbf{k})\,\mathbf{e}^{b'}_{\beta v'}(\mathbf{k})\right], \tag{2.19}$$

where the term in the brackets can be replaced with Equation 2.16. One last simplification can be made upon further rearrangement to obtain

$$\frac{1}{2}\sum_k \sum_{vv'} \xi_v(-\mathbf{k})\,\xi_{v'}(\mathbf{k})\left[\omega_{v'}(\mathbf{k})\right]^2 \sum_{b\alpha} \mathbf{e}^b_{\alpha v}(-\mathbf{k})\,\mathbf{e}^b_{\alpha v'}(\mathbf{k}), \tag{2.20}$$

at which point we note that the eigenvectors of the dynamical matrix are orthogonal and therefore the sum over b and α becomes a delta function $\delta_{vv'}$. Only v terms survive, resulting

in

$$\frac{1}{2}\sum_{k}\sum_{v}\xi_{v}\left(-\mathbf{k}\right)\xi_{v}\left(\mathbf{k}\right)\left[\omega_{v}\left(\mathbf{k}\right)\right]^{2}, \tag{2.21}$$

which is an expression of the potential energy term in normal coordinates. A similar process gives us a kinetic energy term similarly in terms of normal coordinates

$$\frac{1}{2}\sum_{k}\sum_{v}\dot{\xi}_{v}\left(-\mathbf{k}\right)\dot{\xi}_{v}\left(\mathbf{k}\right). \tag{2.22}$$

The entire Hamiltonian in terms of normal coordinates, which remains diagonalized, is then

$$H=\Phi_{0}+\frac{1}{2}\sum_{k}\left[\sum_{v}\dot{\xi}_{v}\left(-\mathbf{k}\right)\dot{\xi}_{v}\left(\mathbf{k}\right)+\sum_{v}\xi_{v}\left(-\mathbf{k}\right)\xi_{v}\left(\mathbf{k}\right)\left[\omega_{v}\left(\mathbf{k}\right)\right]^{2}\right], \tag{2.23}$$

a form that is used in Chapter III to estimate the total free energy of Li_3OCl. Solutions to the Schrödinger equation using this diagonalized phonon Hamiltonian results in discrete energy levels accessible to each phonon mode vibrating at frequency $\omega_{v}\left(\mathbf{k}\right)$

$$E_{v,k}=\hbar\omega_{v}\left(\mathbf{k}\right)\left(n+\frac{1}{2}\right), \tag{2.24}$$

where $n=0,1,\ldots$ are integers corresponding to discrete energy levels.

Thus far, the dynamical matrix has proved crucial in providing important information such as the vibrational frequencies and the directionality of the phonon modes, and it has several important characteristics. As each atom has 3 degrees of freedom, the entire dynamical matrix $D\left(\mathbf{k}\right)$ has dimensions of $3n\times3n$, resulting in $3n$ frequencies when evaluated at a given $\mathbf{k}$ point. At the center of the Brillouin zone, Γ, the phase factor goes to 1, and the dynamical matrix becomes a matrix of all interactomic force constants of the unit cell, where each 3×3 block corresponds to the sum of force constants connecting basis atoms b and b'. Due to the symmetry and constraints imposed on the force constants that will be discussed shortly, the dynamical matrix is also necessarily Hermitian [24]. The eigenvalues of any Hermitian matrix are by definition real, and as the frequencies $\omega_{v}\left(\mathbf{k}\right)$ are obtained by taking the square root of the eigenvalues, the frequencies can be real or imaginary. Real frequencies correspond to a phonon mode with an energy landscape that has positive curvature, as in a parabolic energy surface. Imaginary frequencies, on the other hand, correspond to phonon modes with an energy landscape of negative curvature. The presence of an imaginary or soft mode typically indicates that the crystal is mechanically unstable. A perturbation of atoms

in the equilibrium crystal in the direction of the unstable phonon mode will cause the crystal to transition into a lower energy and often lower symmetry phase. Such a phenomenon will be observed and discussed further in the context of antiperovskite Li_3OCl in Chapter III. Instabilities observed in a phonon dispersion curve can also lead to further insight into the mechanisms of displacive phase transformations. The unstable mode observed in mechanically unstable cubic ZrO_2 is known [12, 13, 25], for example, to be responsible for the transformation into a mechanically stable tetragonal ZrO_2 phase, which will be discussed in Chapter V.

2.1.2 Force Constants

One of the fundamental building blocks of the harmonic approximation is the description of atom movements as harmonic oscillators. Therefore, an accurate description of the force constants is particularly important, and there are several properties and conditions that need to be obeyed [17]. The first property is that of translational invariance, which was used in the diagonalization of the Hamiltonian. Physically, when a crystal is translated rigidly, neither the potential energy of the crystal as a whole nor the force constants should change. The effect of this constraint on the force constants can be shown by applying a translation vector, v, to the potential energy

$$\Phi = \Phi_0 + \sum_{lb\alpha} \Phi^b_\alpha \left(\mathbf{R}_l\right) v_\alpha + \frac{1}{2} \sum_{ll'} \sum_{bb'} \sum_{\alpha\beta} \Phi^{bb'}_{\alpha\beta} \left(\mathbf{R}_l, \mathbf{R}_{l'}\right) v_\alpha v_\beta + \cdots . \tag{2.25}$$

As the change to the total potential energy Φ by a simple translation is zero, the nontrivial solution results in the condition

$$\sum_{ll'} \sum_{bb'} \Phi^{bb'}_{\alpha\beta} \left(\mathbf{R}_l, \mathbf{R}_{l'}\right) = 0. \tag{2.26}$$

From this condition, we can draw from it the acoustic sum rule, which is

$$\Phi^{bb}_{\alpha\beta} \left(\mathbf{R}_l, \mathbf{R}_l\right) = - \sum_{(l'b') \neq (lb)} \Phi^{bb'}_{\alpha\beta} \left(\mathbf{R}_l, \mathbf{R}_{l'}\right). \tag{2.27}$$

The term $\Phi^{bb}_{\alpha\beta} \left(\mathbf{R}_l, \mathbf{R}_l\right)$ is the inter-atomic force constant between an atom and itself. Another property can be gleaned from Equation 2.3, where the partial differentiation is commutative and as a result we obtain the symmetry constraint [17, 26]

$$\Phi^{bb'}_{\alpha\beta} \left(\mathbf{R}_l, \mathbf{R}_{l'}\right) = \Phi^{b'b}_{\beta\alpha} \left(\mathbf{R}_{l'}, \mathbf{R}_l\right). \tag{2.28}$$

While the force constants depend only on a relative distance, the form of the force constant does depend on the directionality, as this expression shows. It states that the force constant going from site b to site b' is related to the transpose of the force constant from site b' to b. Further combining Equations 2.27 and 2.28 produces another condition, which is

$$\sum_{(l'b')\neq(lb)} \Phi^{bb'}_{\alpha\beta}\left(\mathbf{R}_l, \mathbf{R}_{l'}\right) = \sum_{(l'b')\neq(lb)} \Phi^{bb'}_{\beta\alpha}\left(\mathbf{R}_l, \mathbf{R}_{l'}\right). \tag{2.29}$$

For certain crystal symmetries, this condition may not be trivially satisfied and thus needs to be explicitly enforced [26].

Extending the concept of translational invariance, we note that when a crystal is subjected to an infinitesimal rigid body rotation, the forces do not change either. We begin by expressing the derivative of the potential as

$$\frac{\partial \Phi}{\partial \mathbf{u}^b_\alpha\left(\mathbf{R}_l\right)} = \Phi^b_\alpha\left(\mathbf{R}_l\right) + \sum_{l'b'\beta} \Phi^{bb'}_{\alpha\beta}\left(\mathbf{R}_l, \mathbf{R}_{l'}\right) \mathbf{u}^{b'}_\beta\left(\mathbf{R}_{l'}\right). \tag{2.30}$$

Applying an antisymmetric, infinitesimal rotation, S^R such that $S^R_{\beta\gamma} = -S^R_{\gamma\beta}$ is equivalent to a perturbation of the form

$$\begin{aligned}
\mathbf{u}^{b'}_\beta\left(\mathbf{R}_{l'}\right) &= \sum_\gamma S^R_{\beta\gamma} \cdot \left[\left(\mathbf{R}_{l'} + \boldsymbol{\tau}_{b'}\right) - \left(\mathbf{R}_l + \boldsymbol{\tau}_b\right)\right]_\gamma && (2.31)\\
&= \sum_\gamma S^R_{\beta\gamma} \Delta r^{bb'}_\gamma\left(\mathbf{R}_l, \mathbf{R}_{l'}\right) && (2.32)\\
&= -\sum_\gamma S^R_{\beta\gamma} \Delta r^{bb'}_\gamma\left(\mathbf{R}_{l'}, \mathbf{R}_l\right). && (2.33)
\end{aligned}$$

For convenience, we define the difference between two sites as $\Delta r^{bb'}_\gamma = \left(\mathbf{R}_{l'} + \boldsymbol{\tau}_{b'}\right) - \left(\mathbf{R}_l + \boldsymbol{\tau}_b\right)$. Substituting this expression for the perturbation into Equation 2.30, we obtain

$$\frac{\partial \Phi}{\partial \mathbf{u}^b_\alpha\left(\mathbf{R}_l\right)} = \Phi^b_\alpha\left(\mathbf{R}_l\right) - \sum_{l'b'\gamma} \Phi^{bb'}_{\alpha\beta}\left(\mathbf{R}_l, \mathbf{R}_{l'}\right) S^R_{\beta\gamma} \Delta r^{bb'}_\gamma\left(\mathbf{R}_{l'}, \mathbf{R}_l\right). \tag{2.34}$$

Applying a rigid rotation means the derivative of the potential behaves as

$$\begin{aligned}
\frac{\partial \Phi}{\partial \mathbf{u}^b_\alpha\left(\mathbf{R}_l\right)} &= \sum_\beta \left(\delta_{\alpha\beta} + S^R_{\alpha\beta}\right) \Phi^b_\beta\left(\mathbf{R}_l\right) && (2.35)\\
&= \Phi^b_\alpha\left(\mathbf{R}_l\right) + \sum_\beta S^R_{\alpha\beta} \Phi^b_\beta\left(\mathbf{R}_l\right), && (2.36)
\end{aligned}$$

where $\delta_{\alpha\beta}$ is the Kronecker delta function. Equating Equations 2.34 and 2.36 results in

$$\sum_{\beta} S^R_{\alpha\beta}\Phi^b_{\beta}\left(\mathbf{R}_l\right) = -\sum_{l'b'\gamma} \Phi^{bb'}_{\alpha\beta}\left(\mathbf{R}_l, \mathbf{R}_{l'}\right) S^R_{\beta\gamma}\Delta r^{bb'}_{\gamma}\left(\mathbf{R}_{l'}, \mathbf{R}_l\right). \tag{2.37}$$

Recalling that the rotational matrix S^R is antisymmetric ($S^R_{\beta\gamma} = -S^R_{\gamma\beta}$), this expression can be further simplified as

$$\delta_{\alpha\beta}\Phi^b_{\gamma}\left(\mathbf{R}_l\right) - \delta_{\alpha\gamma}\Phi^b_{\beta}\left(\mathbf{R}_l\right) = -\sum_{l'b'} \left[\Phi^{bb'}_{\alpha\beta}\left(\mathbf{R}_l, \mathbf{R}_{l'}\right)\Delta r^{bb'}_{\gamma}\left(\mathbf{R}_{l'}, \mathbf{R}_l\right) - \Phi^{bb'}_{\alpha\gamma}\left(\mathbf{R}_l, \mathbf{R}_{l'}\right)\Delta r^{bb'}_{\beta}\left(\mathbf{R}_{l'}, \mathbf{R}_l\right)\right]. \tag{2.38}$$

As we mentioned at the beginning, at equilibrium, $\Phi^b_{\alpha}\left(\mathbf{R}_l\right)$ is zero due to the absence of forces. This results in the final expression for the rotational invariance condition [17, 27]

$$\sum_{l'b'} \left[\Phi^{bb'}_{\alpha\beta}\left(\mathbf{R}_l, \mathbf{R}_{l'}\right)\Delta r^{bb'}_{\gamma}\left(\mathbf{R}_{l'}, \mathbf{R}_l\right) - \Phi^{bb'}_{\alpha\gamma}\left(\mathbf{R}_l, \mathbf{R}_{l'}\right)\Delta r^{bb'}_{\beta}\left(\mathbf{R}_{l'}, \mathbf{R}_l\right)\right] = 0. \tag{2.39}$$

These force constants rules and constraints can be applied during the fitting of the force constants via a constrained least squares method, the mathematics of which are detailed in Appendix A.3.

2.1.3 Non-Analytic Born Effective Charge Correction

Electrostatic interactions arising from atomic displacements are largely screened in metals, but in insulating, ionic materials, the electrostatic effects do not decay as rapidly, and thus cannot be ignored [13, 28]. Phonon modes approaching the center of the Brillouin zone Γ have wavelengths approaching infinity. Acoustic modes within this limit result in atoms in a unit cell moving in-phase with each other, corresponding to a rigid translation of the crystal. Optical modes at Γ correspond to atoms moving out-of-phase from each other. In ionic materials, as oppositely charged ions vibrate in opposite directions in the manner of optical modes, dynamic dipoles arise and interact with each other Coulombically and induce macrosocpic electric fields. This effect results in the splitting of longitudinal optical and transverse optical (LO-TO) frequencies around the Brillouin zone center such that the longitudinal frequency is higher than the transverse frequency [17]. An expression for the ratio of the longitudinal and transverse frequencies known as the Lyddane-Sachs-Teller relation [29] was further extended for more general crystal symmetries by Cochran and Cowley [30].

A non-analytical correction to the analytical expression of the dynamical matrix that

reflects this behavior is needed and takes the form of

$$D^{bb'}_{\alpha\beta}\left(\mathbf{k};\mathrm{na}\right) = \frac{1}{\sqrt{M_b M_{b'}}}\frac{4\pi e^2}{V}\frac{\left(\sum_\gamma Z^b_{\alpha\gamma}\mathbf{k}_\gamma\right)\left(\sum_{\gamma'} Z^{b'}_{\beta\gamma'}\mathbf{k}_{\gamma'}\right)}{\mathbf{k}\cdot\varepsilon^{(\infty)}\cdot\mathbf{k}} f\left(\mathbf{k}\right), \tag{2.40}$$

where different expressions of $f(\mathbf{k})$ have been proposed. The terms Z^b and $Z^{b'}$ are the Born effective charge tensors, a 3×3 matrix proportionality constant between the dipole moment and the atomic displacement causing this polarization. Specifically, each $Z^b_{\beta\alpha}$ refers to the polarization along direction β as a result of a displacement in the α direction of basis atom b [31]. $\epsilon^{(\infty)}$ is the macroscopic dielectric tensor.

One approach to account for this LO-TO splitting was formulated by Parlinski *et al.* [32], where a Gaussian smearing is applied to the non-analytical correction to ensure its decay before reaching a k-point commensurate with the supercell:

$$f\left(\mathbf{k}\right) = \exp\left(2\pi i\mathbf{k}^2/\rho^2\right) \tag{2.41}$$

Here, commensurate k-points are defined as points in reciprocal space obtained by a perfect tiling of the supercell's reciprocal lattice within the unit cell's reciprocal lattice, except for the Γ point [33]. The damping factor ρ can be calculated based on the particular unit cell's k-points and the supercell geometry. It should be chosen such that the non-analytic contribution to the dynamical matrix dies off before reaching the nearest commensurate k-point.

Another more recent approach formulated by Wang *et al.* [33] takes the form of

$$f\left(\mathbf{k}\right) = \frac{1}{N}\sum_l \exp\left(i\mathbf{k}\cdot\left[\mathbf{R}_l - \mathbf{R}_0\right]\right) \tag{2.42}$$

where N is the number of unit cells, indexed by l, in the larger supercell from which the force constants were calculated. The quantity $\mathbf{R}_l - \mathbf{R}_0$ is the distance of each unit cell l relative to the first unit cell. This correction similarly approaches zero at commensurate k-points. Both forms of $f\left(\mathbf{k}\right)$ also fulfill the requirement of Cochran and Cowley [30] as $\mathbf{k}$ approaches the Γ point. They are also non-zero at k-points that are not commensurate with the supercell, which is necessary as the effect of these electrostatic effects persist at these points.

2.1.4 Statistical Mechanics and Thermodynamics

Solutions to the Schrödinger equation using the fully diagonalized Hamiltonian in Equation 2.15 describing independent harmonic oscillators provide the energy of a particular mi-

crostate of the system. Thermodynamic quantities can be calculated by averaging over these microstates, which can be defined as a collection of quantum numbers $\vec{n} = \{n_{k0}, n_{k1}, \ldots, n_{k3N}\}$. This is the set of integers that define the energy occupancy level for each harmonic oscillator. The energy of a microstate is then a sum of the energies of all the harmonic oscillators in the system

$$E_{\vec{n}} = \sum_k \hbar\omega_k \left(n_k + \frac{1}{2}\right). \tag{2.43}$$

It follows that the partition function of the entire system is then

$$Z = \sum_{\vec{n}} \exp\left(-\beta E_{\vec{n}}\right), \tag{2.44}$$

where we sum over all possible microstates of the system and $\beta = k_B T$ has been introduced for simplicity. This can be further written as

$$Z = \sum_{n_{k0}} \sum_{n_{k1}} \cdots \sum_{n_{k3N}} \prod_k \exp\left[-\beta\hbar\omega_k \left(n_k + \frac{1}{2}\right)\right], \tag{2.45}$$

since the sum within an exponent is equivalent to a product of exponents. We can then rearrange exponent terms as each exponent term is dependent only on one of the sums

$$Z = \sum_{n_{k0}} \exp\left[-\beta\hbar\omega_k \left(n_{k0} + \frac{1}{2}\right)\right] \sum_{n_{k1}} \exp\left[-\beta\hbar\omega_k \left(n_{k1} + \frac{1}{2}\right)\right] \cdots \sum_{n_{k3N}} \exp\left[-\beta\hbar\omega_k \left(n_{k3N} + \frac{1}{2}\right)\right], \tag{2.46}$$

This expression can be written more compactly as

$$Z = \prod_k^{3N} \sum_{n_k} \exp\left[-\beta\hbar\omega_k \left(n_k + \frac{1}{2}\right)\right], \tag{2.47}$$

where the sum over all possible energy levels $\{n_k = 0, 1, \dots\}$ is the partition function of a single harmonic oscillator Z_k, which can be further simplified using a geometric series

$$Z_k = \sum_{n_k} \exp\left[-\beta\hbar\omega_k\left(n_k + \frac{1}{2}\right)\right] \tag{2.48}$$

$$= \exp\left(-\frac{1}{2}\beta\hbar\omega_k\right)\sum_{n_k}\exp\left[-\beta\hbar\omega_k n_k\right] \tag{2.49}$$

$$= \frac{\exp\left(-\frac{1}{2}\beta\hbar\omega_k\right)}{1-\exp\left(-\beta\hbar\omega_k\right)}. \tag{2.50}$$

To obtain the total vibrational free energy, the partition function in Equation 2.47 is substituted into $F = -(1/\beta)\ln Z$

$$F = -\frac{1}{\beta}\ln\prod_k^{3N}\frac{\exp\left(-\frac{1}{2}\beta\hbar\omega_i\right)}{1-\exp\left(-\beta\hbar\omega_i\right)} \tag{2.51}$$

$$= -\frac{1}{\beta}\sum_k^{3N}\ln\left(\frac{\exp\left(-\frac{1}{2}\beta\hbar\omega_k\right)}{1-\exp\left(-\beta\hbar\omega_k\right)}\right) \tag{2.52}$$

$$= \frac{1}{\beta}\sum_k^{3N}\frac{1}{2}\beta\hbar\omega_k + \ln\left[1-\exp\left(-\beta\hbar\omega_k\right)\right]. \tag{2.53}$$

Here, we introduce the density of states $g(\omega_k)$, an integration over all the frequencies in the Brillouin zone

$$\int_0^\infty g(\omega_k)d\omega_k = 3N. \tag{2.54}$$

The vibrational free energy can be ultimately be expressed as

$$F = \frac{1}{2}\int_0^\infty \hbar\omega_k g(\omega_k)d\omega_k + \frac{1}{\beta}\int_0^\infty \ln\left[1-\exp\left(-\beta\hbar\omega_k\right)\right]g(\omega_k)d\omega_k \tag{2.55}$$

where

$$E_{\text{zp}} = \frac{1}{2}\int_0^\infty g(\omega_k)\hbar\omega_k d\omega_k \tag{2.56}$$

is the zero-point energy corresponding to the vibrational groundstate and resulting from the fact that the lowest $n = 0$ level of the quantized energies of a harmonic oscillator is finite. Differentiating the free energy with respect to temperature results in vibrational entropy,

defined as

$$S = -k_B \int_0^\infty g(\omega_k) \cdot \ln\left[1 - \exp\left(-\hbar\omega_k/kT\right)\right] d\omega_k - \frac{1}{T}\int_0^\infty g(\omega_k) \frac{\hbar\omega_k}{\exp\left(\hbar\omega_k/kT\right) - 1} d\omega_k. \tag{2.57}$$

An intuitive understanding of how phonon frequencies may contribute to vibrational entropy can be derived from considering a 1-D lattice. The frequency of an individual harmonic oscillator in this simplified model is proportionally related to its force constant

$$\omega_k = \sqrt{\frac{\Phi_k}{m}}, \tag{2.58}$$

so a lower frequency tends to correspond to a softer spring. The separation of discretized energy levels E_k, determined by $\hbar\omega_k$ in Equation 2.24, is smaller for a softer spring. In calculating the partition function and ultimately the vibrational entropy, this translates into the sampling of more states, leading to an overal increase in entropy. Conversely, higher frequencies correspond to stiffer spring constants and energy levels that are separated further apart, thus contributing less to entropy.

2.1.5 Quasi-Harmonic Approximation

The beauty and simplicity of the harmonic approximation works well for materials where the assumption that atoms are heavy and their movements only oscillate within the vicinity of their equilibrium positions is valid. At low temperatures, this model can also be valid to an extent as lower temperatures will induce less thermal excitations. At high temperatures, however, this model is no longer accurate as volumetric changes due to thermal expansion have to be accounted for. The quasi-harmonic approximation is an attempt to correct for these thermal expansion effects.

By obtaining Helmholtz free energies at volumes both larger and smaller than the equilibrium volume, we can build a free energy that is dependent not only on temperature, but also on volume

$$F(T, V) = E_0(V) + F^H(T, V), \tag{2.59}$$

where as usual, $E_0(V)$ is the energy of our static crystal at a specific volume V, and our harmonic free energies at each volume is denoted as $F^H(T, V)$. Differentiating the free energy

with respect to volume gives negative pressure

$$\left(\frac{\partial F}{\partial V}\right)\Big|_T = -P. \tag{2.60}$$

Minimizing $F(T, V)$ with respect to volume at each temperature, we obtain an equilibrium volume $V^*(T)$ at zero pressure. The free energies evaluated at these equilibrium volumes $F(T, V^*(T))$ gives a Gibbs free energy at zero pressure.

In the following chapters, we will use the quasi-harmonic approximation to obtain free energies to explore vibrational stabilization of various materials. A simple case exploring the stabilization of a metastable Cu_2Sb relative to Cu and Sb through phonons can be found in Appendix B.

2.1.6 Forces from First-Principles Calculations

There are two main approaches to calculating the force constants described in Section 2.1.1 needed to construct the dynamical matrix in Equation 2.13. The first is the direct approach or supercell method, in which Hellmann-Feynman forces resulting from perturbations of atoms within a supercell from equilibrium positions are used to calculate the force constants necessary for the dynamical matrix [18, 19, 28, 34]. A number of atomic displacements are imposed on atoms within a supercell, typically ranging anywhere from 30 - 100 atoms, along high symmetry directions. An optimal supercell size can be determined by the means of convergence tests of force constants [18] or free energies, depending on the ultimate aim and computational limitations. The symmetry of the supercell can be used to minimize the number of perturbation directions necessary for a complete description of force constants [19]. The forces resulting from the perturbations are used in a least squares fit of a system of linear equations to calculate the force constants between pairs of atoms.

The second approach to obtaining force constants is based on linear-response theory [35, 36]. In this approach, the dynamical matrix can be evaluated at specific k-points. Typically, the Hessian of the Born Oppenheimer energy surface is calculated by differentiating the Hellmann-Feynman forces with respect to atomic positions [36]. Practically, this is accomplished by calculating the response of a ground-state electron charge density to perturbations of atoms within an equilibrium supercell structure. The Hessian matrix obtained is essentially a collection of 3×3 matrices, each of which is an inter-atomic force constant between two atoms in the supercell. As this method is not used in this work, we will not go into details of the method and its formulations.

2.2 First-Principles Calculations

To obtain forces needed to fit the interatomic force constants previously defined in Equation 2.3, first-principles calculations are employed. Conceptually, the foundation of the technique is in solving the many body Schrödinger equation

$$H\psi = E\psi, \tag{2.61}$$

which relates the Hamiltonian H to the energy of the system E through a many-body wave function ψ [37]. An exact solution can in theory provide the allowed eigenstates and corresponding energies, but obtaining a precise solution to this equation for realistic material systems is not feasible, even with current computational capabilities. A simplification in the form of an approximate Hamiltonian is introduced

$$H = T\left(\mathbf{r}_i\right) + V\left(\mathbf{r}_i, \mathbf{r}_j\right) + V\left(\mathbf{r}_i, \mathbf{R}_j\right) + V\left(\mathbf{R}_i, \mathbf{R}_j\right). \tag{2.62}$$

The first term is the kinetic energy operator of electrons

$$T = -\frac{\hbar^2}{2m}\sum_i \nabla_i^2. \tag{2.63}$$

The second term describes the Coulombic interaction between electrons

$$V\left(\mathbf{r}_i, \mathbf{r}_j\right) = \sum_i \sum_{j<i} \frac{1}{|\mathbf{r}_j - \mathbf{r}_i|}, \tag{2.64}$$

while the third term is the Coulombic interaction between electrons and nuclei

$$V\left(\mathbf{r}_i, \mathbf{R}_j\right) = -\sum_i \sum_j \frac{Z_j}{|\mathbf{R}_j - \mathbf{r}_i|}. \tag{2.65}$$

Finally, the last term expresses the ion-ion Coulomb potential

$$V\left(\mathbf{R}_i, \mathbf{R}_j\right) = \sum_i \sum_{j<i} \frac{Z_i Z_j}{|\mathbf{R}_j - \mathbf{R}_i|}. \tag{2.66}$$

In these expressions, m is the electron mass, $\mathbf{r}_i$ is the position of electron i, $\mathbf{R}_i$ is the position of a nucleus i, and Z_i is the nucleus charge of atom i. What is notably missing from the Hamiltonian is the contribution of the kinetic energy of the nuclei. The description above is based on the Born-Oppenheimer approximation. Under this assumption, the nuclei are

considered to be at fixed positions given the ease at which electrons respond to changes in their environment. Another simplification of the approximate Hamiltonian is that the nuclei are treated classically, while the electrons are treated quantum mechanically.

An initial approach to solving this many-body problem was the Hartree method [37]. In this model, the eigenfunctions of Equation 2.61 are approximated as a product of individual, orthonormal single-electron wave functions

$$\psi\left(\mathbf{r}_1, \mathbf{r}_2, \ldots, \mathbf{r}_N\right) = \psi\left(\mathbf{r}_1\right)\psi\left(\mathbf{r}_2\right)\cdots\psi\left(\mathbf{r}_N\right). \tag{2.67}$$

The electrons in this Hartree product are assumed to be non-interacting. This assumption is precisely one of the failings of the model because in a real system, electrons do not behave independently, and thus there are non-negligible correlation effects between electrons. Another oversimplification is that the wave functions do not obey exchange symmetry, where when two electrons swap places, the wave function needs to change signs. An improvement was introduced via the Hartree-Fock approach [37], where a Slater determinant composed of one electron wave functions obeying exchange symmetry is used as a more accurate approximation of the wave function. Despite this modification, the model still does not account for electron correlations.

2.2.1 Density Functional Theory

A slightly less computationally intensive method to solving the many-body Schrödinger equation in which electron interactions are approximated is density functional theory (DFT). Rather than solving a problem with $3n$ degrees of freedom, one for each of the 3 spatial coordinates of n electrons, Hohenberg and Kohn [38] introduced the concept that the ground state energy is a unique functional of the electron density, $E\left[n\left(\mathbf{r}\right)\right]$. Instead of solving for $3n$ variables of the wave function, the problem is reduced down to the three spatial variables of the electron density.

Another important result by Hohenberg and Kohn is that the electron density resulting from minimizing the energy functional is the electron density mapping directly onto the solution of the Schrödinger equation. This is known as the variational principle. The combination of the two concepts indicate that by minimizing the density functional, both the ground state energy and corresponding electron density can be obtained. The energy functional for an electron density takes on the form of [39]

$$E\left[\rho\right] = T_{\mathrm{S}}\left[\rho\right] + \int V_{\mathrm{ext}}\left(\mathbf{r}\right)\rho\left(\mathbf{r}\right)d\mathbf{r} + E_H\left[\rho\right] + E_{\mathrm{XC}}\left[\rho\right], \tag{2.68}$$

where $T_{\mathrm{S}}[\rho]$ is the kinetic energy of independent electrons. The second term $\int V_{\mathrm{ext}}(\mathbf{r})\,\rho(\mathbf{r})\,d\mathbf{r}$ is the interaction energy between the electron density and an external potential field arising from Coulombic interactions between the electrons and ions. The term $E_H[\rho]$ is the Hartree term resulting from classical Coulombic interactions between electrons. The last term, $E_{\mathrm{XC}}[\rho]$, is the exchange-correlation energy. In a realistic system, electron interactions are correlated, and thus an attempt to correct for the treatment of electrons as classical ions in the Hartree term is included in this last exchange-correlation term. In addition, kinetic energy differences between a system with independent electrons and interacting electrons are also built in. This last term is the most difficult to capture, as it is meant to account for corrections to the other three terms in an attempt to describe a realistic, physical system.

There are different implementations of $E_{\mathrm{XC}}[\rho]$. Two of the most popular are the local density approximation (LDA) [40], and the generalized gradient approximation (GGA) [41]. The exchange correlation term in LDA is dependent on the exchange-correlation energy of a homogeneous electron gas. While this works for localized systems such as layered materials, it tends to under-predict lattice parameters relative to experimental values. GGA, on the other hand, is also dependent on the gradient of the local electron density. Despite this correction, GGA tends to over-predict lattice parameters.

Even within these approximations, there are different parameterizations. Initially, GGA as parameterized by Perdew and Wang, often referred to as PW-91 [42], was used. An improvement was introduced by Perdew, Burke, and Ernzerhof (PBE) [43]. In more recent years, a pseudopotential method designed specifically for solids, PBE-sol, [44] has been resulted in better agreement with experimental lattice parameters.

2.2.2 Pseudopotential Method

Kohn and Sham introduced a method in which the problem of solving for the electron density can be simplified to solving a collection of equations each corresponding to an independent electron. Each of these Kohn-Sham equations takes the form

$$\left[-\frac{\hbar^2}{2m}\nabla^2 + V(\mathbf{r}) + V_H(\mathbf{r}) + V_{XC}(\mathbf{r})\right]\psi_i(\mathbf{r}) = \epsilon_i\psi_i(\mathbf{r}), \tag{2.69}$$

where each single-electron wave function $\psi_i(\mathbf{r})$ depends solely on the three spatial variables. The terms in the brackets on the left hand side of the equation resemble the form of the approximate Hamiltonian expressed in Equation 2.62. Of the three potential terms, the first, $V(\mathbf{r})$, represents the interaction between the single electron i and the collection of atomic nuclei. The second potential term $V_H(\mathbf{r})$ is the Hartree potential, which physically describes a Coulombic repulsion between electron i and the total electron density. This

Hartree potential includes a nonphysical self-interaction term between electron i with itself. A correction for this interaction is built into the exchange-correlation potential, $V_{XC}(\mathbf{r})$, which is a derivative of the exchange-correlation energy (first encountered in 2.68)

$$V_{XC}(\mathbf{r}) = \frac{\delta E_{XC}(\mathbf{r})}{\delta n(\mathbf{r})}. \tag{2.70}$$

As both the Hartree potential and the exchange-correlation potential both depend also on the entire electron density rather than only an independent electron, the seemingly independent single-electron wave functions are still inter-dependent. As a result, a self-consistent method to solving the Kohn-Sham equations is required to obtain the ground state energy and corresponding electron density.

There are two primary numerical approaches to solving the Kohn-Sham equations, the Linear Augmented Plane Wave (LAPW) method and the pseudopotential method [45, 46]. While the LAPW method is considered more accurate, the pseudopotential method is more computationally efficient. In the pseudopotential method, the core electrons are assumed to be frozen and to have no effect on the bonding. The core electrons are replaced by an effective potential. This pseudopotential approach therefore reduces the number of Kohn-Sham equations to be solved due to a reduction in the number of participating electrons. A popular generalization of the LAPW and pseudopotential method is the Projector-Augmented Wave (PAW) method [47,48]. The implementation of these methods by the Vienna Ab Initio Simulation Package (VASP) [49] was used to perform the calculations in this dissertation.

2.2.3 Cluster Expansion

The cluster expansion method has been well-studied and implemented in many systems to predict macroscopic physical properties of a crystal system that depend on configurational degrees of freedom [2–4]. In a system where there are N possible Li-vacancy sites, there are 2^N possible ways to distribute Li-ions and vacancies over those sites. Each arrangement or configuration can be represented uniquely by assigning each site in the crystal a site variable σ_i. In a spin basis, if a site i is occupied by a Li-ion, then $\sigma_i = 1$; conversely, if a site j is occupied by a vacancy, then $\sigma_j = -1$. A particular configuration can be expressed in terms of a vector of these site variables, $\vec{\sigma} = \{\sigma_1, \ldots, \sigma_i, \ldots, \sigma_N\}$. Site basis functions are used to describe all possible states that a particular site can have. Interactions between sites in the crystal can be broken down into pair, triplet, or even quadruplet interactions, where each collection of sites is referred to as a cluster. Within this framework, to describe an entire crystal, cluster basis functions, ϕ_α, are constructed by taking tensor products of site basis

functions. For a given cluster α, the cluster basis function is represented as

$$\phi_\alpha(\vec{\sigma}) = \prod_{i \in \alpha} \sigma_i. \tag{2.71}$$

The cluster basis functions form a complete and orthonormal basis in configurational space, and properties of the system with configurational dependence can therefore be expressed as linear combinations of these functions [2].

Within this cluster expansion description, the energy of a static crystal, which is dependent on configurational degrees of freedom, $\vec{\sigma}$, can be represented by an expansion of these basis functions and expressed as

$$E(\vec{\sigma}) = V_0 + \sum_\alpha V_\alpha \phi_\alpha(\vec{\sigma}). \tag{2.72}$$

The coefficients V_0 and V_α are known as the effective cluster interactions (ECIs). The summation is over clusters of different sizes, which can be more explicitly expressed as

$$E(\vec{\sigma}) = V_0 + \sum_i V_i \sigma_i + \sum_{ij} V_{ij} \sigma_i \sigma_j + \sum_{ijk} V_{ijk} \sigma_i \sigma_j \sigma_k + \cdots. \tag{2.73}$$

The individual summations are over single, pair, and triplet clusters as denoted by the site indexing i, j, and k. As in Equation 2.72, the V's are expansion coefficients. Although the cluster expansion is theoretically over all possible cluster sizes (number of sites in the cluster) and lengths (distance between sites), in practice a truncation is typically applied to both as the strongest and most important interactions often occur between smaller clusters and within a radius where the cluster expansion has converged. To obtain the ECIs that accurately describe the system of interest, first-principle calculations of different configurations are performed and their corresponding energies are collected. A least squares fit between the occupation variables σ and the formation energies is used to determine the ECIs.

The convergence and quality of a cluster expansion are quantified by the cross validation (CV) score and the root mean square (RMS) error. The CV score is a measure of the ability of the model to accurately predict configurational energies [50]. Specifically, the leave-one-out CV score was utilized, and is calculated as

$$\mathrm{CV}^2 = \frac{1}{N} \sum_{i=1}^{N} \left(E(\vec{\sigma}_i) - E'(\vec{\sigma}_i)^2 \right).$$

For each of the N calculated configurations, the first principles energy $E(\vec{\sigma}_i)$ is compared

to the predicted energy $E'(\vec{\sigma}_i)$, where the predicted energy is calculated by first performing a least-squares fit to the other $N-1$ configurations and subsequently evaluating the cluster expanded energy of the excluded configuration $\vec{\sigma}_i$. The RMS error provides a measure of the ability of the cluster expansion model to predict formation energies of calculated configurations. Typically, lower CV and rms scores are correlated with cluster expansions that correctly predict stable ground states. The Cluster Assisted Statistical Mechanics [51, 52] implementation of the cluster expansion was used in Chapter VI to cluster expand over Li-Va sites in trirutile $Li_{3x}Fe_2F_6$.

2.2.4 Monte Carlo

Monte Carlo simulations are used to calculate thermodynamic averages in statistical mechanics. In this method, different microstates resulting from a Markov chain of configurational evolution are sampled [53]. The Metropolis algorithm was used, where the successful transition from configuration A to B each with grand canonical energies Ω_A and Ω_B is determined by a transition probability calculated as

$$P(A \to B) \begin{cases} 1 & \text{if } \Omega_B < \Omega_A \\ e^{-\Delta\Omega/k_B T} & \text{if } \Omega_B \geq \Omega_A \end{cases}. \tag{2.74}$$

The energy difference between the two states is given as $\Delta\Omega = \Omega_B - \Omega_A$. The grand canonical energy Ω is

$$\Omega = E(\vec{\sigma}) - \mu N, \tag{2.75}$$

where $E(\vec{\sigma})$ is the average energy of a configuration defined by occupation variables $\vec{\sigma}$, μ is the chemical potential, and N is the number of sites. Following the rule given in Equation 2.74, if the energy of the new configuration Ω_B is lower than the current state Ω_A, then naturally the transition occurs. If Ω_B is higher, however, the probability $P(A \to B)$ is compared to a randomly generated number. If the probability is larger than this random number, then the new configuration is accepted. If the probability is smaller, however, the current configuration is kept.

The effective Hamiltonian resulting from a cluster expansion is used to estimate the formation energy of each new configuration in the Monte Carlo simulation and to facilitate sampling a large enough number of microstates to calculate thermodynamic averages. Monte Carlo simulations can either be performed at constant chemical potential to obtain heating and cooling runs or at constant temperature for chemical potential runs. The latter was

used to calculate a voltage curve for lithium insertion into $Li_{3x}Fe_2F_6$ in Chapter VI. For a given temperature, this voltage is

$$V\left(x_{\mathrm{Li}}\right) = -\frac{\mu_{\mathrm{Li}} - \mu_{\mathrm{Li}}^{\mathrm{reference}}}{Fz}, \tag{2.76}$$

where μ_{Li} is the chemical potential of Li in the intercalation material, $\mu_{\mathrm{Li}}^{\mathrm{reference}}$ is the chemical potential of a pure Li reference, F is Faraday's constant, and z is the electron charge of a Li ion.

CHAPTER III

Anharmonicity and Phase Stability of Antiperovskite Cubic Li_3OCl

3.1 Introduction

The recently discovered antiperovskite Li_3OCl compound is a promising solid electrolyte for Li-ion batteries, with ionic conductivities reported [6] to be almost as high as 2 mS cm^{-1}. Li_3OCl has a perovskite crystal structure, but with the role of anions and cations reversed (Figure 3.1a): The positively charged Li ions form the corner sharing octahedra while the negatively charged O ions occupy the center of the Li-octahedra; the negatively charged Cl occupy the large cages at the center of the unit cell coordinated by 12 Li ions. Several first-principles studies of Li transport in the antiperovskite crystal structure have predicted low migration barriers for Li-vacancy exchanges, with values on the order of 350 meV [7,54]. An even lower migration barrier of approximately 160 meV was predicted for an interstitial dumbbell mechanism [7]. The effect of alloying in $Li_3OCl_{1-x}Br_x$ on the migration barriers of vacancy mediated Li diffusion was also recently investigated from first-principles [55]. While Li vacancies and Li interstitials can appear at stoichiometric compositions through the creation of Frenkel defect pairs, the formation energy of such pairs is predicted to be too large [7] to achieve an appreciable concentration of diffusion mediating defects at room temperature. Off-stoichiometric compositions that are Li rich are likely more desirable to ensure an excess of Li ions that can migrate by means of the interstitial dumbbell mechanism.

Devising strategies to synthesize off-stoichiometric compositions of Li_3OCl by doping or alloying requires an understanding of the factors stabilizing Li_3OCl. First-principles studies predict that Li_3OCl is metastable at zero Kelvin relative to decomposition into LiCl and Li_2O [7,54] (Figures 3.1b and 3.1c). The ability to synthesize Li_3OCl experimentally [6], however, suggests that this compound is likely entropically stabilized at elevated temperatures, if not at room temperature, then at least at the higher synthesis temperatures of approximately

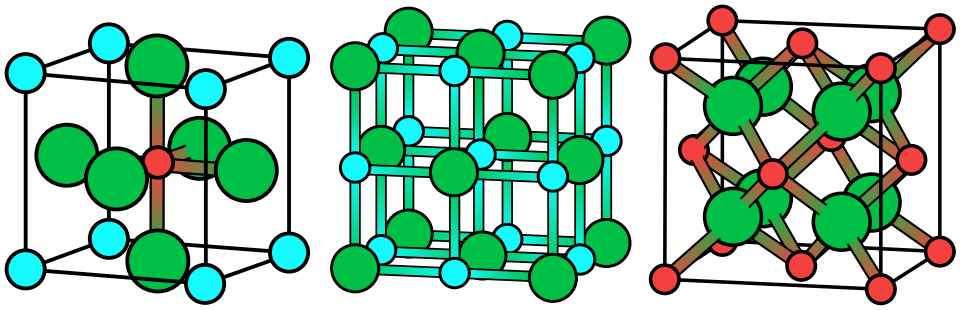

Figure 3.1. Crystal structures of (a) Li_3OCl, (b) LiCl, and (c) Li_2O. Lithium, oxygen, and chlorine atoms are represented by green, red, and blue circles, respectively.

$330 - 360°C$ [6]. As Li_3OCl does not exhibit significant configurational disorder and is an insulator, the most important degrees of freedom are vibrational excitations.

Perovskite structures have been widely studied. A perfectly cubic perovskite is rarely observed and most perovskites that exhibit cubic symmetry at high temperature undergo symmetry breaking transitions at low temperature. Symmetry breaking distortions can arise either as a result of distortions of the octahedra, or due to rotations of the octahedra [56]. The Glazer notation has been established to classify structures that can be derived from cubic perovskite through octahedral rotations [57]. Octahedral rotations around the three cubic axes are denoted with the notation $a^*b^*c^*$ where the letters a, b and c represent relative tilt angles around the cubic axes of the octahedra, and the $*$ can be $+$, $-$, or 0, depending on whether an in-phase, out-of-phase, or no tilt of neighboring octahedra has occurred [57]. In the case of the cubic $Pm\bar{3}m$ Li_3OCl structure, which has no tilts, the tilt system is represented as $a^0a^0a^0$. Howard and Stokes have taken the 23 tilt systems proposed by Glazer [57] and using group-theory, simplified the list to 15 distinct tilt systems [58]. These group theoretic tools have proven invaluable in analyzing rotational instabilities in a wide range of perovskites [59–62].

In this work, we investigate the stability of Li_3OCl using lattice dynamics. We find that Li_3OCl is mechanically unstable with respect to octahedral rotations. We map out the energy landscape as a function of unstable modes and find that the minima correspond to several of the 14 rotational tilt systems [58]. The energy gained by octahedral rotations relative to the cubic crystal, however, is predicted to be very small, suggesting that the high-symmetry cubic form of Li_3OCl should emerge even at low temperatures due to anharmonic vibrational excitations. Additionally, we find that vibrational entropy will likely stabilize the cubic $Pm\bar{3}m$ form of Li_3OCl relative to decomposition into LiCl and Li_2O above room temperature.

3.2 Methodology

First-principles density functional calculations were performed using the Vienna Ab Initio Simulation Package (VASP) [48, 49] within the generalized gradient approximation (GGA) as implemented by Perdew, Burke, and Ernzerhof [43]. Projector augmented wave [47, 49] pseudopotentials with valence-electron configurations of $1s^1 2s^1 2p^1$ for Li, $2s^2 2p^4$ for O, and $3s^2 3p^5$ for Cl and an energy cutoff of 600 eV were used.

Force constants for Li_3OCl were calculated using the frozen phonon approach. Isolated atomic displacements relative to their high symmetry positions in cubic antiperovskite were sampled in large supercells. The resulting forces on all the atoms in the supercell were then calculated with VASP. Force constants were determined using a least-squares fit between atomic perturbations and the calculated forces. The force constants were then used to construct the dynamical matrix [5, 12, 17, 18, 31]. Since Li_3OCl is an ionic crystal, the effect of dipole-dipole interactions must also be accounted for in the dynamical matrix [29, 30, 36]. Born effective charges and dielectric tensors were calculated with density functional perturbation theory as implemented in VASP [35, 63]. These were then used to calculate the non-analytic contribution to the dynamical matrix, which was evaluated within the same supercell as that for the atomic perturbations using the envelope function introduced by Wang et al [33]. A $6 \times 6 \times 6$ (1080 atoms) cubic supercell of the primitive cubic structures ($a = 3.907\mathring{A}$) was fully relaxed before applying various displacements of length $0.015\mathring{A}$ to each of the three asymmetric unit cell sites in the Li_3OCl structure. A $3 \times 3 \times 3$ Gamma-centered k-point mesh was used in the VASP calculations performed on these supercells.

We also calculated vibrational free energies within the quasi-harmonic approximation for Li_3OCl, LiCl and Li_2O. Phonon dispersion curves and their corresponding densities of states were calculated as described above for a range of volumes. Smaller supercells were used for the quasi-harmonic calculations. For Li_3OCl, a $3 \times 3 \times 3$ supercell of the primitive cubic unit cell was used (containing 27 primitive cells and 135 atoms). For LiCl and Li_2O, supercells containing 32 unit cells (64 atoms) and 27 unit cells (81 atoms) were used. Atomic perturbations having lengths of 0.015, 0.15, and 0.03 $\mathring{A}$ for Li_3OCl, LiCl, and Li_2O, respectively were sampled to extract force constants. A second order polynomial fit of the free energy dependence on volume was used to obtain the Gibbs free energy as a function of temperature.

Irreducible representations of the $Pm\bar{3}m$ phase were obtained via the SMODES module of ISOTROPY (ISOTROPY Software Suite, iso.byu.edu). Accompanying each irreducible representation is one or more symmetrized collective displacement mode, each of which transforms the dynamical matrix into block diagonal form. The energy of the crystal was then calculated with VASP as a function of the amplitudes of the displacement modes. Energy

calculations of collective displacements having M_3^+ and R_4^+ symmetries were performed in a supercell containing two primitive unit cells of Li_3OCl.

The FINDSYM module [64] of ISOTROPY was used to verify the space groups of the 15 structures resulting from octahedral tilts of the $Pm\bar{3}m$ structure. Structures were calculated using the same $2 \times 2 \times 2$ supercell of the 5 atom cubic primitive with a $9 \times 9 \times 9$ Γ-centered k-point mesh, thus ensuring that an identical k-point mesh was used for each structure. After a full relaxation of each structure, final energies were calculated using the tetrahedron method with Blöchl corrections [65].

3.3 Results

3.3.1 Phonons

Figure 3.2 shows the calculated phonon dispersion curves for $Pm\bar{3}m$ Li_3OCl as calculated using force constants fit to force-displacement relationships obtained from DFT-PBE calculations on a $6 \times 6 \times 6$ supercell of the cubic unit cell. We also show the dispersion curves using force constants extracted from a $3 \times 3 \times 3$ supercell. Because Li_3OCl is an ionic crystal, contributions from Born effective charges were included in the calculation of the dispersion curves to account for macroscopic electric fields induced by long-range Coulombic interactions due to dipole moments that emerge from longitudinal optical phonons [17]. This leads to the LO-TO (longitudinal optical - transverse optical) splitting at the Γ point [30, 33]. Oxygen and chlorine occupy sites having cubic symmetry and therefore have isotropic Born effective charges with values of $-1.98|e|$ and $-1.30|e|$, respectively. The Li ions occupy sites with lower symmetry and have an anisotropic, diagonal Born effective charge tensor with a value of $0.99|e|$ in the direction of the O-Li-O bond and a value of $1.14|e|$ in the plane perpendicular to the O-Li-O bond. The dielectric tensor has diagonal elements of 15.13. The Born effective charges, particularly those of Li and O, are remarkably close to their formal charges, indicating the highly ionic nature of the material.

Figure 3.2 shows that the cubic form of Li_3OCl is dynamically unstable with respect to phonon modes at R and M. The unstable modes, corresponding to imaginary eigenvalues of the dynamical matrix, are represented as negative frequencies in Figure 3.2. The instability at R is three-fold degenerate, indicating that there are three symmetrically equivalent phonon modes that contribute to the decomposition of the cubic phase into a more energetically favorable structure. Figure 3.2 also shows that a phonon mode at M is slightly dynamically unstable when using force constants extracted from a $6 \times 6 \times 6$ supercell, and the same mode is predicted to be even more so when using force constants determined with a $3 \times 3 \times 3$ supercell.

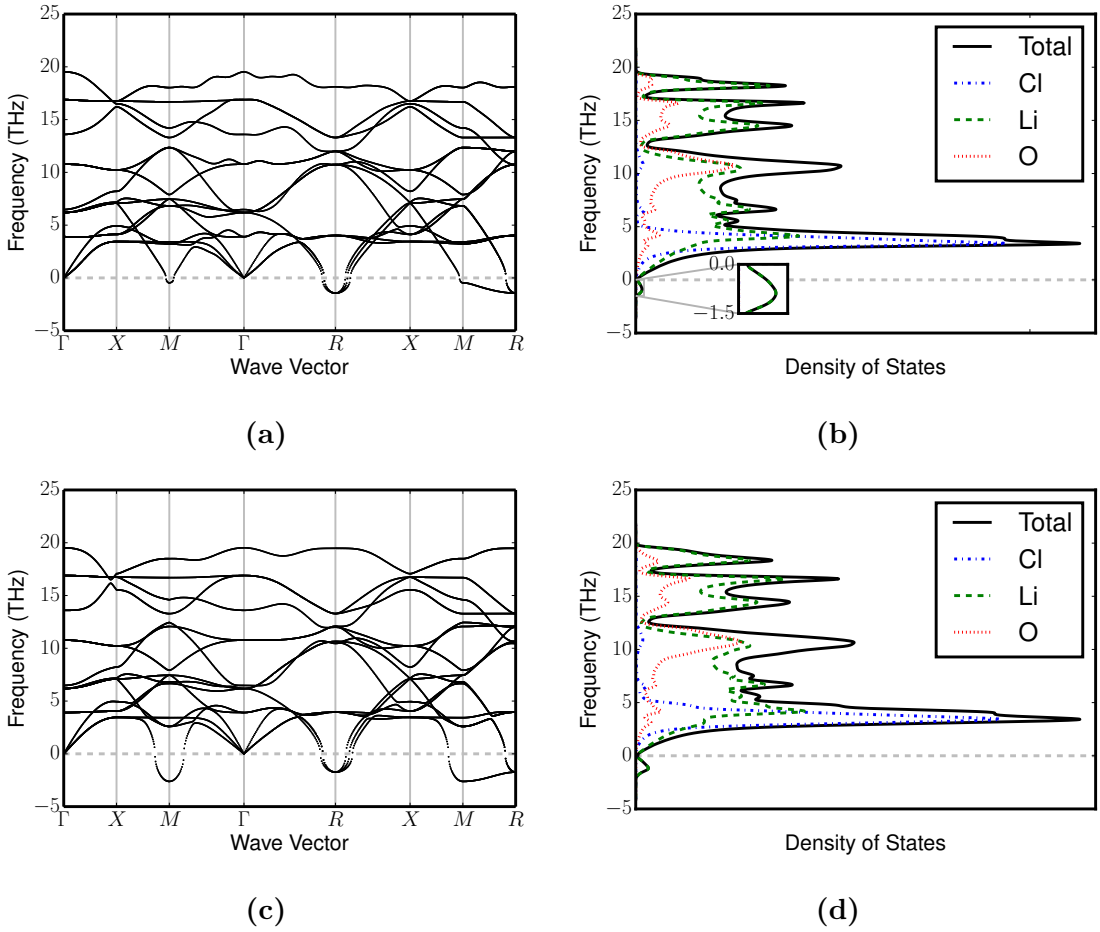

Figure 3.2. (a) Phonon dispersion curve and (b) density of states of $Pm\bar{3}m$ Li_3OCl calculated using the finite displacement method with a lattice parameter of 3.907$\mathring{A}$ and Born effective charge corrections in a $6 \times 6 \times 6$ supercell. (c) and (d) are the dispersion curve and density of states resulting from a $3 \times 3 \times 3$ supercell. There is a 3-fold degenerate instability at the Brillouin zone boundary R point in both supercells, but the smaller supercell results in an instability at the M point as well.

The phonon density of states in Figure 3.2b show that the unstable modes account for a small fraction of the total phonon modes. The partial densities of states in Figure 3.2b indicate that the unstable modes involve only Li ions. The high frequency modes above approximately 5 THz are dominated by oxygen and Li. The Cl anions are about 5 times heavier than Li and reside in the large dodecahedrally coordinated cages characterized by long Cl-Li bonds. As a result, Cl accounts for most of the lower frequency stable modes.

The unstable modes at R indicate that the energy of the crystal can be lowered through octahedral tilts that generate the other 14 tilt systems. A systematic analysis can be accomplished by examining the irreducible representations of the point groups of the first Brillouin zone high-symmetry points [56] of cubic $Pm\bar{3}m$ Li_3OCl. In the antiperovskite structure, the

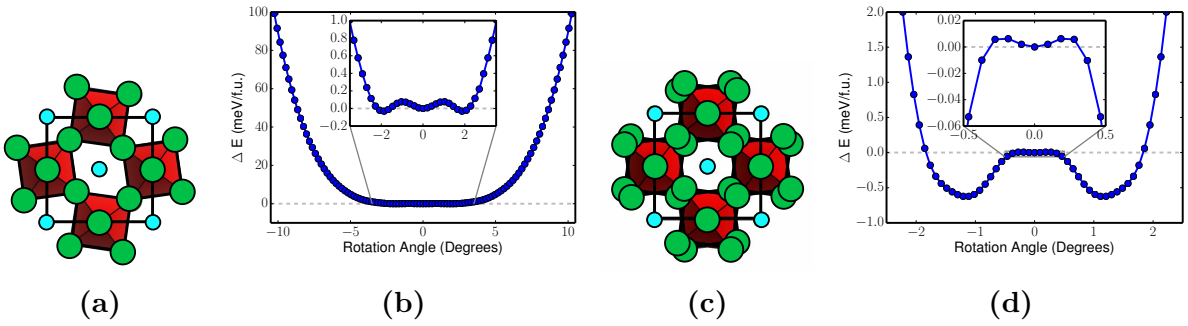

Figure 3.3. Energy variation with Li_6O octahedral rotations. (a) In-phase octahedral rotations due to distortions with M_3^+ symmetry and (b) resulting energy variation. (c) Out-of-phase octahedral rotations and (d) resulting energy variation. Green, red, and blue circles represent Li, O, and Cl atoms, respectively. The zero reference energy is that of the undistorted $Pm\bar{3}m$ structure.

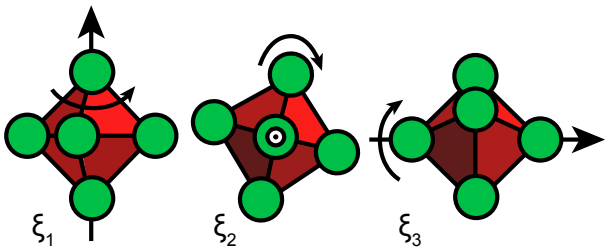

Figure 3.4. Octahedral tilts due to atomic displacements with the irreducible representation symmetry R_4^+. The three-fold degeneracy of R_4^+ leads to three variants of this distortion, where each variation is an octahedral rotation about a different axis.

octahedral rotations result from positional displacements of the Li cations, while the O and Cl anions stay fixed. These rotations can be attributed to a six-dimensional reducible representation of $Pm\bar{3}m$, $M_3^+ \oplus R_4^+$, with M_3^+ and R_4^+ themselves being irreducible representations belonging to high-symmetry points M and R in the first Brillouin zone [58].

Distortions having M_3^+ symmetry can be characterized as rotations of all layers of octahedra around a single axis in a cooperative in-phase motion (Figure 3.3a), resulting in an $a^0a^0c^+$ tilt system and a $P4/mbm$ space group [58]. This tilt periodicity can be realized in a tetragonal supercell made up of two cubic primitive cells. Figure 3.3b shows the dependence of the energy of the crystal as the angle of rotation is incrementally increased. The energy well is highly anharmonic for small rotation angles varying by less than 0.2 meV over a two degree interval and exhibiting three local minima. The two minima at non-zero rotation angle correspond to structures possessing $P4/mbm$ symmetry.

By doubling the M_3^+ unit cell in the c-axis direction, we effectively create two layers of octahedra that can be rotated in opposing directions, simulating an out-of-phase rotation between the two layers (Figure 3.3c). This distortion leads to the formation of a $a^0a^0c^-$ tilt

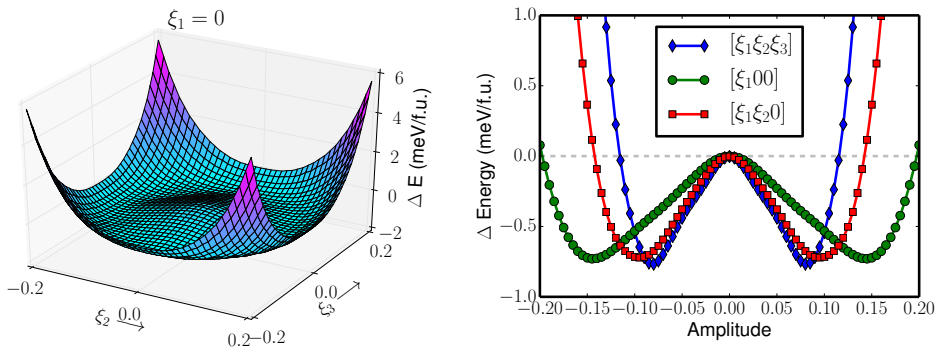

(a) **(b)**

Figure 3.5. Energy variations due to distortions with R_4^+ symmetry with Pm$\bar{3}$m as the energy reference. (a) The energy landscape of an $\xi_1 = 0$ slice of the 3-D ξ_x space. The landscape is very flat, with the energy scale around the wells being on the order of 1 meV/f.u. (b) Amplitude dependent energies in the [111], [110], and [100] directions of the ξ_x space leading to the formation of $R\bar{3}c$, $Imma$, and $I4/mcm$ structures.

system with a space group of $I4/mcm$. While the energy wells are slightly deeper than those of the M_3^+ rotation, the depth of the energy wells remain well above -1 meV per f.u. As is clear in Figures 3.3b and 3.3d, M_3^+ is indeed a stable mode, but both Figures 3.2c and 3.2a exhibit a relatively soft branch at M. This correlates with the ease at which the structure falls into the 2 energy minima when the M_3^+ distortion is applied.

At the R point, the R_4^+ representation is 3-fold degenerate, and each mode results in a rotation along a different pseudo-cubic axis (Figure 3.4). Defining the amplitudes of each of these rotational variants as order parameters ξ_1, ξ_2, ξ_3, we sampled distortions over a uniform grid in this three-dimensional space and calculated the energy landscape. A $\xi_1 = 0$ slice in the $\xi_1 - \xi_2 - \xi_3$ space is shown in Figure 3.5a. Similar to the M_3^+ rotations, the energy scales in the $\xi_2 - \xi_3$ space are extremely small, and the depth of the wells occur within 1 meV. Global energy minima are found along the [111] direction of the $\xi_1 - \xi_2 - \xi_3$ space. Taking two-dimensional slices along the [111], [110], and [100] directions in the $\xi_1 - \xi_2 - \xi_3$ space, we see in Figure 3.5b that while the lowest energy well occurs along [111], corresponding to an equal angle of rotation along each axis, it is less than half an meV lower than the energy wells along the [110] and [100] directions. We note that the minimum energy structures along the [111], [110], and [100] directions have space groups of $R\bar{3}c$, $Imma$, and $I4/mcm$, respectively. These space groups in turn correspond to the $a^-a^-a^-$, $a^0b^-b^-$, and $a^0a^0c^-$ tilt systems, which is consistent with conclusions drawn from previous group-theoretical analysis [56, 66].

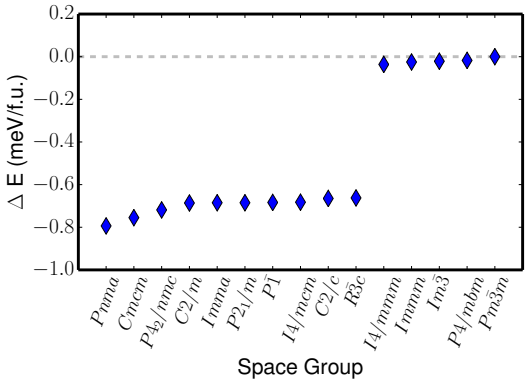

Figure 3.6. Energies of Li_3OCl in the 15 tilt systems. The $Pm\bar{3}m$ structure was used as the reference. All distortions were calculated in a $2 \times 2 \times 2$ supercell of the primitive cell to minimize k-point errors. The energies are within 0.8 meV of the perfect cubic structure.

3.3.2 Stability of $Pm\bar{3}m$ Li_3OCl Relative to 14 Rotational Tilt Systems

Figure 3.6 shows the calculated energies of all 14 tilt systems relative to $Pm\bar{3}m$ Li_3OCl. The energies were calculated using the same $2 \times 2 \times 2$ supercell of the cubic primitive cell using an identical k-point mesh for each structure. All structures were allowed to relax fully. The space groups before and after relaxation were unchanged for each structure as verified using FINDSYM [64].

Of the 14 tilted structures, 10 have lower energy than the cubic $Pm\bar{3}m$. While Figure 3.6 shows that the introduction of octahedral tilts can lower the energy of the cubic antiperovskite, it is important to note, however, that the energy differences between all 15 structures are within 1 meV per f.u. of each other. Despite minimizing k-point errors by using the same supercell for all calculations, the energy differences are small and still well within the numerical error range of first-principle calculations. The 15 different tilt systems in Li_3OCl are therefore energetically indistinguishable, and it is impossible to unambiguously identify the most stable tilt system. It is also unlikely that the system will remain trapped in one of these lower symmetry distortions at all but the lowest temperatures.

3.3.3 Stability of Li_3OCl Relative to LiCl and Li_2O

Li_3OCl at zero Kelvin is predicted to have a positive formation energy relative to a two phase mixture of Li_2O and LiCl [7]. It is therefore not stable at zero Kelvin. It may, however, become entropically stabilized at elevated temperatures as a result of vibrational excitations. The unstable modes of cubic Li_3OCl corresponding to the imaginary (negative) frequencies in Figures 3.2a and 3.2c pose challenges to calculating free energies at finite temperature using

either the harmonic or quasi-harmonic approximation. The energy landscapes as a function of the amplitudes of the unstable phonon modes in Figures 3.3 and 3.5 reveal a substantial degree of anharmonicity with respect to Li_6O octahedral rotational degrees of freedom. While instabilities and anharmonicity in materials have been extensively studied [67, 68] and can be treated using first-principles parameterized anharmonic lattice-dynamical Hamiltonians together with Monte Carlo simulations [69–72], these approaches are highly involved. Here we estimate the free energy of Li_3OCl within the quasi-harmonic approximation by integrating over only the stable phonon modes of cubic Li_3OCl and argue that the neglect of unstable (anharmonic) modes should lead to an upper bound of the Li_2O + LiCl to Li_3OCl transition temperature.

To estimate the error incurred when calculating the free energy of a dynamically unstable high symmetry phase by integrating only over stable phonon modes, it is convenient to formally express the Born-Oppenheimer potential energy surface in terms of the amplitudes of phonon normal coordinates, $\xi_{\mathbf{k},b}$, where as usual, $\mathbf{k}$ refers to a wave vector and b to a phonon branch. The potential energy surface can then be expressed as a polynomial expansion of the phonon normal coordinate amplitudes as, for example, described by Monserrat et al [73]. We can distinguish between two categories of phonon modes in such an expansion. For stable and stiff modes, the harmonic approximation should be suitable, and only terms up to second order need to be kept in the expansion. We will denote the amplitudes of these normal coordinates with $\xi^H_{\mathbf{k},b}$. For unstable or soft phonon modes, anharmonicity is important and polynomials of their amplitudes beyond the second order are needed to reproduce the full potential energy surface. We denote the amplitudes of these phonon modes with $\xi^A_{\mathbf{k}',b'}$. The potential energy surface can then formally be written as

$$V\left(\{\xi^H_{\mathbf{k},b}\},\{\xi^A_{\mathbf{k}',b'}\}\right) = \sum_{\mathbf{k},b}\frac{1}{2}\omega^2_{\mathbf{k},b}(\xi^H_{\mathbf{k},b})^2 + V^A\left(\{\xi^A_{\mathbf{k}',b'}\}\right). \tag{3.1}$$

where the $\xi^A_{\mathbf{k}',b'}$ appearing in the anharmonic potential $V^A(\xi^A_{\mathbf{k}',b'})$ may even be coupled to each other. With this partitioning, it is next convenient to split the full vibrational Hamiltonian, including the kinetic energy, into a sum of a harmonic part H^H and an anharmonic part H^A

where

$$H^H = \sum_{\mathbf{k},b} \left(\frac{(\dot{\xi}^H_{\mathbf{k},b})^2}{2} + \frac{1}{2}\omega^2_{\mathbf{k}} (\xi^H_{\mathbf{k},b})^2 \right) \tag{3.2}$$

$$H^A = \sum_{\mathbf{k}',b'} \frac{(\dot{\xi}^A_{\mathbf{k}',b'})^2}{2} + V^A \left(\{\xi^A_{\mathbf{k}',b'}\} \right). \tag{3.3}$$

Since H^H and H^A are decoupled from each other, they can be solved separately. The harmonic Hamiltonian will have energy levels $E^H_\nu = \sum_{\mathbf{k},b} \hbar\omega_{\mathbf{k},b} \left(n_{\mathbf{k},b} + 1/2\right)$ where the $n_{\mathbf{k},b}$ are integer quantum numbers. Formal solutions to the anharmonic Hamiltonian will generate a spectrum of energy levels $E^A_0, E^A_1, \ldots, E^A_{\nu'}, \ldots$, where E^A_0 corresponds to the ground state energy of the anharmonic Hamiltonian. The energy of any particular vibrational microstate η of the full crystal is then

$$E_\eta = E^o_{\text{cubic}} + \sum_{\mathbf{k},b} \hbar\omega_{\mathbf{k},b} \left(n_{\mathbf{k},b} + 1/2\right) + E^A_0 + \Delta E^A_{\nu'} \tag{3.4}$$

where E^o_{cubic} is the fully relaxed energy of cubic Li_3OCl and $\Delta E^A_{\nu'} = E^A_{\nu'} - E^A_0$ (which is always ≥ 0).

Substitution of Eq. 3.4 into the partition function $Z = \sum_\eta \exp(-\beta E_\eta)$ and using $F = -(1/\beta) \ln Z$ yields a free energy F that can be written as a sum of a harmonic vibrational free energy F^H and an anharmonic free energy contribution F^A. An explicit expression for F^H can only be derived once a criterion is established to distinguish between the phonon modes appearing in the harmonic Hamiltonian and those appearing in the anharmonic Hamiltonian. Here we assume that all stable phonon modes fall in the first category while all unstable phonon modes fall in the second category. The free energies can then be written as

$$\begin{aligned} F^H &= E^\circ_{\text{cubic}} + E^H_{\text{zp}} \\ &\quad + \frac{1}{\beta} \int_0^\infty g(\omega) \ln \left(1 - \exp\left(-\beta\hbar\omega\right)\right) d\omega \end{aligned} \tag{3.5}$$

and

$$F^A = E^A_0 - \frac{1}{\beta} \ln \left(\sum_{\nu'} \exp\left(-\beta \Delta E^A_{\nu'}\right) \right). \tag{3.6}$$

E^H_{zp} appearing in Eq. 3.5 refers to the zero point energy of the harmonic Hamiltonian and is

given by

$$E_{\text{zp}}^{H} = \int_0^\infty \frac{1}{2} g(\omega) \hbar\omega d\omega \tag{3.7}$$

where $g(\omega)$ is the density of states.

The harmonic free energy F^H can be calculated numerically given the vibrational density of states $g(\omega)$ (Figure 3.2b and 3.2d) by integrating over solely the stable phonon frequencies in the Brillouin zone. The anharmonic contribution F^A due to the presence of soft, unstable modes, however, is not as accessible. It consists of a temperature independent term E_0^A which could be positive or negative and a temperature dependent term, $-k_B T \ln\left(\sum_{\nu'} \exp\left(-\beta \Delta E_{\nu'}^A\right)\right)$, which is always negative. The second term of F^A, therefore, lowers the total free energy and gives it a more negative slope as a function of temperature compared to that of F^H. If E_0^A is zero or negative, then the true free energy F will be less than F^H at all temperatures. If E_0^A is positive, however, its inclusion in the estimate of F will result in a rigid upward shift of the free energy curve as a function of temperature relative to F^H.

The order of magnitude of E_0^A can be estimated by comparing the zero Kelvin component of the free energy of cubic Li_3OCl, $E_{\text{cubic}}^o + E_{\text{zp}}^H + E_0^A$, to the zero Kelvin free energy of a dynamically stable tilted variant of cubic Li_3OCl. The lower symmetry $I4/mcm$ form of Li_3OCl, for example, is dynamically stable. Within the harmonic approximation, its free energy at zero Kelvin is equal to the fully relaxed energy $E_{I4/mcm}$ plus its zero point energy $E_{I4/mcm}^{\text{zp}}$. The two free energies at zero Kelvin should be very similar, if not equal, i.e.

$$E_{\text{cubic}}^o + E_{\text{zp}}^H + E_0^A = E_{I4/mcm} + E_{I4/mcm}^{\text{zp}} \tag{3.8}$$

provided that the harmonic approximation at zero Kelvin is valid for the $I4/mcm$ form of Li_3OCl and that the decomposition in harmonic and anharmonic free energies is sufficiently accurate for the cubic form of Li_3OCl. Based on Eq. 3.8 and a calculation of the phonon density of states for the $I4/mcm$ form of Li_3OCl, we estimate a value for E_0^A of approximately 5 meV per Li_3OCl formula unit. Although E_0^A is positive, its magnitude still suggests that E_0^A has a negligible contribution to the total free energy F of cubic Li_3OCl and that F^H can therefore serve as an upper bound to the true free energy of Li_3OCl. The transition temperature for the LiCl plus Li_2O reaction to Li_3OCl using F^H instead of F should therefore serve as an upper bound to the true transition temperature.

We estimate the temperature at which Li_3OCl is stabilized relative to LiCl and Li_2O by first conducting quasi-harmonic calculations for all three phases. The quasi-harmonic

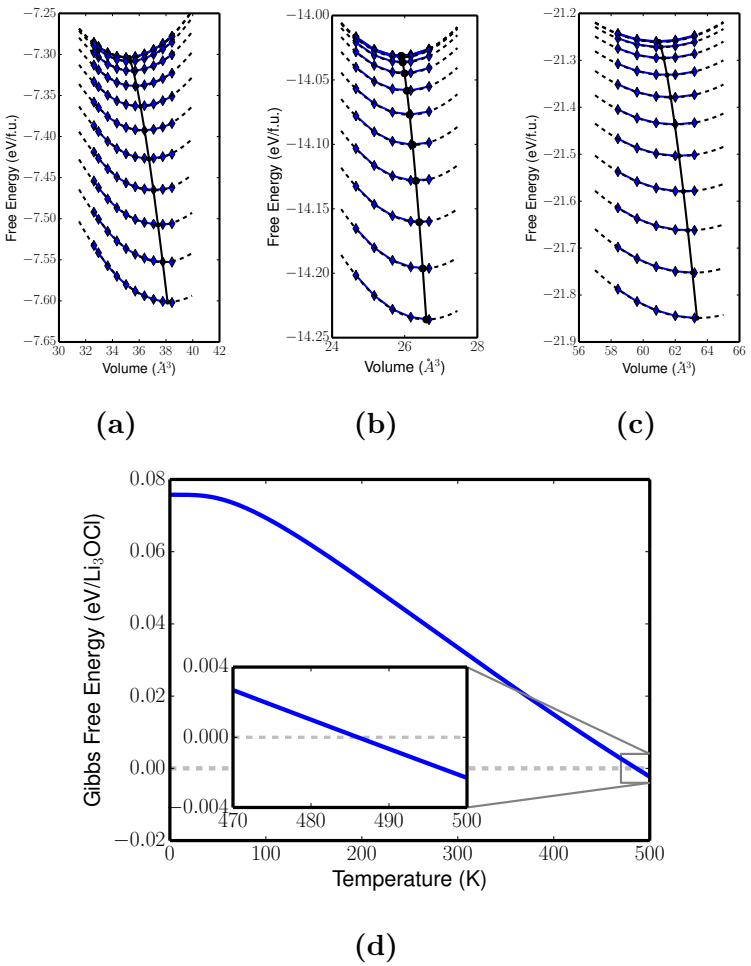

Figure 3.7. Quasi-harmonic curves for (a) LiCl, (b) Li_2O, and (c) Li_3OCl and (d) free energy curve for Li_3OCl. Volume-free energy curves are at increments of 50 K between 0 - 500 K. Li_3OCl is entropically stabilized at 486 K, which is an upper-bound approximation.

approximation, unlike the purely harmonic model, accounts for thermal expansion by constructing volume dependent free energies. These volume and temperature dependent free energy curves, $F(T,V) = E(V) + F^H(T,V)$, consist of the energy of a static lattice at a particular volume, V, and the harmonic vibrational free energy at the same volume. Minimizing $F(T,V)$ with respect to V results in the Gibbs free energy at zero pressure. Harmonic phonons were calculated at volumes both larger and smaller than the equilibrium volume for LiCl, Li_2O, and Li_3OCl. Both LiCl and Li_2O were predicted to be dynamically stable, having only real phonon frequencies. The phonon density of states corresponding to the real vibrational frequencies were used to obtain $F^H(T,V)$ for each of the three phases, which are shown in Figures 3.7a, 3.7b, and 3.7c.

In determining the force constants at different volumes for the quasi-harmonic free energies of Li_3OCl, we used a $3 \times 3 \times 3$ supercell (containing 135 atoms) as opposed to the

substantially larger $6\times6\times6$ supercell (containing 1080 atoms) used to extract force constants for our initial phonon analysis. The dispersion curves resulting from the force constants extracted from the $3\times3\times3$ supercell exhibit softer modes both at R and M (Figure 3.2c) than those based on a $6\times6\times6$ supercell. This is likey due to the sampling of anharmonic modes and the ease with which a slight 1° rotation of the Li_6O octahedra nudges the system into a lower energy state. Note in Figure 3.2d that the soft mode contribution to the total density of states is very small. Using the Gibbs free energies for each of the three compounds, we can calculate a formation free energy for Li_3OCl, $\Delta G_{Li_3OCl} = G_{Li_3OCl} - G_{LiCl} - G_{Li_2O}$. Figure 3.7d, shows that an upper bound temperature at which Li_3OCl is stabilized is approximately 480 K. Errors of $+/-1$ meV per formula unit of Li_3OCl bring the transition temperature within a range of 475 - 487 K, while errors of $+/-5$ meV per formula unit of Li_3OCl result in bounds of 450 - 510 K.

3.4 Discussion

Li_3OCl shows promise as a solid electrolyte for Li-ion batteries [6]. It is, however, predicted to have a positive formation energy relative to a two-phase mixture of LiCl and Li_2O [7,54]. Furthermore, to ensure a high concentration of diffusion mediating defects, the compound must be synthesized with a composition that deviates from perfect stoichiometry as the energy to form Frenkel pairs in the stoichiometric compound is too high to generate a sufficient number of Li interstitials and vacancies at room temperature [7]. A deeper understanding of the factors responsible for the observed stability of Li_3OCl is therefore desirable.

Our analysis of the phonon modes of Li_3OCl shows that its cubic form is dynamically unstable with respect to Li_6O octahedral rotations. The instability occurs at the R wave vector points and leads to the spontaneous decomposition of $Pm\bar{3}m$ Li_3OCl into lower energy tilt systems, which has been observed in other perovskite materials [61,74]. Li_3OCl is highly anharmonic with respect to rotational degrees of freedom of the Li_6O octahedra. The energy landscape as a function of unstable phonon modes of cubic Li_3OCl is very shallow (Figure 3.5a) with the energy differences between cubic and lower symmetry tilt systems being too small to establish which distortion is more stable (Figure 3.6). It is therefore unlikely that any of the lower symmetry tilt variants of Li_3OCl will be stable at any but the lowest temperatures, becoming cubic when sufficient thermal energy is available to overcome the small energy barriers separating the various low symmetry variants.

The ionic radius of Cl relative to Li and O is consistent with the Goldschmidt rule [75] for cubic perovskite stability with respect to rotational instabilities of the Li_6O octahedra.

General guidelines indicate that a cubic structure is preferred for a tolerance factor, defined for an ABX_3 perovskite as

$$t = \frac{(R_A + R_X)}{\sqrt{2}\,(R_B + R_X)}, \tag{3.9}$$

between $0.9 - 1$. The tolerance factor for Li_3OCl is 0.84, based on ionic radii tabulated by Shannon [76]. Substituting Cl with a larger anion should make the cubic perovskite dynamically stable with respect to Li_6O octahedral rotations. Br, for example, which has been alloyed on the Cl sublattice of Li_3OCl to optimize Li conductivity [6,7,55], results in a slightly higher tolerance factor of 0.89 for Li_3OBr. This suggests that Li_3OBr is unlikely to exhibit rotational instabilities.

While our analysis of phase stability due to vibrational excitations does not rigorously account for anharmonicity, it does give a strong indication that Li_3OCl should be entropically stabilized at high temperature. Nevertheless the precise temperature above which Li_3OCl should become thermodynamically stable relative to LiCl+Li_2O is uncertain as our quasi-harmonic model and subsequent analysis only provide an upper bound estimate. Our results, however, indicate that Li_3OCl is very likely stable at typical synthesis temperatures of 330-360°C [6]. Because our free energy calculations relied on the density of states corresponding to stable phonon modes, we were unable to account for the anharmonic contributions to the free energy. The contribution to the total density of states by the imaginary frequencies, however, is relatively small when extracting force constants from frozen phonon calculations using the 1080 or 135 atom supercells of Li_3OCl. This suggests that the inclusion of anharmonic excitations is unlikely to have a strong effect on the predicted temperature above which Li_3OCl becomes stable relative to LiCl and Li_2O.

The phonon analysis of Li_3OCl provides insight about the factors responsible for the high temperature stability of Li_3OCl. As shown in the partial densities of states of Figures 3.2b and 3.2d, the majority of the low frequency modes can be attributed to Cl anions and Li cations, while the majority of high frequency modes involve both Li and O. Cl in Li_3OCl resides in a large cage and is 12 fold coordinated by Li, which is substantially higher than its 6-fold coordination in LiCl. The Li-Cl bond lengths in Li_3OCl are $2.76\mathring{A}$, which are longer than the $2.58\mathring{A}$ Li-Cl bonds in LiCl. Longer bonds tend to be softer, resulting in an increase in vibrational entropy [5]. Hence Cl will gain in vibrational entropy when going from its octahedrally coordinated sites in LiCl to the more open 12-fold coordinated sites in Li_3OCl. Additional vibrational entropy arises from the easy Li_6O octahedral rotations, a degree of freedom that is absent in the more compact LiCl and Li_2O phases.

At practical temperatures for Li-ion battery applications, the Li_6O rotational tilts will be

energetically accessible due to thermal excitations. While these tilts will have consequences for ion transport, it is unclear whether the rotational instabilities will facilitate or hinder Li diffusion. Transition state theory assumes that the initial and final states are dynamically stable, which is not the case here for cubic Li_3OCl. Understanding the role of octahedral rotations on Li diffusion in Li_3OCl, either by a vacancy or interstitial dumbbell mechanism, will require analysis of molecular dynamics simulations at temperatures where the cubic form of Li_3OCl is stabilized by anharmonic vibrational excitations.

3.5 Conclusion

Through a harmonic phonon model we have shown that the cubic $Pm\bar{3}m$ Li_3OCl structure, which has been known to be metastable [7, 54], is mechanically unstable. Aided by group-theoretical analysis, we have identified that a combination of the three degenerate unstable modes with R_4^+ symmetry can result in lower-energy tilt systems. Furthermore, we have explored the energetics of M_3^+, the other irreducible representation known for inducing octahedral rotations. Calculations of the 15 tilt systems showed that while structures involving octahedral tilts have lower energy than cubic $Pm\bar{3}m$, energy differences are too small to identify a single system as most stable. We have also found that Li_3OCl is indeed stabilized by vibrational entropy at temperatures lower than 480 K.

CHAPTER IV

High-Temperature Stability of δ'-ZrO

4.1 Introduction

The oxidation of zirconium alloys has long been of interest as it is an important degradation mechanism of nuclear fuel-rod cladding in water-based reactors. The harsh reactor environments induce waterside corrosion of the Zr-alloy cladding. An experimental understanding of the resulting oxide microstructures is especially important to designing alloys with greater corrosion resistance [9, 77]. Computational efforts can provide further insight into the thermodynamic driving forces behind these complex oxidation processes, which are determined by the relative stabilities of various oxides at high temperatures. While zirconium alloys have been extensively studied, resulting in both experimental [78, 79] and computational phase diagrams [1, 80], new discoveries of the material continue to emerge.

A notable characteristic of the Zr-O phase diagram is the extraordinary oxygen solubility in α-Zr, reported to reach values up to 35 at.% [79]. Various sub-oxide phases are formed at low-temperatures in which oxygen orders over the interstitial sites of α-Zr. At higher temperatures, an α Zr-O solid-solution forms due to the absence of long range oxygen ordering. In calculated phase diagrams [1, 79, 80], there exists an ordered suboxide having $ZrO_{1/2}$ stoichiometry, near the oxygen solubility limit, where the tolerance for vacancies on the oxygen sublattice increases with temperature. At higher oxygen concentrations, the well-studied ZrO_2 polymorphs form. Up to 1478 K, the monoclinic α-ZrO_2 is stable, after which a transformation to tetragonal β-ZrO_2 occurs [78]. At even more elevated temperatures of approximately 1800 K, a non-stoichiometric cubic γ-ZrO_2 becomes stable [79]. In zirconium alloys, this sequence of sub-oxides followed by ZrO_2 has been observed experimentally [81,82]. The formation of these oxides as a function of distance from the oxidation surface is a result of an oxygen chemical potential gradient that exists between the exterior surface, where the oxygen chemical potential is high, and the interior unexposed regions of the nuclear cladding material, where the oxygen chemical potential is low [1].

Recently, a monoxide ZrO phase was discovered experimentally via EELS, atom probe tomography, and electron diffraction [81–83]. Its hexagonal structure was determined with first-principles methods [1] and subsequently confirmed experimentally [83]. This phase was previously identified as a line compound, labeled as δ'-ZrO, in a first-principles calculated phase diagram [1], but as only configurational entropy had been considered, its finite temperature stability limits remain unknown. Determining the stability of δ'-ZrO relative to $ZrO_{1/2}$ and ZrO_2 at elevated temperatures is important due to the high-temperature environments under which nuclear rod claddings are subjected.

Here we examine the stability of Zr-O phases at the nuclear cladding operating temperatures of 300-360° C from first principles by calculating vibrational free energies within the quasi-harmonic aproximation. Previous lattice dynamics studies in the Zr-O binary have focused primarily on the 3 polymorphs of ZrO_2 and their relative stabilities [14, 15, 84]. In this work, we calculated temperature and volume-dependent free energies of α-Zr, $ZrO_{1/2}$, δ'-ZrO, α-ZrO_2 and β-ZrO_2 within the quasi-harmonic approximation and determined that δ'-ZrO is stable to at least as high as 1500 K. Nevertheless, our calculations predict that the oxygen chemical potential window in which δ'-ZrO is stable decreases with increasing temperature due to its lower vibrational entropy relative to that of competing oxides in the Zr-O binary. We also report a prediction of the α to β ZrO_2 transition temperature of 1440 K. With the calculated vibrational free energies, adjustments were made to the phase diagram in Reference [1] to include the contribution of finite temperature vibrational effects.

4.2 Methodology

The Zr-O temperature composition phase diagram was previously calculated using first-principles cluster expansion Hamiltonians and Monte Carlo calculations [1, 80]. While rigorously accounting for configurational degrees of freedom due to oxygan-vacancy disorder over the interstitial sites of hcp Zr, these studies neglected the role of vibrational excitations. Here we build on the phase diagram of [1] by calculating vibrational free energies of key compounds in the Zr-O binary. We are primarily interested in the stability of the newly discovered δ'-ZrO phase at elevated temperature. Whether or not δ'-ZrO remains stable at high temperature depends on the value of its free energy relative to those of $ZrO_{1/2}$ and ZrO_2.

The temperature dependence of the free energies of δ'-ZrO as well as those of α and β-ZrO_2 are primarily determined by vibrational excitations since these phases are line compounds with negligible configurational disorder [1, 79]. While $ZrO_{1/2}$ corresponds to an ordered phase, Monte Carlo simulations [1, 80] have shown that it can tolerate some disor-

der and oxygen off-stoichiometry at high temperature. Hence the temperature dependence of its free energy has contributions from both vibrational and configurational excitations. Although the coupling between configurational and vibrational excitations can be treated rigorously using coarse graining techniques [85], these approaches are computationally prohibitive. Here we estimate the free energy of $ZrO_{1/2}$ by approximating it as a sum of a configurational free energy $G_{\text{config}}(x,T)$ and a vibrational free energy $G_{\text{vib}}(x,T)$. We further assume that the dependence of the vibrational free energy on concentration in HCP based α ZrO_x can be linearly interpolated between that of α Zr and ordered $ZrO_{1/2}$. These approximations should be reasonable for the purpose of calculating the stability of δ' ZrO relative to $ZrO_{1/2}$ and ZrO_2. While $ZrO_{1/2}$ can tolerate a high degree of oxygen off-stoichiometry at elevated temperature, its concentration when in equilibrium with more oxygen rich oxides (i.e. ZrO or ZrO_2) remains very close to that of the stoichiometric compound.

To obtain the vibrational Gibbs free energies, G_{vib}, force constants are needed to construct a lattice dynamics model within the harmonic approximation. The frozen phonon approach was used to calculate force constants for each of the phases. Single atom perturbations were applied in high symmetry directions in large supercells. Forces resulting from these perturbations were obtained through high precision calculations using the Vienna Ab Initio Simulation Package (VASP) [48, 49]. A least squares fit between the displacements and forces was performed to extract force constants that were then used in the construction of the dynamical matrix [5, 12, 17, 18, 31]. First-principles calculations of forces were performed within the generalized gradient approximation (GGA) to density functional theory using the PBEsol parameterization [44]. This parameterization has been shown to be superior to other parameterizations in predicting lattice parameters and phonon properties for ZrO_2 [86]. A 600 eV energy cutoff was used for the plane wave basis. Projector augmented wave [47, 49] pseudopotentials were used having valence-electron configurations of $4s^2, 4p^6, 5s^1, 4d^3$ and $2s^2, 2p^4$ for Zr and O, respectively.

As both α and β forms of ZrO_2 are insulating materials, contributions from long wave length dipole-dipole interactions must be accounted for [13, 29, 30, 36]. These dipole-dipole interactions are not present in either $ZrO_{1/2}$ or δ'-ZrO as they are both metallic [1]. The non-analytical contribution to the dynamical matrix resulting from long-range dipole-dipole interactions was calculated according to the interpolation scheme of Parlinski et al [32]. Born effective charges and dielectric tensors were calculated with a linear response approximation [36] as implemented in VASP [63].

Vibrational free energies within the quasi-harmonic approximation were calculated for Zr, $ZrO_{1/2}$, δ'-ZrO, α-ZrO_2, and β-ZrO_2 by performing harmonic phonon calculations at varying volumes. At each volume, displacements of $0.03\mathring{A}$ were imposed in the $3 \times 3 \times 2$ (36

atoms), $2 \times 2 \times 4$ (96 atoms), $2 \times 2 \times 2$ (72 atoms), and $3 \times 3 \times 3$ (324 atoms) supercells of Zr, ZrO, $ZrO_{1/2}$, and α-ZrO_2 , respectively. Amplitudes of 0.048 and 0.037$\mathring{A}$ were imposed on the O and Zr atoms, respectively, in a $3 \times 3 \times 2$ (108 atoms) supercell of β-ZrO_2. A Monkhorst-Pack [87] k-point mesh of $4 \times 4 \times 4$, $5 \times 5 \times 4$, $7 \times 7 \times 7$, $3 \times 3 \times 3$, and $5 \times 5 \times 5$ was used for each supercell of Zr, ZrO, $ZrO_{1/2}$, α-ZrO_2, and β-ZrO_2 when calculating forces with VASP using DFT-PBEsol. The Gibbs free energy as a function of temperature was calculated by minimizing each iso-thermal, volume-dependent free energy curve via a second order polynomial fit.

4.3 Results

Experimentally, the oxidation of zirconium alloys manifests itself as a sequence of ZrO_x suboxides, a monoxide, and ZrO_2 [81, 82]. Of the ZrO_x suboxides, the ordered phase with the widest region of stability both as a function of oxygen concentration and temperature is $ZrO_{1/2}$. The crystal structures of $ZrO_{1/2}$ and ZrO_2 are well known. The crystal structure of $ZrO_{1/2}$ (Figure 4.1a) consists of an HCP Zr sublattice with oxygen atoms occupying octahedral sites between the triangular close-packed Zr-layers. The other ordered ZrO_x suboxides share the same HCP Zr sublattice with varying oxygen occupation. ZrO_2 forms on the surface of the oxidizing metal due to the high oxygen chemical potential there. In this region, two of the three polymorphs are often observed. One is tetragonal β-ZrO_2, shown in Figure 4.1b, which has O atoms occupying tetrahedral interstitial sites of the tetragonally distorted FCC Zr sublattice, forming an 8-fold coordination around Zr. The Zr in the low-temperature monoclinic α-ZrO_2 polymorph, shown in Figure 4.1c, is 7-fold coordinated by oxygen. While the connectivity of Zr in both α and β-ZrO_2 is that of FCC, in α-ZrO_2, it is highly distorted.

The newly identified δ'-ZrO monoxide phase has hexagonal symmetry with a Zr sublattice identical to ω-Zr. It consists of two distinct layers each denoted by a different shade of green in Figure 4.1d. The first layer is a triangular Zr sublattice while the second layer is a honeycomb Zr sublattice, each outlined with a red and blue dashed line, respectively. Each corner of the triangular sublattice is situated directly above and below the center of each honeycomb. The oxygen are coordinated by 5 Zr atoms, forming a square pyramidal polyhedron, where the O atom is not quite coplanar with the square base of Zr atoms. The purple dashed line in Figure 4.1e shows the outline of this pyramid. The square base of the pyramid is composed of four atoms from the honeycomb layer, while the tip of the pyramid belongs to the triangular sublattice. The O-Zr bond formed with the apex of the square pyramid is 2.15$\mathring{A}$, shorter than the 2.26$\mathring{A}$ bonds formed with the pyramid base. The

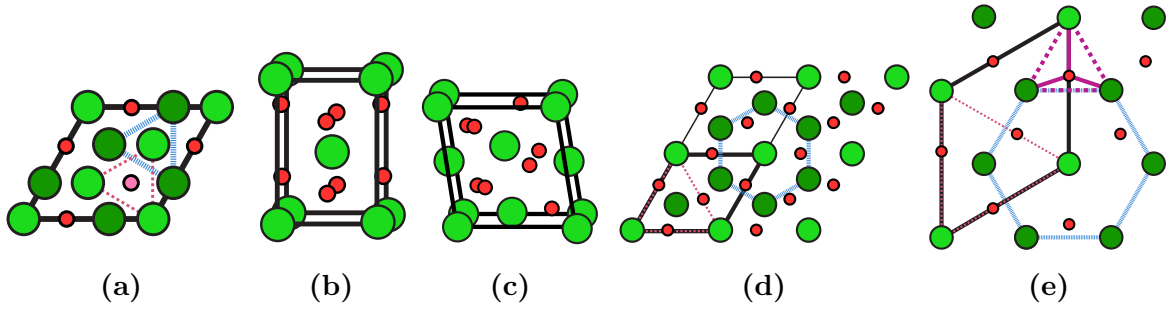

(a) **(b)** **(c)** **(d)** **(e)**

Figure 4.1. Crystal structures of (a) $ZrO_{1/2}$ (b) β-ZrO_2 (c) α-ZrO_2 and (d) δ'-ZrO. The δ'-ZrO oxygen interstitial sites, shown as red squares, and coordination with neighboring Zr are shown in (e). Green and red atoms represent Zr and O, respectively. Different shades of green and red in (a), (d), and (e) differentiate atoms on different layers of the crystal. The triangular and honeycomb sublattices in ZrO are shown in red and blue dashed lines. Different layers of the triangular sublattices of $ZrO_{1/2}$ are also shown in red and blue dashed lines.

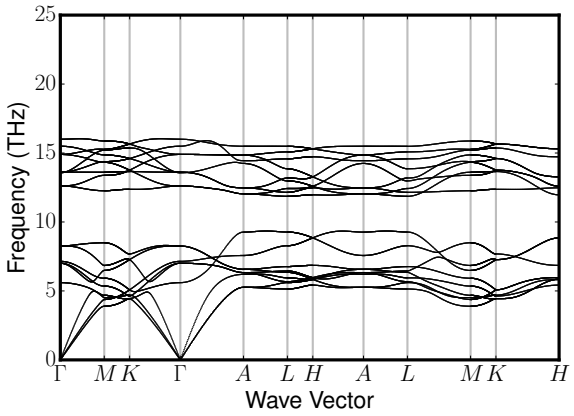

(a)

Figure 4.2. Dispersion curve of δ'-ZrO showing a vibrational band gap.

compact pyramidal coordination of oxygen by Zr suggests that oxygen in δ'-ZrO is tightly bound, which will have implications for the shape of the dispersion curve and density of states.

The phonon dispersion curve and corresponding density of states of δ'-ZrO are shown in Figures 4.2 and 4.3. The most notable feature of the dispersion curve is the vibrational bandgap. The partial density of states (Figure 4.3) shows that the majority of the optical vibrational modes above the gap are dominated by oxygen while the acoustic modes are dominated by Zr. The high oxygen vibrational frequencies suggests that the oxygen are strongly bound within the tight pyramidal coordination geometry of the Zr sublattice. The large separation in vibrational frequencies also arises in part from a large mass difference, with Zr being about 5.7 times heavier than O.

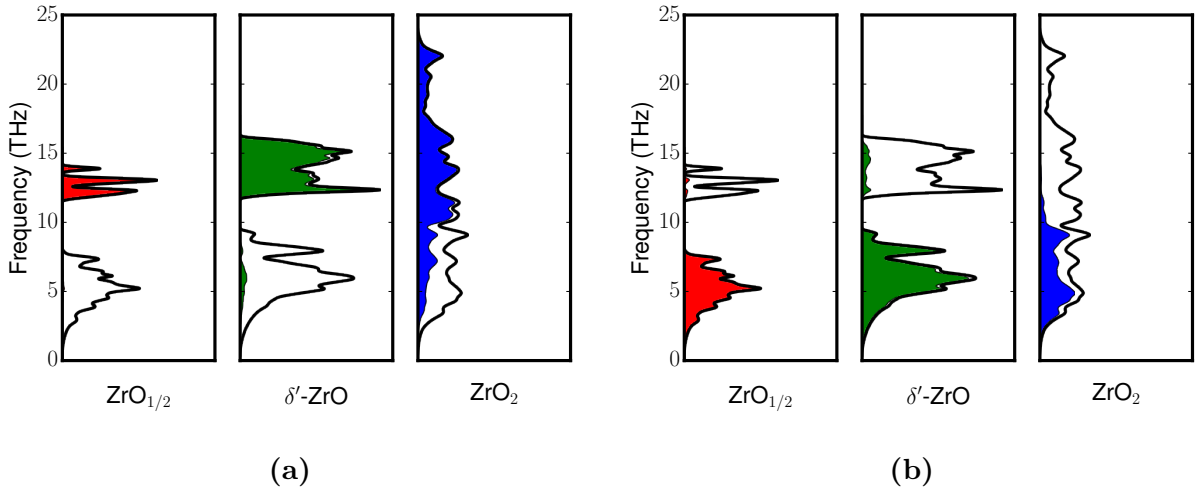

Figure 4.3. (a) Oxygen and (b) zirconium vibrational partial density of states of $ZrO_{1/2}$, δ'-ZrO, and α-ZrO_2. The total density of states is shown by a black outline. For $ZrO_{1/2}$ and δ'-ZrO, there is a clear distribution of oxygen and zirconium vibrational states between high and low frequencies.

The partial densities of states for neighboring phases $ZrO_{1/2}$ and α-ZrO_2 are also shown in Figure 4.3, and their dispersion curves are provided in Supplementary Materials. Similar to δ'-ZrO, Figure 4.3a shows that the oxygen frequencies are well separated from the Zr frequencies in $ZrO_{1/2}$. Compared to $ZrO_{1/2}$, both the oxygen and zirconium frequencies of δ'-ZrO are shifted up. This behavior indicates an overall increase in bond stiffness in δ'-ZrO relative to $ZrO_{1/2}$. In α ZrO_2 the O and Zr vibrational frequencies are more evenly distributed. Nevertheless, the majority of the acousting modes are still dominated by Zr. While some vibrational modes have high frequences the absence of a vibrational band gap in α ZrO_2 ensures that a large fraction of modes dominated by oxygen occur at frequencies below the oxygen vibrational frequencies in $ZrO_{1/2}$ and δ'-ZrO.

A quasi-harmonic analysis was performed to obtain Gibbs free energy curves of several ordered Zr-O phases. Figure 4.4 shows calculated Helmholtz vibrational free energies as a function of volume. By minimizing the isothermal Helmholtz free energies, we obtain G_{vib} at zero pressure for each of the 5 ordered phases. These free energies are superior to those from the harmonic approximation in that finite temperature volume expansion is included in the quasi-harmonic approximation. Figure 4.5 shows both the configurational entropy and the vibrational entropy as a function of oxygen concentration. The configurational entropy was determined by subtracting the internal energy from the free energy, both calculated with Monte Carlo simulations applied to a cluster expansion for the HCP based ZrO_x phase [1]. Minima in the configurational entropy indicate the presence of an ordered phase, the most prominent of which is $ZrO_{1/2}$. The black line denotes the ideal solution entropy multiplied

by the temperature at 1200 K. As the ideal solution entropy corresponds to the maximum configurational entropy, it is always higher than the configurational entropy of a solid with interacting atoms exhibiting some degree of short- or long-range ordering. As is clear from Fig. 4.5, the vibrational entropy is substantially larger than the configurational entropy. The vibrational entropy per Zr of $ZrO_{1/2}$ is also larger than that of α Zr, which is consistent with the introduction of more vibrational degrees of freedom upon insertion of oxygen.

At finite temperatures, vibrational entropy begins to play a role in the relative stabilities of phases. The effect on $ZrO_{1/2}$ and δ'-ZrO at elevated temperatures, for example, can be seen in Figure 4.7, where the formation vibrational entropies (per Zr) for both phases relative to α-Zr and α-ZrO_2 are shown. The formation entropies for both phases are negative. Hence the formation of either $ZrO_{1/2}$ or δ'-ZrO from a two phase mixture of Zr and ZrO_2 is accompanied by a reduction in vibrational entropy. The formation vibrational entropy per Zr of δ'-ZrO is even more negative than that of $ZrO_{1/2}$, indicating that with increases in temperature, vibrational entropy stabilizes δ'-ZrO to a lesser extent than it does $ZrO_{1/2}$. This is consistent with the vibrational densities of state of Figure 4.3, which shows that the bonds are stiffer in δ'-ZrO than in $ZrO_{1/2}$.

To incorporate vibrational effects into the phase diagram, we approximated the total free energy G_{total} as a sum of separate configurational G_{config} and vibrational G_{vib} components. Representative total free energies are shown in Figure 4.6. As temperature increases, the vibrational entropy shown previously in Figure 4.5 dramatically lowers the free energy. Application of the common tangent construction at each temperature yields the phase boundaries shown in the phase diagram of Figure 4.8, which now includes both configurational and vibrational entropy. The most notable change to the phase diagram is that δ'-ZrO is now stable at least until 1500 K. The entropic stabilization of $ZrO_{1/2}$ relative to δ'-ZrO observed in Figure 4.7 translates into an increase in the oxygen solubility limit of the $ZrO_{1/2}$ phase. In the phase diagram, the dashed line in the $ZrO_{1/2}$ region denotes the original two-phase boundary as calculated when only considering configurational degrees of freedom. With the addition of vibrational entropy, this boundary has been shifted towards higher oxygen concentrations. At higher oxygen concentrations, the well-known oxide α-ZrO_2 forms and is stable until a temperature of 1440 K. At this temperature, a transformation to the tetragonal β-ZrO_2 is predicted. This temperature is in good agreement with the experimental transition temperature of 1478 K [78].

The relative stability of the various oxides in the Zr-O binary becomes apparent upon inspection of the variation of the oxygen chemical potential with oxygen concentration. Calculated oxygen chemical potentials at 300 and 600 K are shown in Figure 4.9. These are related to the slopes of the Gibbs free energies in Figure 4.6 with respect to the oxygen

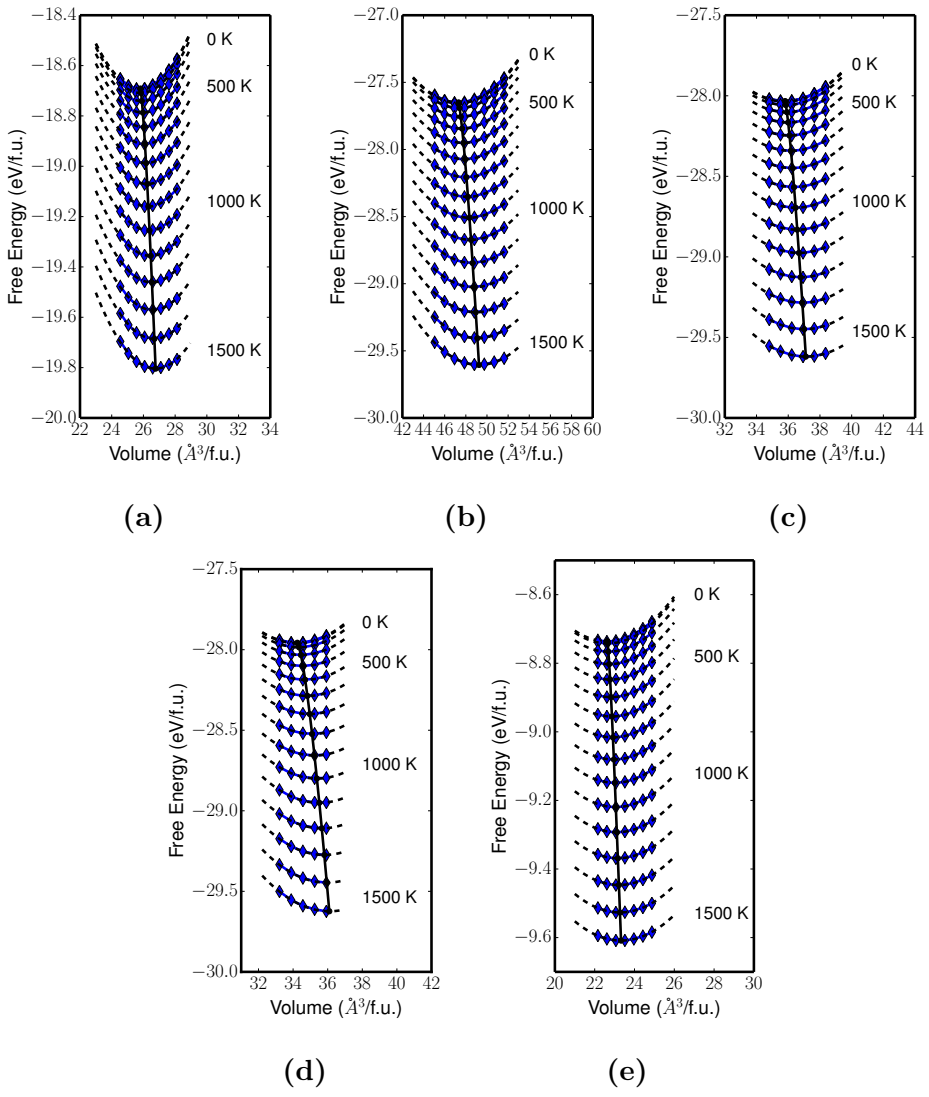

Figure 4.4. Quasi-harmonic volume-dependent free energy curves for (a) δ'-ZrO, (b) $ZrO_{1/2}$, (c) α-ZrO_2 (d) β-ZrO_2, and (e) α-Zr. Curves are shown at increments of 100 K between 0 - 1500 K. The Gibbs free energy obtained by minimizing each isothermal curve was incorporated into the phase diagram in Figure 4.8 to account for finite temperature effects.

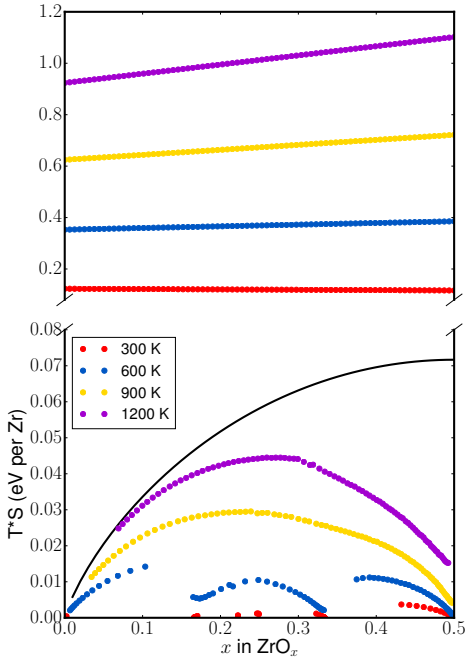

Figure 4.5. Vibrational TS^{vib} (above) and configurational TS^{config} (below) entropies as a function of composition. The black line denotes the ideal solution entropy at 1200 K.

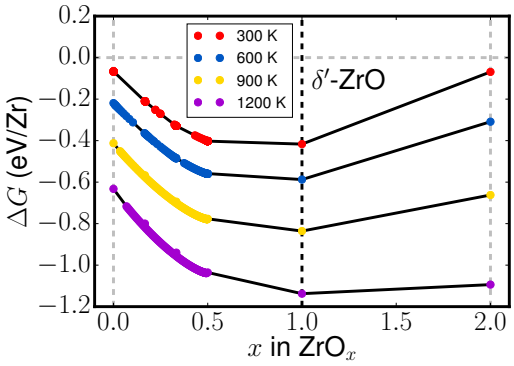

Figure 4.6. Total Gibbs free energy, including both vibrational and configurational contributions, at various temperatures.

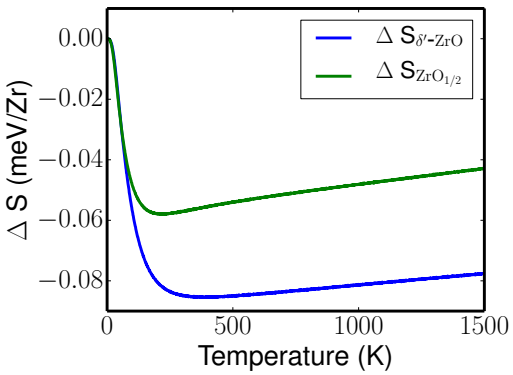

Figure 4.7. Formation vibrational entropy of both δ'-ZrO and $ZrO_{1/2}$ relative to α-Zr and α-ZrO_2, calculated as $\Delta S_{\delta'\text{-ZrO}} = S_{\delta'\text{-ZrO}} - 1/2 S_{ZrO_2} - 1/2 S_{Zr}$ and $\Delta S_{ZrO_{1/2}} = 1/4 S_{ZrO_2} + 3/4 S_{Zr}$. δ'-ZrO is less entropically stabilized at finite temperatures than $ZrO_{1/2}$.

concentration x. Steps in a chemical potential versus concentration plot correspond to stoichiometric compounds, while solid solutions appear as sloping regions. Plateaus signify two-phase regions since the chemical potentials of coexisting phases remain constant in equilibrium. Figure 4.9 shows that the collection of HCP based ZrO_x suboxides as well as α ZrO_2 are stable in wide oxygen chemical potential intervals. δ'-ZrO, however, is stable in only a narrow chemical potential window. Furthermore, the stability window of δ'-ZrO decreases with increasing temperature.

4.4 Discussion

Our first-principles calculation of the vibrational free energies of compounds in the Zr-O binary predicts that newly discovered δ'-ZrO remains thermodynamically stable to temperatures above 1500 K. The updated phase diagram of Figure 4.8 now accounts for both configurational [1] and vibrational degrees of freedom. The phase diagram below $x < 1/2$ remains unaffected by our inclusion of vibrational contributions since we approximated the vibrational free energy between $x = 0$ and $x = 1/2$ as a linear interpolation between the vibrational free energies of α Zr and ordered $ZrO_{1/2}$. Adding a linear term to a free energy curve as a function of concentration does not affect the common tangent construction and will therefore not alter phase boundaries or order-disorder transition temperatures. Since the crystal structure and lattice parameters of HCP based ZrO_x vary negligibly with oxygen concentration [1] we do not expect that a more rigorous inclusion of vibrational degrees of freedom using for example a coarse graining scheme [85] will alter the topology of the phase diagram below $x = 1/2$ much. Inclusion of vibrational contributions does, however, increase

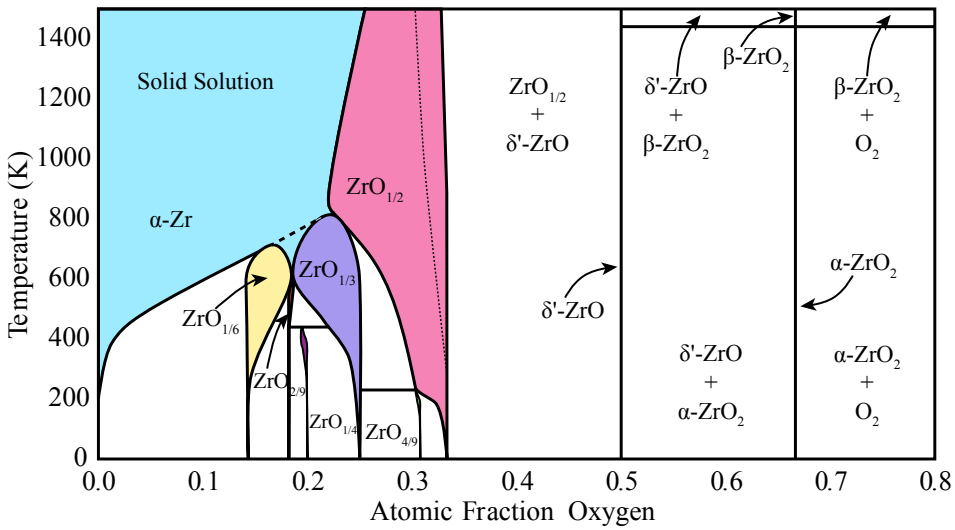

Figure 4.8. Updated Zr-O phase diagram including contributions from both configurational and vibrational excitations. Compared to the original Zr-O phase diagram [1], δ'-ZrO is now shown to be stable to at least 1500 K. Single-phase regions are colored in, while two-phase regions are left white. The boundary between $ZrO_{1/2}$ and the neighboring two-phase region based solely on configurational and excluding vibrational free energies is denoted by a dashed line. The oxygen solubility of oxygen in $ZrO_{1/2}$ increases when contributions from vibrational excitations are also included.

the oxygen solubility limit of ordered $ZrO_{1/2}$ when it coexists with δ'-ZrO. This is due to the low vibrational entropy within δ'-ZrO compared to $ZrO_{1/2}$ and the α and β polymorphs of ZrO_2. Oxygen within the Zr_5O square pyramidal interstitial sites of the ω-Zr sublattice of δ'-ZrO are tightly bound resulting in high frequency optical modes.

As is evident from the updated phase diagram in Figure 4.8, the concentration of ordered $ZrO_{1/2}$ when it coexists with δ'-ZrO is close to ideal stoichiometry. Hence, our linear interpolation scheme to approximate the vibrational free energy of HCP based ZrO_x should be sufficiently accurate for the purposes of assessing the relative stability between δ'-ZrO and $ZrO_{1/2}$ and ZrO_2 at elevated temperature.

The calculated phase diagram of Figure 4.8 shows fair agreement with a previously published phase diagram (between $0 - 1500$ K) as assessed with the CALPHAD approach [79]. The ordered HCP-based phases, $ZrO_{1/6}$, $ZrO_{1/3}$, and $ZrO_{1/2}$, appear in both phase diagrams, although $ZrO_{1/2}$ in Figure 4.8 is predicted to be stable to much higher temperatures [1]. The primary difference between the two phase diagrams is the presence of the recently identified δ'-ZrO line compound.

The relative stability between α and β-ZrO_2 has been investigated before within the harmonic [15] and quasi-harmonic approximation [14]. While the quasi-harmonic study [14]

did not include the effect of long-range dipole-dipole interactions, our calculated vibrational free energies do account for such effects, as did the previous harmonic study [15]. Furthermore, in contrast to prior treatments [14], our harmonic Hamiltonians for α-ZrO_2 did not predict spurious unstable modes (i.e. imaginary frequencies). We believe this is due to our use of significantly larger supercells to extract force constants (324 compared to 108 in a previous study [14]), which have allowed for longer-range force constants to be included in the harmonic Hamiltonian, as Kuwabara et al suspected [14].

Experimental observations [82] of Zr metal-oxide interfaces oxidized at temperatures of 360° C (633 K) have shown narrow regions of ZrO wedged between ZrO_2 and HCP based ZrO_x suboxides (with $x < 1/2$). Zr samples exposed to air will have a gradient in oxygen chemical potential that is high at the surface and that decreases monotonically towards the interior of the sample. While kinetic factors play a role in determining the presence and distribution of different oxide phases in an oxidizing microstructure, the thickness of a particular oxide phase in a monotonically decreasing oxygen chemical potential profile should to a large extent depend on the width of oxygen chemical potential window in which the phase is thermodynamically stable. As is clear from Figure 4.9, δ'-ZrO at x=1 is only stable in a very narrow oxygen chemical potential window. This is consistent with experimental observations that δ'-ZrO appears as much thinner regions compared to ZrO_2 and the collection of HCP based ZrO_x suboxides. Figure 4.9 also shows that the chemical potential stability window of δ'-ZrO decreases with increasing temperature. This suggests that the relative thickness of the δ'-ZrO phase in oxidizing samples will decrease as the temperature is raised. The diminishing relative stability of δ'-ZrO with increasing temperature is a result of its lower vibrational entropy compared to $ZrO_{1/2}$ and ZrO_2.

While our calculation of thermodynamic properties predict that δ'-ZrO remains stable at high temperatures, it does not shed light on the role of this phase in affecting the kinetics of Zr oxidation. Important in this regard is whether the interfaces between the various oxides tend to be coherent, semicoherent or incoherent. The crystallographic nature of the interface will determine how mobile the interface is between a pair of oxides as oxidation proceeds. Another important factor is the oxygen mobility through the different phases. Although oxygen diffusion coefficients in the HCP based ZrO_x suboxides have been predicted to be high at elevated temperature [88], oxygen mobility in the more compact crystal structures of δ'-ZrO will likely be low. δ'-ZrO may therefore act as a diffusion barrier, slowing oxygen ingress in the HCP metal substrate. If this is the case, then it will be desirable to devise strategies that result in a thick δ'-ZrO phase within the oxidizing microstructure. Alloying would have to aim at increasing the energetic stability δ'-ZrO relative to $ZrO_{1/2}$ and ZrO_2 since our current study suggests there is little maneuverability to enhance finite temperature

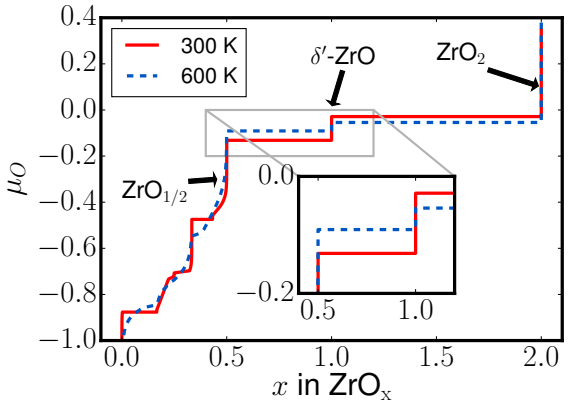

Figure 4.9. Oxygen chemical potential at different temperatures. Single-phase regions have increasing μ_O, while two-phase regions have constant μ_O.

entropic stabilization of the phase.

4.5 Conclusion

Using quasi-harmonic lattice dynamic calculations, we were able to obtain vibrational free energies important to elucidating finite temperature phase stabilities. The phonon dispersion curve and corresponding partial density of states of δ'-ZrO revealed that the O and Zr atoms are tightly bound. In addition to calculating an α-β-ZrO_2 transition temperature of 1440 K, a Zr-O composition-temperature phase diagram complete with configurational and vibrational degrees of freedom was also presented, showing that δ'-ZrO is stable to at least 1500 K. More importantly, the stability of δ'-ZrO relative to $ZrO_{1/2}$ decreases at elevated temperatures due to a relative decrease in vibrational entropy.

CHAPTER V

Dynamical Instabilities of ZrO_2 Polymorphs

5.1 Introduction

Zirconium alloys and their oxides have been studied extensively for their applications in thermal barrier coatings, nuclear rod cladding, and memory storage devices. The oxide ZrO_2 exists in 3 main polymorphs under normal pressures. The low temperature monoclinic phase is stable until 1478 K [78], after which it transforms into a tetragonal phase. At even higher temperatures, a transition to the cubic phase occurs. Under pressurized environments, several orthorhombic phases are known to form. There have been many efforts to stabilize the cubic and tetragonal forms at low temperatures either via strain or doping. For example, the cubic or tetragonal form is stabilized by doping with Y_2O_3 in solid oxide fuel cells and thermal barrier coatings.

The stability and transformation mechanisms of these polymorphs, especially between the cubic and tetragonal phases, have been studied in the context of lattice dynamics [11, 14–16, 25, 84, 89, 90]. Early group-theoretic analysis [11] and subsequent first-principles phonon calculations [12–14] have shown the presence of a soft mode at the X k-point of the cubic Brillouin zone and demonstrated that the cubic phase is mechanically unstable. This unstable mode has been shown [11] to be responsible for a transformation of the cubic phase to the tetragonal phase.

The observed stability of cubic ZrO_2 at elevated temperatures is likely due to anharmonic vibrational excitations. This mechanism has been observed in other mechanically unstable materials, such as ZrH_2 and $BaTiO_2$ [69, 72]. Fabris *et al.* concluded in a tight-binding based lattice dynamics and molecular dynamics study that the cubic ZrO_2 energy landscape is anharmonic at high temperatures and that the phase is entropically stabilized [91]. Carbogno *et al.* found that thermal excitations induce spontaneous switching between tetragonal orientations [86]. At even higher temperatures, each tetragonal orientation is sampled and

the observed cubic form exists as a thermodynamic average of all three tetragonal displacement orientations [86], further confirming the anharmonic vibrational stabilization of the mechanically unstable cubic phase.

The tetragonal ZrO_2 phase exists as three variants, which has been experimentally observed [92,93]. The coexistence of the three tetragonal variants, in addition to the ability of a domain with one variant to reorient into another variant is a characteristic utilized in ferroelastic toughening [94]. In a material where one or more tetragonal variants coexist, when a tensile force is applied near a crack, the tetragonal domains within the vicinity reorient themselves parallel to the tensile direction. The reorientation of these domains result in a compressive strain field surrounding the crack, effectively stopping further crack propagation. This toughening mechanism results in microstructures where two tetragonal variants coexist as twins. To model this type of phase transformation, a model at the continuum level is required. First-principles calculations can be used to calculate free energies that can then be input into a continuum-level model. An accurate description of these free energies requires two descriptors. The first describes the internal atomic positions associated with each tetragonal variant. The second describes the external strain, which varies continuously from one domain into another. Such a framework will be presented and discussed in this chapter.

Group-theoretic techniques applied to tetragonal ZrO_2 [25] have suggested that the phonon modes at the M k-point of the tetragonal Brillouin zone boundary lead to a transformation to the monoclinic structure. A pair potential model [90] also predicted a softening of a mode at M as the separation distance between oxygen atoms increases. Subsequent lattice dynamic studies of the tetragonal phase [14,15], however, have shown that this phase is dynamically stable. The low temperature monoclinic phase has also been shown to be mechanically stable [15,16], with the exception of the study performed in reference [14].

In this chapter, we will examine instabilities of the three ZrO_2 polymorphs. We will begin with a discussion on the cubic mechanical instability that leads to a transformation into the tetragonal phase. The effect of a volume increase on the stability of tetragonal ZrO_2 will also be presented, where we show the discovery of a new orthorhombic phase. The effect of strain on the stability of different tetragonal variants will also be examined within the framework of modeling twinned microstructure resulting from ferroelastic toughening. Finally, the strain-induced instabilities of tetragonal and monoclinic will also be discussed.

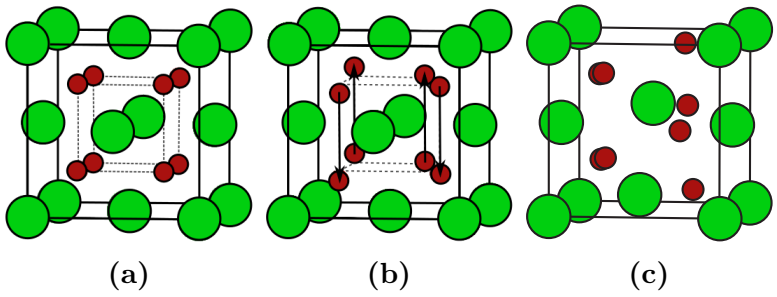

Figure 5.1. (a) Cubic, (b) tetragonal, and (c) monoclinic internal disorder in a cubic lattice.

5.2 Results

5.2.1 Dynamical Instability of Cubic ZrO_2

The internal atomic orderings of the three ZrO_2 polymorphs can be better understood by examining them in the same 12 atom cubic lattice, as shown in Figure 5.1. The cubic phase has an FCC Zr sublattice, with oxygens occupying tetrahedral interstitial sites. The oxygens have a cubic connectivity within the conventional unit cell, as shown by the red atoms in Figure 5.1a. The Zr ordering of the tetragonal phase in this cubic lattice is identical to the cubic phase, but the oxygens are shuffled both up and down along the z-axis such that pairs of atoms at opposite corners of the oxygen cube are displaced along the same direction (Figure 5.1b). The monoclinic phase exhibits much more disorder (Figure 5.1c). The lattice corners are still occupied by Zr atoms, but the Zr at the face centers are displaced inwards. The oxygen ordering bears little resemblance to the ordering in the tetragonal phase.

The crystallographic relationship between the cubic and tetragonal phase is straightforward. The tetragonal internal ordering can be reproduced by displacing the oxygens in cubic ZrO_2 up and down the z-axis. Previous group theory [11] and first-principles [12, 13] studies have shown the presence of an unstable mode in the cubic ZrO_2 dispersion curve, indicating that cubic ZrO_2 is mechanically unstable. This unstable mode at the X Brillouin zone boundary point is represented by negative frequencies in Figure 5.2. The unstable mode suggests that displacements along this mode will push the system into a lower energy state. In fact, these displacements tetragonally shuffle the oxygens, leading to a transformation into the tetragonal phase.

In a perfectly cubic lattice, there are three orientations of this tetragonal oxygen shuffle, each corresponding to shuffles in the three Cartesian coordinate directions. An order parameter description of these tetragonal shuffles can be formulated by first assigning variables λ_3, λ_2, and λ_1 to the x, y, and z shuffle directions. Figure 5.3 shows the energy variation resulting from amplification of λ_1 within a cubic lattice. At $\lambda_1 = 0$, there is no shuffle,

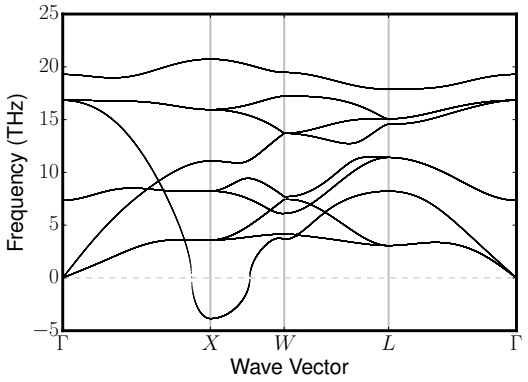

Figure 5.2. Dispersion curve of cubic ZrO_2 showing an unstable mode at X.

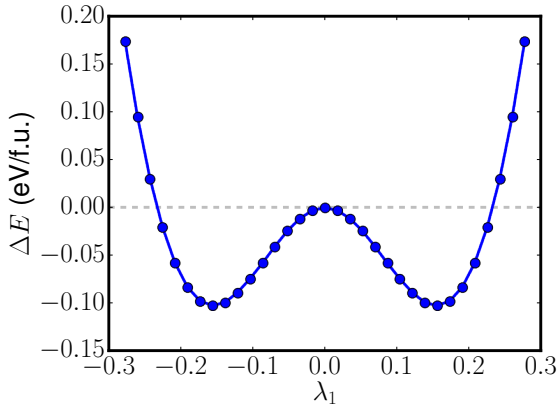

Figure 5.3. Energy variation with λ_1, where λ_1 corresponds to a z-shuffle. Here, the shuffles are imposed in a cubic lattice. $\lambda_1 = 0$ indicates no oxygen shuffle, which corresponds to a cubic oxygen ordering.

and the structure thus has the same internal ordering as the cubic phase. As a z shuffle is imposed, the energy decreases, indicating that the tetragonal internal ordering is preferable. This result supports the result that the cubic phase is mechanically unstable. Despite the dynamical instability of cubic ZrO_2, the observed stability at high temperatures is likely due to anharmonic stabilization [86, 91].

Order parameters η_1, η_2, and η_3 can be defined in terms of these λs as

$$\eta_1 = \frac{\lambda_1 + \lambda_2 + \lambda_3}{\sqrt{3}} \tag{5.1}$$

$$\eta_2 = \frac{\lambda_3 - \lambda_2}{\sqrt{2}} \tag{5.2}$$

$$\eta_3 = \frac{2\lambda_1 - \lambda_2 - \lambda_3}{\sqrt{6}}. \tag{5.3}$$

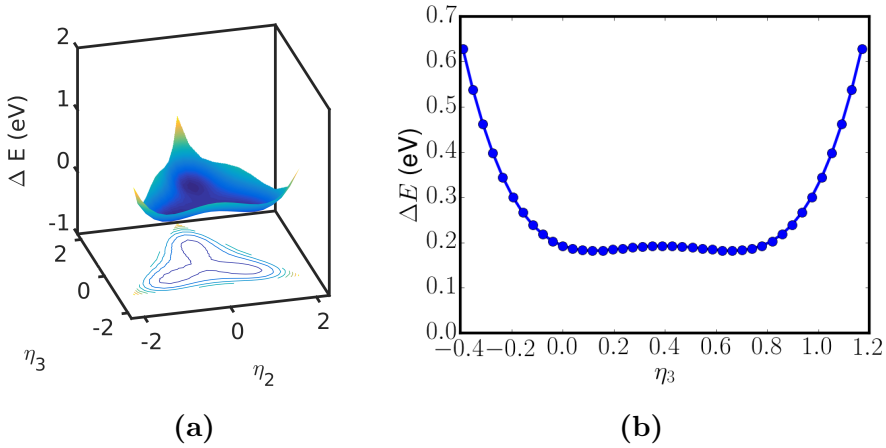

Figure 5.4. (a) η_2-η_3 energy landscape in a cubic lattice. (b) A slice along in η_2-η_3 space connecting the two minima of the energetically equivalent y and x energy wells.

Here, η_1 describes a shuffle amplitude, while η_2 and η_3 correspond to shuffle orientations. The η_2-η_3 energy landscape for these λ shuffles in a cubic lattice is shown in Figure 5.4a. Because the symmetry of the lattice does not dictate a preference for any one tetragonal shuffle orientation, there are three energetically equivalent energy wells. Starting from the well at finite η_3 and $\eta_2 = 0$ and going clockwise, each well corresponds to the dominance of z, x, and y oriented oxygen shuffles. The center of this energy landscape, where $\eta_2 = \eta_3 = 0$, corresponds to a combination of all x, y, z shuffles.

5.2.2 Volume Induced Instability of Tetragonal ZrO_2

Unlike the cubic phase, both tetragonal [14,15] and monoclinic [15] ZrO_2 have been shown to be dynamically stable. The lattice dynamic studies on the monoclinic phase performed in reference [14] revealed an instability near the Brillouin zone center. In our quasiharmonic calculations for the monoclinic phase, we used significantly larger supercells with 324 atoms (compared to 108 atoms used in reference [14]), which eliminated these instabilities. In previous studies, monoclinic-tetragonal transition temperatures within the harmonic [15] and quasiharmonic [14] approximation have predicted monoclinic-tetragonal transition temperatures of 1560 K and 1350 K, respectively. As discussed in Chapter IV, our quasi-harmonic model predicted a monoclinic to tetragonal ZrO_2 transition temperature of 1440 K (Figure 5.5), which is in good agreement with the experimental transition temperature of 1478 K [78]. In performing the quasi-harmonic calculations of the tetragonal phase, it became evident that at larger volumes, acoustic modes at the Z k-point become increasingly unstable. At the tetragonal equilibrium volume, the dispersion curve (Figure 5.6a) is dynamically stable. The dispersion curve of a tetragonal unit cell that is 8% larger than the equilibrium

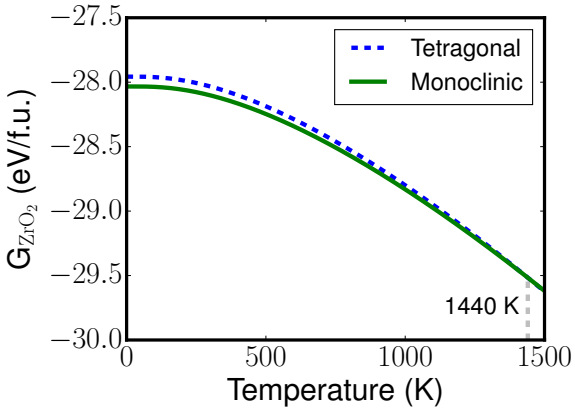

Figure 5.5. Tetragonal and monoclinic vibrational Gibbs free energies. The transition between the two phases occurs at 1440 K, the crossing point between the two curves.

has an instability (Figure 5.6b). In both dispersion curves, discontinuous lines in the optical modes at Γ are characteristic of the LO-TO splitting in ionic materials due to interactions with an external electric field [17]. The instability at Z in Figure 5.6b suggests displacements along the unstable mode will lead to decomposition into another phase that lowers the overall energy of the system. Furthermore, the unstable mode at Z is doubly degenerate, suggesting the existence of at least two symmetrically equivalent lower energy states.

Verification of whether this mode is unstable was accomplished by imposing the displacements of one of the two unstable phonon modes in the ideal crystal. As the unstable mode is at the high symmetry k-point $(0, 0, 0.5)$, a supercell derived by doubling the primitive cell in the c axis direction was necessary to preserve the periodicity of the displacement field. This phonon mode was imposed with increasingly large amplitudes in supercells based on primitive unit cells with volumes ranging from +0% to +10% of the equilibrium volume. The resulting energy curves are shown in Figure 5.7. At the equilibrium volume of +0%, the energy landscape is still fairly parabolic, but as the volume increases to +4%, the energy well flattens and becomes increasingly anharmonic. Starting at about +6%, two minima begin to appear at positive and negative displacements. With further increases in volume, the depth of the two energy wells increases. A similar calculation with the degenerate mode results in energy curves with identical behavior, suggesting that there are 4 variants of this phase.

The displacement field resulting from this unstable Z mode broke the tetragonal symmetry of the structure and resulted in a structure with an internal distortions having orthorhombic $P2_12_12_1$ symmetry. Given the two minima in the energy curve in Figure 5.7 and the double degeneracy of this phonon mode, it follows that four of these orthorhombic

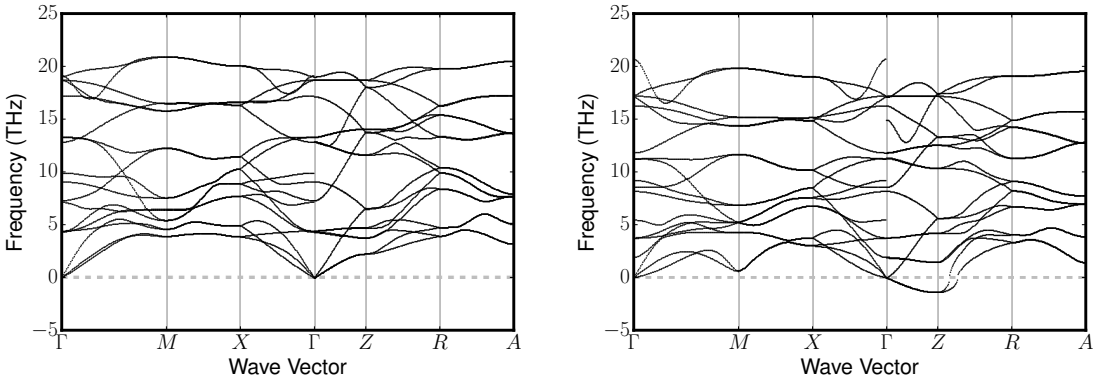

Figure 5.6. Dispersion curves of tetragonal ZrO_2 based on a primitive unit cell that is (a) at the equilibrium volume and (b) +8% larger than the equilibrium volume. In (b) there is an instability at Z, corresponding to the $(0, 0, 0.5)$ point in the irreducible Brillouin zone.

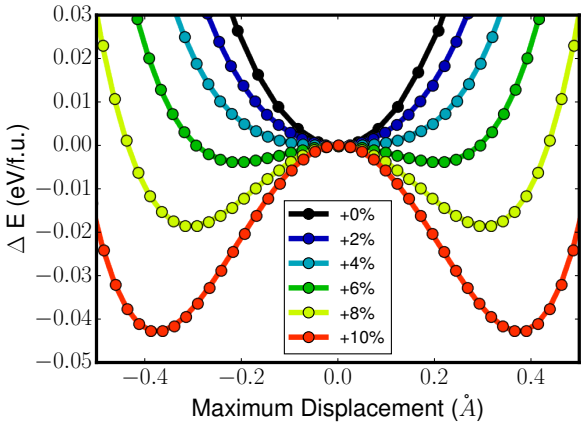

Figure 5.7. Amplifying the displacements due to the unstable phonon mode at Z at volumes incrementally larger than the equilibrium shows that the instability appears around +3% of the equilibrium volume. The energy wells that result from the instability deepen as the volume is increased.

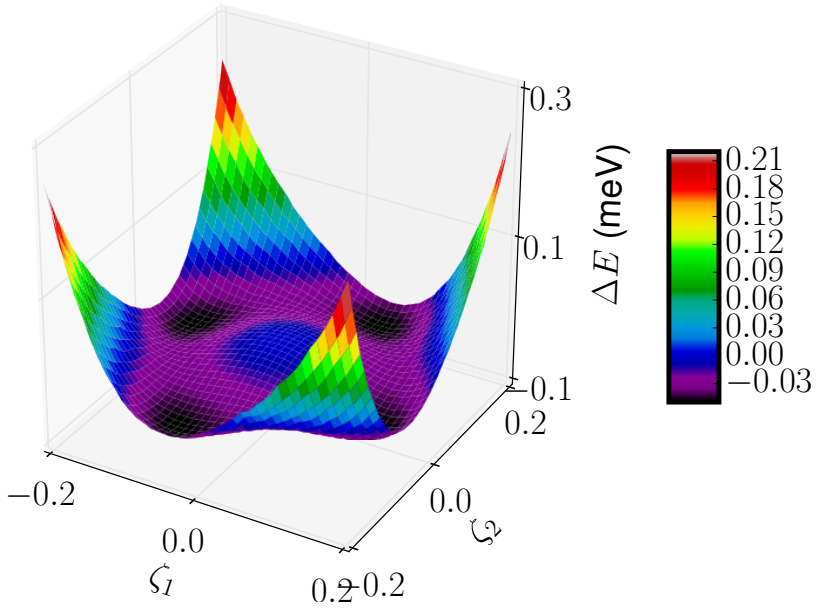

Figure 5.8. Energy landscape in the Z_3 symmetry mode space.

variants can be derived from the tetragonal phase. Denoting the displacements leading to the orthorhombic phase of one mode as ζ_1 and the displacements from the degenerate mode as ζ_2, an energy landscape resulting from combinations of these displacements can be calculated. The energy landscape resulting from displacements in this ζ_1-ζ_2 space is shown in Figure 5.8. The local maximum in the center of the energy landscape is the ideal tetragonal structure. As expected, there are four minima, each corresponding to a minima in the energy wells resulting from displacement of the unstable Z modes. As the energy landscape shows, combinations of displacements ζ_1 and ζ_2 lead to energetically higher structures.

Further inspection of the displacements of this mode shows that the displacements occur only in the a-b plane. As the propagation direction of the phonon mode at Z is in the c direction and the displacements occur in perpendicular directions, the phonon mode is a transverse mode. The transverse mode has little effect on the O and Zr layering in the c axis direction, so these remain largely similar to the parent tetragonal phase. The displacements occurring along the trajectory shown in Figure 5.7 can be described by 4 distinct layers of Zr displacements, as shown in Figure 5.9a. The first layer is composed of Zr atoms displaced in the $-i\hat{\mathbf{a}} - j\hat{\mathbf{b}}$ direction, where $j > i$. The subsequent layer of Zr displacements is in the $-i\hat{\mathbf{a}} + j\hat{\mathbf{b}}$ direction. Zr displacements in the third layer occurs in the $+i\hat{\mathbf{a}} + j\hat{\mathbf{b}}$, which is in the exact opposite direction of the first layer. The fourth and final layer is also in the opposite direction of the second Zr layer.

The oxygen displacements can similarly be described in terms of 4 distinct layers where

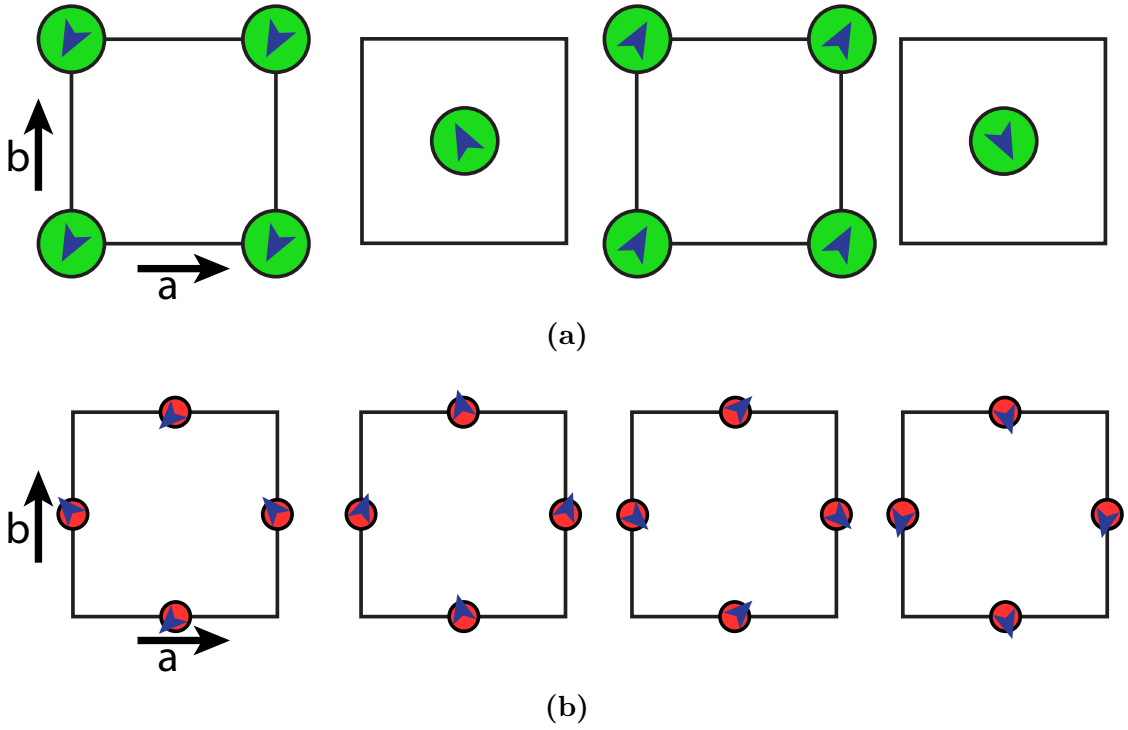

Figure 5.9. Layer-by-layer breakdown of the displacement fields for one of the unstable phonon modes leading to orthorhombic $P2_12_12_1$. (a) Zr atoms and (b) O atoms.

each set of four atoms in a layer belong to either an upper or lower set of 8 tetragonally shuffled oxygens. The first layer has one pair of oxygens displaced in the $-m\hat{\mathbf{a}}+n\hat{\mathbf{b}}$ direction while the other pair is displaced in the $-m\hat{\mathbf{a}}-n\hat{\mathbf{b}}$ direction, where $n > m$. The following layer of oxygen displacements occur in the $+m'\hat{\mathbf{a}}+n'\hat{\mathbf{b}}$ and the $-m'\hat{\mathbf{a}}+n'\hat{\mathbf{b}}$ directions, where again, $n' > m'$. The displacements of the second and fourth oxygen layers are slightly larger than the first and third layers.

The asymmetric displacements in the a-b plane results in an elongation of the b axis and shortening of the a axis, ultimately transforming the tetragonal lattice into an orthorhombic one. By taking the structure at one of the minima of the +10% energy curve in Figure 5.7 and allowing for a full structural relaxation, we found a previously unidentified ZrO_2 orthorhomic phase, shown in Figure 5.11. The space group was identified as $P2_12_12_1$ (Space group #19) using the FINDSYM module of the ISOTROPY Software Suite [64]. This orthorhombic structure has lattice parameters of $a = 3.485\mathring{A}$, $b = 3.861\mathring{A}$, and $c = 10.577\mathring{A}$. There are three Wyckoff positions, which are shown in Table 5.1. The ideal tetragonal unit cell has 2 Wyckoff positions, O $4d$ and Zr $2b$, and the Zr are octahedrally coordinated by oxygen. In this orthorhombic phase Zr, is coordinated by 7 oxygens. The Zr-O polyhedra are mostly edge-sharing in the orthorhombic phase, as are the octahedra in the tetragonal phase. The

Table 5.1. Wyckoff positions of orthorhombic phase $P2_12_12_1$.

Atom	Site	Position
O	4a	(0.2512, 0.4611, -0.0387)
O	4a	(0.2505, -0.3409, 0.2185)
Zr	4a	(-0.2488, 0.3312, -0.1346)

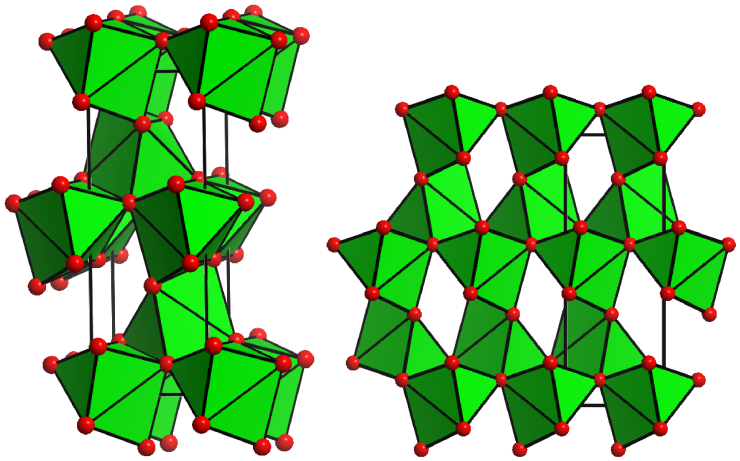

(a) **(b)**

Figure 5.10. Crystal structure of newly identified orthorhombic $P2_12_12_1$ phase.

tetragonal structure is much more compact, while distortions leading to the orthorhombic phase opens up open tunnels running parallel to the b axis (Figure 5.10b).

While this particular orthorhombic polymorph had not been identified previously, other orthorhombic phases have been reported. The known orthorhombic phases include $Pbc2_1$ [95], $Pnma$, and $Pbca$ [96], each shown in Figure 5.11. Both $Pbca$ and $Pnma$ are stable at elevated pressures, and phonon studies of these phases at ambient pressures have shown them to be dynamically stable [16]. The $Pbc2_1$ phase was first found in magnesium partially-stabilized-zirconia [95]. Both $Pbca$ and $Pbc2_1$ have zirconium atoms that are seven fold coordinated by oxygen, similar to monoclinic ZrO_2. The Zr atoms in the tetragonal phase, however, are eight-fold coordinated. $Pnma$, which is under the most compression, has Zr that is nine fold coordinated by oxygen. Figure 5.12 shows the volume-energy relationships between all known ZrO_2 polymorphs, along with the new $P2_12_12_1$ phase, shown as a black diamond. There is a general trend in Zr coordination number and energy levels, as 7-fold coordinated Zr phases are lower in energy, followed by the 8 fold coordinated cubic and tetragonal phases. The 9 fold coordinated orthorhombic $Pnma$ phase is the highest in energy. The volume-energy trend between cubic, tetragonal, and monoclinic is consistent with previous reports [84, 97]. There is a slight volume expansion associated with the cubic

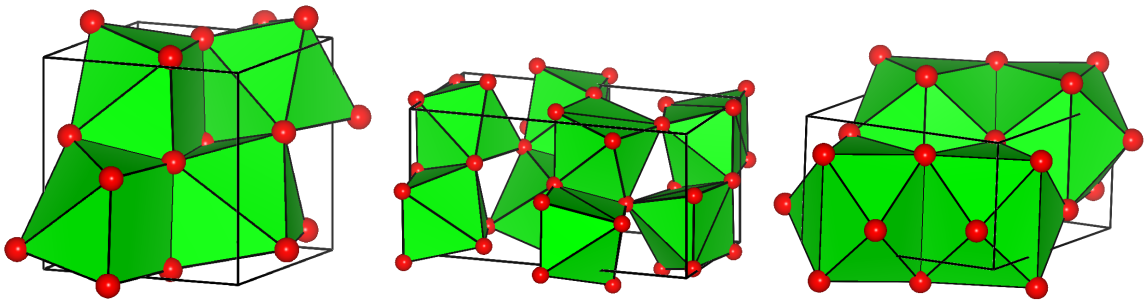

(a) **(b)** **(c)**

Figure 5.11. Known orthorhombic ZrO_2 structures: (a) $Pbc2_1$, (b) $Pbca$, and (c) $Pnma$.

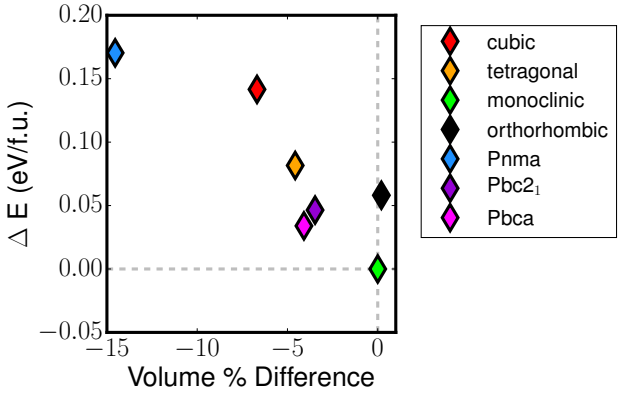

Figure 5.12. Energy-volume relationships between the known ZrO_2 polymorphs relative to monoclinic ZrO_2. The black diamond orthorhombic marker is the newly identified orthorhombic phase with a space group of $P2_12_12_1$.

to tetragonal transition. A larger volume expansion of approximately 5% accompanies the transition from tetragonal to monoclinic ZrO_2. This $P2_12_12_1$ phase is larger in volume than the tetragonal phase and is almost the same volume as the monoclinic phase. The $P2_12_12_1$ phase is, however, still approximately 60 meV/f.u. higher in energy than the monoclinic. It is possible that if the volume of the system were to expand to near monoclinic values, it would prefer to form the more energetically favorable monoclinic phase rather than the orthorhombic phase.

5.2.3 Strain Induced Instability of Tetragonal ZrO_2

In addition to volume increases, strain can also serve as a destabilizing factor in tetragonal ZrO_2. To demonstrate this effect, we use the Hencky strain metric to explore the role of strain on the relative stabilities of the different tetragonal variants. The relationship between

a strained L' and a reference L lattice can be described by the following transformation

$$L' = F \cdot L, \tag{5.4}$$

where F is the deformation gradient tensor. The deformation gradient tensor can be uniquely decomposed into rotation R and stretch U components

$$F = R \cdot U, \tag{5.5}$$

as long as the chosen U is symmetric. The Hencky strain is simply the matrix logarithm of this stretch tensor

$$H = \ln U. \tag{5.6}$$

Using the components of the Hencky strain metric

$$H = \begin{pmatrix} \epsilon_{xx} & \epsilon_{xy} & \epsilon_{xz} \\ \epsilon_{yx} & \epsilon_{yy} & \epsilon_{yz} \\ \epsilon_{zx} & \epsilon_{zy} & \epsilon_{zz} \end{pmatrix}, \tag{5.7}$$

we can define strain order parameters (SOPs) as

$$e_1 = \frac{1}{\sqrt{3}} (\epsilon_{xx} + \epsilon_{yy} + \epsilon_{zz}) \tag{5.8}$$

$$e_2 = \frac{1}{\sqrt{2}} (\epsilon_{xx} - \epsilon_{yy}) \tag{5.9}$$

$$e_3 = \frac{1}{\sqrt{6}} (2\epsilon_{zz} - \epsilon_{xx} - \epsilon_{yy}) \tag{5.10}$$

$$e_4 = \sqrt{2}\epsilon_{yz} \tag{5.11}$$

$$e_5 = \sqrt{2}\epsilon_{xz} \tag{5.12}$$

$$e_6 = \sqrt{2}\epsilon_{xy}. \tag{5.13}$$

In the infinitesimal strain limit, e_1 represents dilatational strain, while e_2 and e_3 correspond to a deviatoric strain. Within the same infinitesimal limit, e_4 - e_6 are shears. The benefit of utilizing the Hencky strain is that applying it does not change the volume with e_2-e_3 strains [98]. As Figure 5.13 shows, applying only an e_3 strain would elongate a cube along the z-axis. Straining along any of the dashed green axes in e_2-e_3 space will result in a differently oriented tetragonal lattice.

In a cubic, unstrained lattice, the three tetragonal variants x, y, and z are energetically

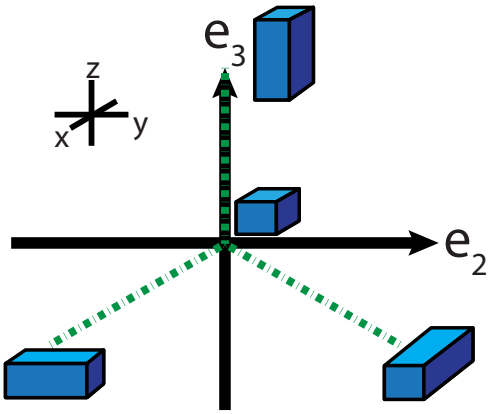

Figure 5.13. Effect of deviatoric e_2-e_3 strains on a cube. Straining along one of the three green axes will result in a different tetragonal orientation

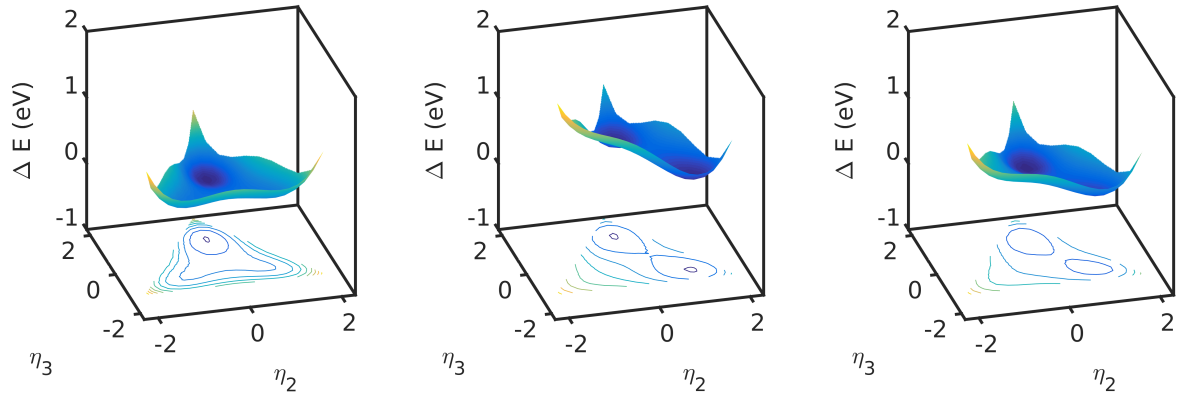

Figure 5.14. η_2-η_3 energy landscapes at various e_2-e_3. (a) Under an $e_2 = 0$, $e_3 = 0.0228$ strain, the z variant is favored. (b) An $e_2 = 0.0650$, $e_3 = 0.0375$ strain favors the z and y variants. (c) Straining by $e_2 = 0.0361$, $e_3 = 0.0292$ results in z being favored slightly over x and y.

equivalent, as Figure 5.4a showed. Applying a finite $e_3 = 0.0228$ strain such that the lattice is now tetragonally strained in the c axis direction, results in the destabilization of the x and y variants, as shown in Figure 5.14a. The z variant energy well is much lower in energy than either the x or y energy wells. Similarly, choosing an $e_2 = 0.0650$ and $e_3 = 0.0375$ strain such that the lattice is equally strained in both the x and z directions results in the energy landscape shown in Figure 5.14b, where the x and z energy wells are energetically equivalent. This strain, however, destabilizes the y variant completely. Finally, applying an $e_2 = 0.0361$ and $e_3 = 0.0292$ strain such that the lattice is strained more in the z direction than the x direction results in a deeper z shuffle well relative to the x shuffle well, as Figure 5.14c shows. From these energy landscapes, we can see that strain can effectively destabilize certain tetragonal variants and dictate the preferred tetragonal orientations.

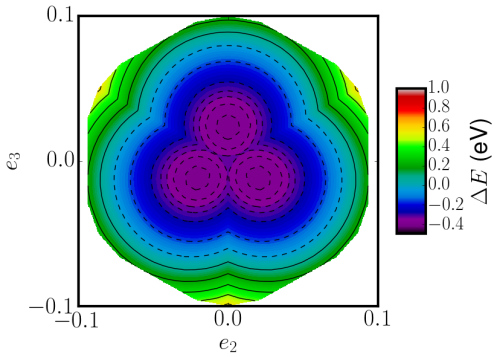

Figure 5.15. Contour plot of tetragonal internal shuffle landscape at tetragonal e_1.

As Figure 5.14 showed, strain can affect the stabilities of the tetragonal variants. Its effect under deviatoric strain can be seen by applying an e_2-e_3 strain to cubic lattices with x, y, and z internal shuffles, allowing full internal relaxations, and taking the minimum energy landscape. A contour of the resulting energy landscape is shown in Figure 5.15. Each of the three minima falls on one of the three tetragonal orientation axes in Figure 5.13 and corresponds to a different tetragonal shuffle variant. The local maximum at the origin corresponds to a cubic internal ordering in a cubic, unstrained lattice, which is consistent with previous results showing the metastability of the cubic phase.

5.2.4 Instabilities of Tetragonal and Monoclinic Under Strain

As the previous section showed, strains can cause a particular tetragonal orientation to be more energetically favorable, while simultaneously destabilizing another orientation. Strain has a similar effect on the stabilities of tetragonal and monoclinic. The relationship between the three ZrO_2 polymorphs can be described in terms of the SOPs e_1 - e_6. Furthermore, the strains of the tetragonal and monoclinic phases can be expressed relative to the cubic phase. Figure 5.16 shows a projection of cubic, tetragonal, and monoclinic phases in e_2-e_3 strain space. The cubic reference is the blue diamond at the origin. The z-shuffle variant of the tetragonal phase has non-zero strain order parameters $e_1 = 0.0181$ and $e_3 = 0.0228$. This particular variant corresponds to the green diamond on the e_3 axis. The other two tetragonal variants are the green diamonds on the dashed axes, which are the same tetragonal deviatoric strain axes shown in Figure 5.13. The non-zero SOPs of the monoclinic phase are $e_1 = 0.0417$, $e_2 = -0.0135$, $e_3 = 0.0209$, $e_5 = -0.1208$. The increase in e_1 relative to tetragonal is consistent with the observed volume expansion during the tetragonal to monoclinic transition. Four monoclinic variants can be derived from each tetragonal variant. Each pair of the four will have the same e_2-e_3 strains, but can have a positive or negative e_4, e_5 or e_6 shear. Because the equilibrium tetragonal and monoclinic phases have different

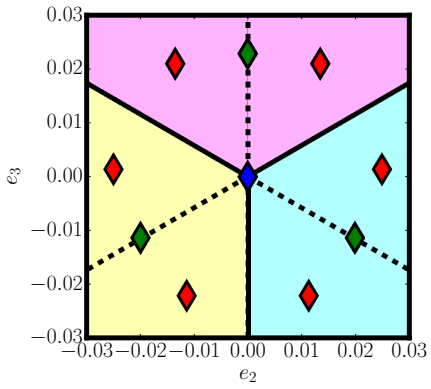

Figure 5.16. The relationship between cubic (blue diamond), tetragonal (green diamond), and monoclinic(red diamond) projected onto the e_2-e_3 space. The different trisections represent different regions in which a tetragonal variant dominates. The x, y, z regions are blue, yellow, and pink.

strains, strain is likely to have an effect on the stabilities of either phase. For example, under tetragonal SOPs, the tetragonal phase is probably more stable than monoclinic.

To explore the energetics of the transition from tetragonal to monoclinic, the nudged elastic band method was used to calculate the energy pathway. In a cubic, unstrained lattice, where all order parameters $e_1 - e_6$ are zero, both tetragonal and monoclinic are stable and separated by an energy barrier approximately 240 meV per formula unit (f.u.), as shown by the blue diamond pathway (I) in Figure 5.17. The magnitude of the energy barrier is not trivial and is unlikely to be overcome and result in a martensitic transformation. In a lattice strained by tetragonal strain order parameters, as the green curve (II) shows, the tetragonal phase is even more stable, while the monoclinic phase is metastable. This shift in energetics suggests that given a slight perturbation, a structure that has monoclinic internal distortions within a tetragonally strained lattice would easily fall into the stable tetragonal phase, lowering the energy of the system by about 150 meV per f.u. In this instance, the strain further stabilized the tetragonal phase, while destabilizing the monoclinic.

Further straining the lattice such that the dilatation and deviatoric strains $e_1 - e_3$ have the equilibrium monoclinic values results in an orthorhombic lattice where the tetragonal phase is still stable, but the monoclinic is now unstable, as seen by the red curve (III) in Figure 5.17. Imposing an e_5 shear to the lattice fully reproduces the equilibrium monoclinic lattice. The strains and shear of this monoclinic phase renders the tetragonal phase metastable and stabilizes the monoclinic phase.

As Figure 5.17 showed, the stabilities of tetragonal and monoclinic can be influenced by different strain conditions. In the cubic lattice, both tetragonal and monoclinic are stable since there is a lack of orientation preference. Tetragonally straining the lattice would naturally increase the stability of the tetragonal phase, while decreasing the stability of the

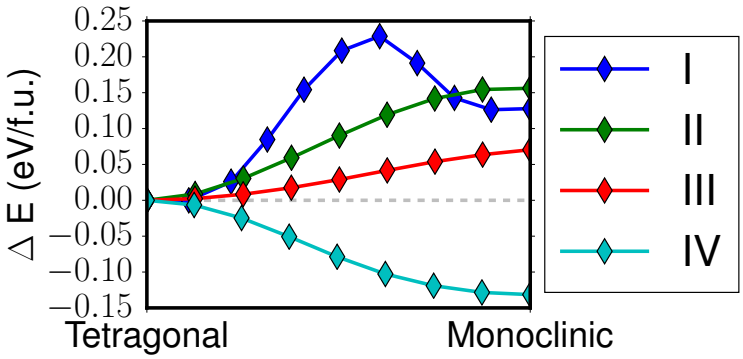

Figure 5.17. Energy barriers between tetragonal and monoclinic performed in lattices strained according to the strain order parameters of cubic (I), tetragonal (II), orthorhombic (III), and monoclinic (IV).

monoclinic phase. Although it is expected that the orthorhombic strain would decrease the stability of the tetragonal phase and make the monoclinic phase more energetically favorable, it is surprising, however, that the orthorhombic strain would destabilize the monoclinic phase. Adding the shear strain, however, subsequently stabilizes the monoclinic phase. It is apparent that while dilation and deviatoric strains alone can destabilize the tetragonal phase, the shear seems necessary to stabilize the monoclinic.

5.3 Conclusion

In this chapter, we have explored different types of instabilities in the three main ZrO_2 polymorphs. In cubic ZrO_2, we observed the dynamical instability leading to the tetragonal phase. As previous studies on cubic ZrO_2 [86, 91] and other mechanically unstable materials [69, 72] have noted, the dynamically unstable phase is likely stabilized at high temperatures by anharmonic vibrations. While the tetragonal phase is dynamically stable near equilibrium volumes, it becomes dynamically unstable at larger volumes, resulting in an orthorhombic $P2_12_12_1$ phase. Since this new phase only gradually appears at larger volumes, it is possible that thermal expansion at higher temperatures may facilitate its formation. As Figure 5.7 showed, this orthorhombic phase is energetically more favorable than the tetragonal phase. Only the tetragonal structure, however, has been experimentally observed thus far. It is possible that at larger volumes, tetragonal ZrO_2 is stabilized by anharmonic vibrations, similar to the way cubic ZrO_2 is dynamically stabilized [86, 91] and observed at high temperatures.

The volume-induced instability and anharmonicity of the tetragonal phase may have broader implications on the diffusion behavior within this high temperature material. The effect of a soft phonon mode on diffusion has been studied in the context of β-Ti. This

high-temperature BCC phase has been shown to be mechanically unstable [67], and the diffusion behavior exhibits curvature deviating from the linear Arrhenius relation [99–102]. It has been suggested that the anharmonicity of this high-temperature phase explains the non-linear diffusivity dependence on temperature [103, 104]. Köhler and Herzig report that the displacement field associated with the unstable mode serves to facilitate the diffusion mechanism within β-Ti [102]. Further studies on the diffusion behavior in tetragonal ZrO_2 with the knowledge of this anharmonicity could be performed.

The volume induced tetragonal instability had not been identified previously [14–16]. One of these studies [14], however, had reported the presence of an instability in the monoclinic phase, which we have resolved by using a significantly larger supercell in our calculations. As previous studies [14–16] used different pseudopotentials, a cursory examination using PBE and LDA pseudopotentials demonstrated a similar tetragonal instability at larger volumes, indicating that this is not a spurious result due to pseudopotential differences.

In addition to strain playing a role in stabilizing different tetragonal variants, we have seen that it can also affect the stabilities of tetragonal and monoclinic. In thin film applications, the atomic layer deposition of zirconia leads to observations of high-temperature tetragonal phases [105–107]. This phase is not expected at low deposition temperatures of $523 - 573$ K [105–107] that are well below the monoclinic-transition temperature of 1478 K. It is possible that in these thin films, the epitaxial strain stabilizes the tetragonal phase at low temperatures.

While the results of strain dependent stabilities have focused primarily on the tetragonal and monoclinic phases, anisotropic strains could be a mechanism that stabilizes the newly discovered orthorhombic phase. Further first-principles calculations can be used to determine the strains required to stabilize the orthorhombic phase at low temperatures. Armed with such insights, experimental studies involving strains can then be performed to stabilize this orthorhombic phase. Once this has been accomplished, mechanical properties testing can then be performed to determine if this phase has promise in engineering applications.

The equilibrium phase diagram provides insight into the temperature stability of the three ZrO_2 polymorphs, but there are other mechanisms through which the stabilities of each of these phases can be affected. Further studies of these different mechanisms may aid in future engineering efforts to stabilize the high-temperature tetragonal and cubic phases.

CHAPTER VI

Intercalation of Li in Trirutile $Li_{3x}Fe_2F_6$

6.1 Introduction

Recent battery research has pivoted from traditional intercalation materials such as $LiCoO_2$ and $LiFePO_4$ to displacement and conversion materials, such as CuSb and metal fluorides. Conversion materials hold great promise in that while intercalation materials are typically limited to one electron transfer per formula unit, the different valence states of the metal cation in a conversion material allows for a larger theoretical energy density. Iron fluorides FeF_2 and FeF_3 are examples of a conversion system where Li insertion causes structural changes to the host structure [108,109]. The rutile FeF_2 and perovskite FeF_3 decompose into LiF and metallic BCC Fe upon lithiation. As a first-principles study of the Li-Fe-F ternary phase diagram shows [110], of the many structural changes the occur during the lithiation, a trirutile $LiFe_2F_6$, is known to form in the early stages of conversion.

The trirutile structure is composed of three rutile-based structures stacked on top of each other. Along the *c*-axis, every two Fe octahedra are followed by one Li octahedron, forming these Fe-Li metal chains (Figure 6.1a. The octahedra are edge sharing along the *c*-axis, and neighboring chains Li-Fe octahedra are corner-sharing. There are long, empty tunnels running parallel to the c-axis, which is assumed to the primary Li diffusion pathway. In addition to the body center and corner sites of the tetragonal lattice, Li can occupy two other sites in this empty tunnel. One site is along the *a* (and symmetrically equivalent *b*) lattice edge and the other is in the center of the *a*-*c* face. Figure 6.1b shows every possible Li (green) and Li vacancy (blue) site in the unit cell.

Experimentally, a cation-disordered trirutile $LiFe_2F_6$ structure was synthesized by ball-milling stoichiometric mixtures of LiF, FeF_2 and FeF_3 [111]. As the Rietveld refinement did not present superlattice peaks characteristic of the ordering in an ideal $LiFe_2F_6$ structure, it was concluded that there was a disordered arrangement of Li and Fe [111]. Reversible

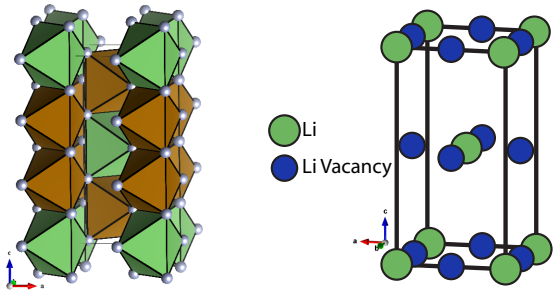

Figure 6.1. (a) Trirutile primitive structure where green and brown octahedra correspond to Li and Fe. (b) Li-vacancy sites within the primitive trirutile unit cell considered in the cluster expansion.

intercalation reaction was observed between voltages of $2.0 - 4.5$ V, corresponding to lithiation between $x = 0.1666$ and $x = 0.5333$ in $Li_{3x}Fe_2F_6$. This voltage regime stays well within intercalation regime and never advances the conversion reaction. With in-situ XRD, Liao *et al.* determined that during first discharge, Li is inserted into the empty channels that run parallel to the Li and Fe polyhedra chains. Similarly, upon charging, Li is extracted first from the channels before Li is extracted from the Li-Fe-chains [111].

In this chapter, we will examine the stable phases that form upon intercalation of Li into trirutile FeF_3 using the cluster expansion method detailed in Section 2.2.3. The resulting effective Hamiltonian will then be used in a Monte Carlo simulation to calculate the Li insertion voltage curve. Li migration barriers in the dilute regime will also be examined.

6.2 Methodology

First-principles calculations were performed using density functional theory (DFT) with the Vienna ab Initio Simulation Package (VASP) [48,49]. The calculations utilized the generalized gradient approximation (GGA) of the exchange-correlation functional as implemented by Perdew-Wang [42]. Pseudopotentials developed by the projector-augmented wave (PAW) method [47, 49] with the valence state $3p^1 3d^7 4s^1$ for Fe, $1s^1 2s^1 2p^1$ for Li, and $2s^2 2p^5$ for F were used. An energy cutoff of 550 eV was used. Brillouin zone integration was performed on a $6 \times 6 \times 6$ Γ-centered k-point mesh to achieve energy convergence to within 1 meV/atom. Full relaxations of 156 configurations with Li-Va ordering over possible octahedral sites in trirutile were performed. Ferromagnetic (FM), spin-polarized calculations were implemented since the related rutile structure FeF_2 is known to exhibit antiferromagnetic (AFM) properties below the Neel temperature 79 K [112–114].

The cluster expansion method [51, 52] was used to predict DFT formation energies of

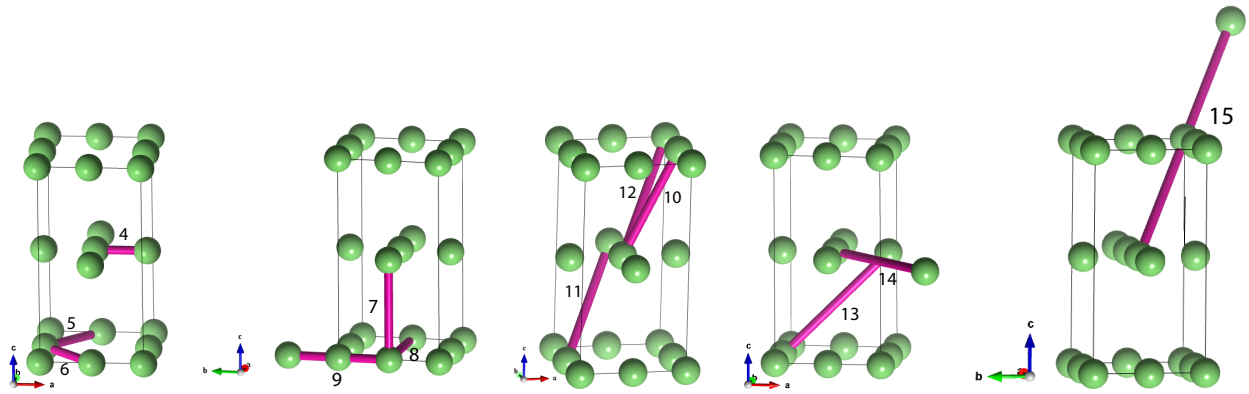

Figure 6.2. Pair clusters considered in the cluster expansion fit.

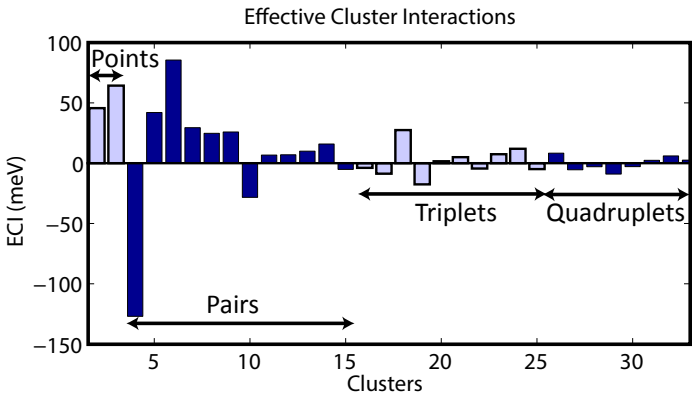

Figure 6.3. Effective cluster interactions used in the fitting of the cluster expansion.

possible Li-Va orderings in trirutile $LiFe_2F_6$ in Monte Carlo simulations to extract Li chemical potential and subsequently the voltage curve at 300 K. Possible Li-Va sites in the unit cell that were considered are shown in Figure 6.1b. A genetic algorithm [115] followed by a depth-first-search [1] was used to fit the effective cluster interactions (ECIs). A total of 33 clusters were considered: an empty cluster, 2 point clusters, 12 pair clusters, 10 triplet clusters, and 8 quadruplet clusters. The 12 pair clusters included in the fit are shown in Figure 6.2. The effective cluster interactions obtained from the fit are shown in Figure 6.3. Within each cluster size set (i.e. pairs, triplets, quadruplets), the ECIs are ordered from shortest to longest distance. The closest atoms tend to have the largest ECIs, and the interaction dies off with increases in distance. The cross-validation (CV) score, a measure of the predictive quality of the cluster expansion, was 0.041 eV per unit cell. The RMS error, which measures the ability of the model to reproduce formation energies of calculated configurations, is 0.027 per unit cell.

Li migration barriers in the dilute limit were calculated through nudged-elastic band (NEB) calculations as implemented in VASP. $2 \times 2 \times 2$ supercells of the primitive trirutile

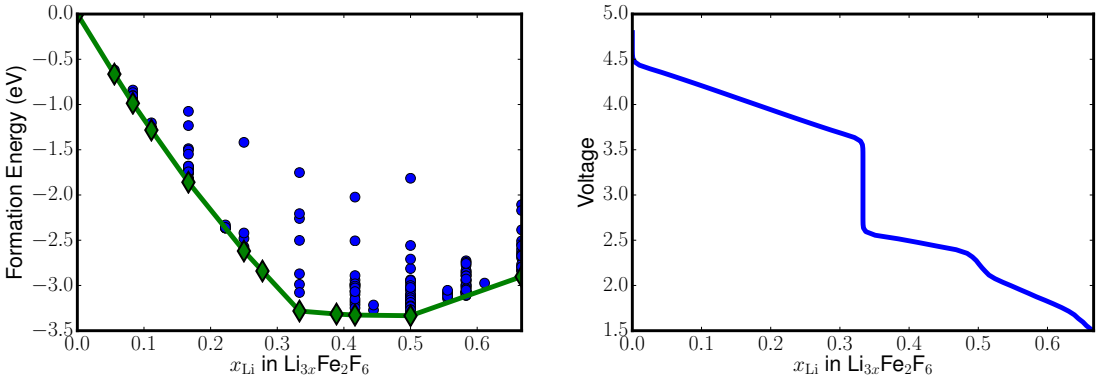

(a) **(b)**

Figure 6.4. (a) Calculated first-principles energies (blue circles) and the convex hull (green line). Stable phases that are on the convex hull are shown as green diamonds. (b) Calculated voltage curve of Li insertion into trirutile Fe_2F_6.

FeF_3 structure were used. This supercell was sufficiently large in all directions such that the Li diffusing in either the [001] or [100] directions was not influenced by its periodic image. A total of 5 images were interpolated between the initial and final states. As all NEB calculations were performed at constant volume, a lower energy cutoff of 400 eV with a Γ-centered k-point mesh of $4 \times 4 \times 4$ were used. This k-point density is commensurate with the k-point density for the primitive unit cell as calculated by a convergence test.

6.3 Results

Using the cluster expansion method, we were able to predict the stable phases formed by intercalating Li into trirutile Fe_2F_6. Figure 6.4a shows the energies of the calculated structures (blue circles) and the stable phases on the convex hull (green diamonds and line). Only concentrations up to $x = 2/3$ were considered as further lithiation will reduce the Fe valence state to less than the desired +2. There are many ordered ground states on the convex hull in the $x < 1/3$ concentration region, which will likely

The 300 K voltage curve calculated by Monte Carlo simulations is shown in Figure 6.4b. At $x = 0$, there is the fully delithiated trirutile structure (Figure 6.5) At 300 K, between concentrations of $x = 0$ and $x = 1/3$, there is a solid solution. At $x = 1/3$, the big voltage drop corresponds to the stable phase is the $LiFe_2F_6$ trirutile structure shown previously in Figure 6.1a. Further lithiation results in a stable compound $Li_{3/2}Fe_2F_6$, where Li occupies alternating levels of vacancy sites in the empty tunnels (Figure 6.5). Finally, $Li_2Fe_2F_6$ is a slightly more complex structure where Li only occupies half of the sites along the Li-Fe

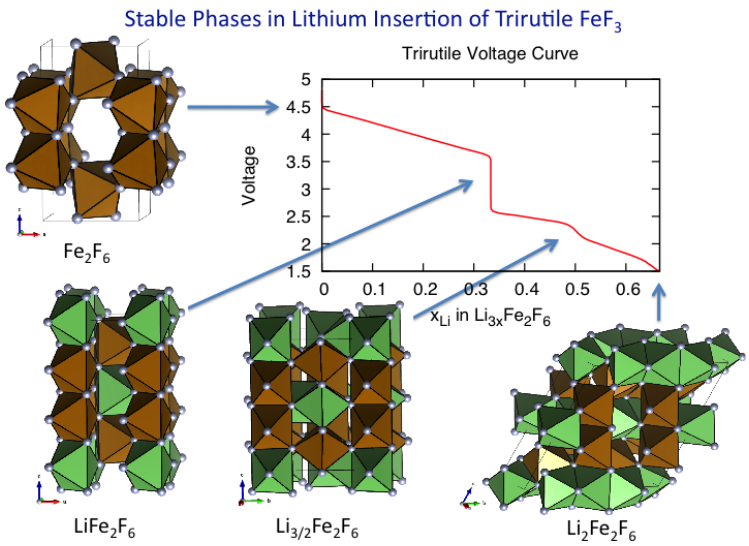

Figure 6.5. Stable phases formed upon Li insertion into trirutile Fe_2F_6.

chains, while the empty tunnels are now occupied by two Li. This configuration produces an arrangement with face-sharing Li polyhedra. These results are consistent with Liao *et al.*'s theory that the Li sites along the Fe-chain are filled before the empty tunnel sites are filled, and that upon charging, the Li in the empty tunnel are extracted before that of Fe-chains.

To understand how Li diffuses in the dilute limit, we calculated its migration barriers in the delithiated structure in Figure 6.5. The delithiated trirutile structure is open. In addition to the empty tunnels in the [001] directions, there are now open pathways in the (110) plane as well. Adding one Li atom to the supercell composed of 4 units of the delithiated primitive cell, we see that there are two symmetrically distinct hops. The first pathway is down the empty tunnels, in the [001] direction (Figure 6.6a). Similar to the lithiated $LiFe_2F_6$ trirutile structure, it is expected that Li would simply shoot through the [001] tunnels. The migration barrier for this pathway, however, is 750 meV (Figure6.6b), which is fairly high.

The second hop is within the (110) plane, where Li moves from a site in the metal chains into a tunnel site, and then back into the adjacent metal chain site (Figure 6.6c). Surprisingly enough, the barrier for this hop is 315 meV (Figure 6.6d), about half of the [001] barrier. The local minimum in the middle of the curve corresponds to the intermediate octahedral site shown as a blue polyhedron.

Examining the crystal structures of these pathways provides some insight into the difference in migration barrier magnitudes. In the [100] path, Li hops from octahedral site to octahedral site. In the metal chain sites, it is edge sharing with the Fe polyhedra both above and below. Within the same plane, it is only corner sharing with diagonal metal chains. As it moves into the octahedral site in the tunnel, it becomes edge-sharing with four

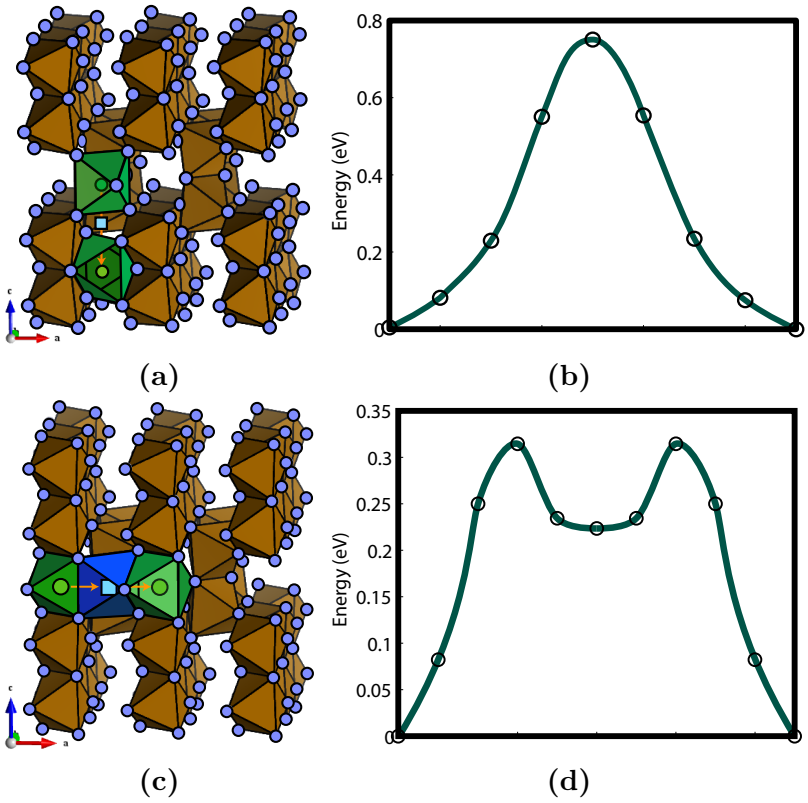

Figure 6.6. Li migration barriers in the dilute limit. (a) The [001] hop and (b) corresponding energy barrier. (c) The [100] hop, which is equivalent to the [010] hop and (d) corresponding energy barrier.

Fe polyhedra, two on each side. The [001] hop requires passing through an intermediate octahedral site that is face-sharing with two Fe polyhedra. This intermediate site is exactly midway between the initial and final states and corresponds to the barrier peak in Figure 6.6b. The electrostatic repulsions between the Fe and Li polyhedra are likely the hindering factor to Li diffusion through this path. The large differences in barrier energies suggests that Li diffusion in the dilute regime largely occurs through 2D diffusion in the (110) plane.

6.4 Conclusion

In this chapter, we performed a cluster expansion over Li-Va sites in $Li_{3x}Fe_2F_6$, which was subsequently used in Monte Carlo simulations to calculate a voltage curve. Examining the sites that Li occupy in the stable phases shows that, as Li is intercalated, it first fills up sites along the metal chain before filling up tunnel sites, as Liao *et al.* observed in their experiments [111,116]. NEB calculations indicated that Li diffusion in the dilute limit occurs largely within the (110) plane.

CHAPTER VII

Conclusion

This thesis focused primarily on the application of phonons in exploring dynamical instabilities as well as high-temperature phase stabilities. Instabilities activated by volume changes and strain were also analyzed. Dynamical properties of different materials with a wide range of applications, including Li_3OCl, δ'-ZrO, and ZrO_2, were discussed in detail. The stable phases formed during the intercalation of Li into trirutile $Li_{3x}Fe_2F_6$ were studied as well.

We found that Li_3OCl, a solid electrolyte candidate for Li-ion batteries, is mechanically unstable with respect to certain octahedral rotations. Combinations of these rotations can lead to energetically lower structures, but the energy differences between these lower symmetry and energy structures are too small to definitively identify the single most stable phase. As the energy gained from these rotational distortions are incredibly small, it is likely that even at low temperatures, the structure presents as cubic on average. In addition, we also calculated the vibrational free energies within the quasi-harmonic approximation of LiCl, Li_2O, and Li_3OCl. As Li_3OCl is dynamically unstable, we performed an estimation of its free energy and found an upper bound for the temperature at which Li_3OCl becomes entropically stabilized. We also calculated vibrational free energies within the quasi-harmonic approximation of several Zr-O phases to predict the high-temperature stability of a recently identified δ'-ZrO phase. The stabilities of oxide phases in the Zr-O system is of interest due to their applications as nuclear fuel rod cladding in water-based reactors. We found that this monoxide phase is stable at least until 1500 K, which is beyond typical nuclear reactor operating temperatures. In addition, we also updated a previously published phase diagram [1] to include both configurational and vibrational entropy.

Different types of instabilities were explored in the ZrO_2 polymorphs. The dynamical instability of cubic ZrO_2 has been shown to lead to a transformation of the tetragonal phase. Within the broader context of modeling microstructural phase transformations such as those observed in ferroelastic toughening, a framework describing both internal tetragonal shuffle

order parameters and strain order parameters was introduced. Energy landscapes showing the relative stabilities of the three tetragonal variants under different strain conditions were shown, and a strong coupling between the internal order parameters and external strain was found. In tetragonal ZrO_2, we found a dynamical instability induced by an increase in volume, which leads to a transformation into a new orthorhombic phase. Despite the presence of this instability, it is likely that the tetragonal phase is entropically stabilized by anharmonic vibrations at the high temperatures where it is observed, which is similar to how the cubic phase may be stabilized. The ability of strain to affect phase stability was extended to the tetragonal and monoclinic phases, where we found that strain can stabilize the high-temperature tetragonal phase, while simultaneously destabilizing the low temperature monoclinic phase.

Lastly, a study of trirutile $Li_{3x}Fe_2F_6$ revealed the different phases that form with Li insertion. Migration barrier calculations in the dilute limit also indicate that Li diffusion likely occurs in a 2-D manner in the (110) planes, rather than through the empty tunnels in the [001] direction.

In each of these material systems, there are different properties and aspects that can be further explored. For example, the dynamical stabilities and phase stabilities of the broader family of super-conducting antiperovskites will likely be studied to aid engineering efforts to maximize the ionic conductivities. Further research in this area will help efforts to make solid electrolytes competitive with liquid electrolytes, thus improving the safety of Li-ion batteries for use in applications such as electric cars. In the studies on Li_3OCl and ZrO_2 in particular, we found these materials to have a degree of anharmonicity, which were not accounted for in our quasiharmonic models. Although we made approximations of the effects of anharmonicity, there have been studies of other materials that required more involved anharmonic Hamiltonians combined with Monte Carlo simulations. Future studies on the role of anharmonicity and instabilities on diffusion will prove interesting in both Li_3OCl and tetragonal ZrO_2, as a relationship between diffusion and anharmonicity has been observed in β-Ti [102–104].

Studies of oxygen diffusion in the novel δ'-ZrO phase will lead to a better understanding of the oxidation mechanisms in zirconium alloys. As we have suggested, if oxygen diffusion proves difficult in δ'-ZrO, engineering zirconium alloys with a thick δ' phase may improve the oxidation resistance. Further calculations of the anisotropic strain required to stabilize the new orthorhombic ZrO_2 phase is necessary before experiments are carried out. Certain properties, such as the bulk modulus, can also be calculated. If these properties indicate that the orthorhombic phase has useful properties for engineering applications, the calculations can motivate and inform experiments on methods to stabilize the phase.

The quasi-harmonic approximation used to calculate the thermodynamic properties were computationally expensive and intensive, even with current computational capabilities. This is particularly true when incorporating vibrational effects into a phase diagram with several different ordered phases to consider. With further improvements in computing speed and efficiency of first-principles algorithms, however, these types of calculations will likely become increasingly common and routine.

As we have demonstrated in this thesis, dynamical properties can provide useful insight into the phase stabilities and phase transformations of materials with very different applications. Studies of these vibrational properties can lead to a very fundamental understanding of the underlying physics that affect the stabilities of these materials. While the emphasis here has been on ionic materials, the versatile methodologies and concepts used here can be applied to other types of materials as well.

APPENDICES

APPENDIX A

Phonons Implementation

A.1 Finding Perturbation Directions

The choice of perturbation directions in the direct approach is important as it produces the input required for determining force constants. While there are an infinite number of perturbation directions, a straightforward and relatively brute-force approach is to enumerate positive and negative perturbations along each Cartesian direction, and calculate all the forces resulting from those 26 perturbations. Symmetry of the crystal, however, will result in redundancies in the forces that are obtained. Therefore, it is possible to use symmetry to predetermine the minimum set of perturbations necessary for a complete description of the force constants [34]. In a perfectly relaxed crystal in which all lattice parameters and atom positions are optimized, there should be zero forces in the crystal. In real DFT computations, however, there are often residual forces in the unperturbed crystal. This is particularly true for crystals with lower than cubic symmetry. Because of the presence of these residual forces, it is common that additional perturbations are required to compensate for the bias.

To select the optimal set of perturbation directions, we begin by defining the asymmetric unit of a crystal, which is the smallest subset of atoms that can fully reproduce the crystal by application of symmetry. Perturbations of each of the atoms in the asymmetric unit, rather than in the entire crystal, is sufficient to obtain accurate force constants. The method described here results in as few as 1 and as many as 6 perturbation directions per asymmetric unit site. To begin, for each asymmetric unit site, of the 26 perturbation directions, only the symmetrically distinct ones are kept. For each unique perturbation, symmetrically equivalent directions are generated using the point group of the asymmetric unit site. If the symmetrically equivalent directions span all of space, which is verified by checking that

the rank of the matrix of these directions is 3, then this unique perturbation is kept as a valid perturbation direction. There may be more than one unique perturbation direction for which this is true, in which case, the choice of perturbation direction is left up to the user.

If there is no single perturbation that spans all of space, then the symmetrically equivalent directions with rank 2 are searched. For a single set of symmetrically equivalent directions $\{\mathbf{u}_0, \ldots, \mathbf{u}_d\}$, the cross product between the initial perturbation direction $\mathbf{u}_0$ and subsequent directions $\mathbf{u}_d$ are calculated. If the cross product result is a zero vector, the two perturbation directions $\mathbf{u}_0$ and $\mathbf{u}_d$ are parallel and span the same space. If the cross product $\mathbf{u}_0 \times \mathbf{u}_d$ is non-zero, then the two vectors $\mathbf{u}_0$ and $\mathbf{u}_0 \times \mathbf{u}_d$ span all of space, and those directions are used.

The negative perturbation direction, i.e. the opposite direction, is also included by default. Perturbations in the positive and negative directions within a harmonic potential should be equivalent as the energy landscape is symmetric. A potential energy surface that is asymmetric, however, has odd-order terms. Inclusion of negative directions, in addition to the positive directions, removes odd-order effects. The negative directions are a way to address the problem of residual forces, which are first-order effects.

A.2 Determining Force Constants with a Clusters-Based Approach

In predicting the phase stability of alloying compounds with respect to configurational disorder, a widely used approach has been the cluster expansion, which is discussed in Section 2.2.3. The foundation of the cluster expansion formalism is in describing configurational degrees of freedom of a crystal in terms of smaller collection of atoms, or clusters, starting from a point cluster and moving on to pairs, triplets, and even quadruplets. These building blocks allow us to build a Hamiltonian based on these clusters and their interactions.

We can use this clusters-based framework in evaluating interatomic force constants, as defined in Equation 2.3. Because we are building a harmonic model, we limit ourselves to pair clusters, ignoring point, triplet, and higher-order interactions. For anharmonic descriptions, higher order terms will be necessary. As in cluster expansions, the number of unique pairs that can be enumerated in an infinite crystal is in theory infinity, but due to realistic computational limitations, and utilizing the assumption that at longer distances, the interaction decays rapidly, we can truncate our enumeration. In the case of phonons, the upper bound of this truncation will be defined by the simulation cell size. In the cluster expansion formalism, a collection of clusters that are symmetrically equivalent are referred to as belonging to the same orbit. In particular, we are interested in clusters radiating from the same site b, which we will call the pivot. As a result, our orbits will be special in that they

not only gather symmetrically equivalent clusters, the clusters in an orbit all also contain the same pivot. For simplicity, we will index clusters with η and orbits with Ω. Each orbit represents clusters of a particular length, for example, $\Omega = 0$ represents the pair cluster between an atom with itself, which we will refer to as the self-interaction pair. $\Omega = 1$ is the nearest neighbor, $\Omega = 2$ is the next nearest neighbor, etc. Because we will no longer be dealing with a single pair of atoms in the supercell, but rather all symmetrically equivalent ones as well, we will express our force constants as $\Phi_{\Omega\eta}$, where it is understood that this describes the force constant of a specific pair of atoms in a particular orbit. Force constants of clusters in the same orbit can be related by the space group of the crystal.

A basis of rank 2 tensors can be constructed such that the sum possesses the symmetry of the force constant describing the interaction between the two sites represented by η. We represent each 3×3 tensor of this basis using Λ^{δ}, where δ indexes the number of tensors in the basis. The force constant for a particular pair cluster can then be written as

$$\Phi_{\Omega\eta} = \sum_{\delta} \Gamma^{\delta}_{\Omega} \Lambda^{\delta}_{\Omega\eta}. \tag{A.1}$$

While the collection of $\Lambda^{\delta}_{\Omega\eta}$'s describe the symmetry of the force constant, using perturbations and forces, we can fit for the coefficients Γ^{δ} that will give us a force constant that accurately describes the physics between a particular pair cluster. Note that for a single orbit, while the clusters' basis tensors may take on different forms, there is a single set of coefficients for all the clusters in the orbit.

We can express the force on site b resulting from a perturbation on site b', where both sites b and b' belong to cluster η, as

$$\vec{f_b} = \sum_{\Omega} \sum_{\eta} \Phi_{\Omega\eta} u_{\Omega,\eta,b'}. \tag{A.2}$$

Following equation 2.27, we can write the self-interaction term as

$$\Phi_{0,0} = -\sum_{\Omega=1} \sum_{\eta} \sum_{\delta} \Gamma^{\delta}_{\Omega} \Lambda^{\delta}_{\Omega\eta}, \tag{A.3}$$

where we omit the orbit $\Omega = 0$ representing the self-interaction term from our summation. One common method of ensuring Equation 2.27 is satisfied is to fit for the force constants of all finite-length pairs, and subsequently setting the self-interaction force constant term to be the negative of the sum of the other pairs [26]. The fitting method presented here will ensure that this condition is enforced self-consistently. We begin by combining Equations

A.2 and A.3

$$\vec{f}_b = \Phi_{0,0} u_{0,0,b'} + \sum_{\Omega=1} \sum_{\eta} \left(\sum_{\delta} \Gamma^{\delta}_{\Omega} \Lambda^{\delta}_{\Omega\eta} \right) u_{\Omega,\eta,b'} \tag{A.4}$$

$$= -\sum_{\Omega=1} \sum_{\eta} \sum_{\delta} \Gamma^{\delta}_{\Omega} \Lambda^{\delta}_{\Omega\eta} u_{0,0,b'} + \sum_{\Omega=1} \sum_{\eta} \left(\sum_{\delta} \Gamma^{\delta}_{\Omega} \Lambda^{\delta}_{\Omega\eta} \right) u_{\Omega,\eta,b'} \tag{A.5}$$

$$= \sum_{\Omega=1} \sum_{\delta} \Gamma^{\delta}_{\Omega} \sum_{\eta} \Lambda^{\delta}_{\Omega\eta} \left(u_{\Omega,\eta,b'} - u_{0,0,b'} \right) \tag{A.6}$$

$$= \sum_{\Omega=1} \sum_{\delta} \Gamma^{\delta}_{\Omega} V_{\Omega,\delta,b'} \tag{A.7}$$

$$\tag{A.8}$$

where $V_{\Omega,\delta,b'} = \sum_{\eta} \Lambda^{\delta}_{\Omega\eta} \left(u_{\Omega,\eta,b'} - u_{0,0,b'} \right)$. This can be rewritten as a matrix equation

$$\begin{bmatrix} \vec{f}_0 \\ \vec{f}_1 \\ \vdots \\ \vec{f}_b \end{bmatrix} = \begin{bmatrix} V_{1,0,0} & V_{1,1,0} & \cdots & V_{\Omega,\delta,0} \\ V_{1,0,1} & V_{1,1,1} & \cdots & V_{\Omega,\delta,1} \\ \vdots & \vdots & \vdots & \vdots \\ V_{1,0,b'} & V_{1,1,b'} & \cdots & V_{\Omega,\delta,b'} \end{bmatrix} \begin{bmatrix} \Gamma^0_1 \\ \Gamma^1_1 \\ \vdots \\ \Gamma^{\delta}_{\Omega} \end{bmatrix}. \tag{A.9}$$

Once the forces, perturbations, and tensors are known, the coefficients Γ^{δ}_{Ω} can be solved with a least squares method.

A.3 Constrained Linear Least Squares Fitting of Force Constants

In our description of force constants in Section 2.1.1, we described several constraints that need to be imposed. These constraints can be applied during our least squares fitting via the means of well-established constrained linear least squares fitting as, for example, detailed in reference [117].

Given the matrix X filled with $\vec{V}_{\Omega,\delta_\Omega,b'}$ components and a column vector of forces, we can fit for coefficients (column vector of Γs) through a system of linear equations that take on the general form

$$y = X\beta, \tag{A.10}$$

where β is the column vector of these coefficients, y is the column vector of forces, and X

the tensor components of our force constants. Now given a constraint on β such that

$$Q'\beta = c, \tag{A.11}$$

we can find a constraint-corrected β, β_c using the following equation

$$\beta_c = R(R'X'XR)^{-1}R'X'y + \left(I_p - R(R'X'XR)^{-1}R'X'X\right)Q\left(Q'Q\right)^{-1}c. \tag{A.12}$$

Here, Q is a full rank $p \times q$ matrix and R is a $p \times (p-q)$ matrix. For Equation A.12 to be valid, not only do these matrix conditions need to be true, it is also imperative that $[QR]$ is non-singular and $R'Q = 0$. In the implementation, R is obtained by computing the kernel of Q. To verify that $[QR]$ is non-singular, the determinant is verified to be non-zero.

A.4 Units

In implementing the calculation of the dynamical matrix using VASP output, careful unit conversions to the dynamical matrix need to be applied in order to obtain a dynamical matrix where taking the square root of the eigenvalues will produce frequencies in units of THz. Of course, frequencies are also sometimes expressed in units of cm^{-1}, but we will not address that here. To begin, recall the expression for the dynamical matrix in Equation 2.13. It is straightforward to note that only quantities such as the mass of the atoms M_i, M_j, and the force constant have units, as the phase factor is unitless. In VASP, the calculated forces have units of $\text{eV}/\mathring{A}$, and the force constants $\Phi^{bb'}_{\alpha\beta}\left(\mathbf{R}_l, \mathbf{R}_{l'}\right)$ have units of $\text{eV}/\mathring{A}^2$, and the masses have units of a.m.u. The following unit conversions to the dynamical matrix need to be applied:

$$\frac{\text{eV}}{\mathring{A}^2\text{a.m.u.}} \times \frac{1.60217646 \times 10^{-19}\text{J}}{1\text{eV}} \times \frac{1\text{a.m.u.}}{1.66053886 \times 10^{-27}\text{kg}} \times \frac{\frac{\text{kgm}^2}{\text{s}^2}}{1\text{J}} \times \left(\frac{10^{10}\mathring{A}}{1\text{m}}\right)^2 = 9.6475 \times 10^{27}\frac{1}{\text{s}^2}. \tag{A.13}$$

Solving for the eigenvalues of this adjusted dynamical matrix will now give us ω^2, the angular frequency squared in terms of $1/\text{s}^2$. As phonon dispersion curves are commonly plotted in terms of just frequency ν, related to angular frequency by $\omega = 2\pi\nu$, a division by $(2\pi)^2$ is applied

$$9.6475 \times 10^{27}\frac{1}{\text{s}^2} \times \frac{1}{(2\pi)^2} = 2.4440 \times 10^{26}\frac{1}{\text{s}^2}. \tag{A.14}$$

Noting that 1/s is a Hz, and that phonon frequencies are conventionally expressed in terms of THz, we further apply a conversion factor of $1\text{THz} = 10^{12}\text{Hz}$:

$$2.4440 \times 10^{26}\text{Hz}^2 \times \left(\frac{1\text{THz}}{10^{12}\text{Hz}}\right)^2 = 244.40\text{THz}^2.$$

As a result of this added conversion factor, when we solve the dynamical matrix, we are ultimately solving for ν, and not ω, in units of THz.

As a last note of caution, whether ω or ν is used in evaluating the thermodynamic properties outlined in Section 2.1.4 only depends on whether h or $\hbar$ is used. In addition, frequencies need to be in Hz and not THz.

APPENDIX B

Entropic Stabilization of Cu_2Sb Relative to Cu and Sb

An interesting Li-ion anode candidate is Cu_2Sb, a displacement material. Contrary to conventional layered intercalation materials such as $LiCoO_2$, the charge and discharge of the battery does not solely involve the shuttling of Li ions in and out of fixed host structures. In displacement battery materials, as Li is intercalated in, another element is extruded. In Cu_2Sb, Cu is displaced [118]. In calculating the Li-Cu-Sb ternary phase diagram, Chang *et al.* discovered that while Cu_2Sb can be synthesized and remains stable at room temperatures, zero Kelvin calculations with various pseudopotentials indicated that Cu_2Sb is metastable relative to Cu and Sb [119]. In fact, with the exception of more precise hybrid functionals, Cu_2Sb had a positive formation energy relative to the pure components. A possible explanation was that Cu_2Sb is stabilized by vibrational entropy, a hypothesis easily tested with lattice dynamic calculations.

Using the quasi-harmonic approach described in Section 2.1.5, we examined the stability of Cu_2Sb relative to Cu and Sb. Harmonic phonon calculations were performed for Cu, Sb ($A7$) and Cu_2 Sb at volumes ranging from -5 % to $+5$ % of the equilibrium volume. Perturbations with magnitudes of $0.01 - 0.05\mathring{A}$ were imposed in supercells containing 32, 32, and 18 primitive cells of Cu, Sb(A7), and Cu_2Sb, respectively. Each harmonic calculation resulted in dispersion curves similar to the equilibrium volume dispersion curves shown in Figure B.1.

Having obtained Gibbs free energies at zero pressure for each of the three phases from the quasi-harmonic calculations (Figures B.1a-B.1c), the formation free energy of Cu_2Sb can be calculated as

$$\Delta G_{Cu_2Sb} = G_{Cu_2Sb} - 2G_{Cu} - G_{Sb}. \tag{B.1}$$

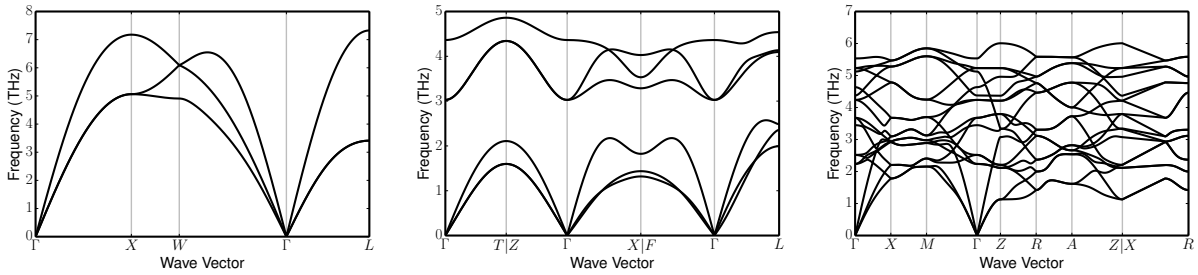

(a) **(b)** **(c)**

Figure B.**1.** Dispersion curves of (a) Cu (b) A7-Sb and (c) Cu_2Sb plotted along high symmetry directions.

As Figure B.2d shows, the temperature at which Cu_2Sb becomes stabilized is about 190 K, indicating that Cu_2Sb is stabilized by vibrational entropy.

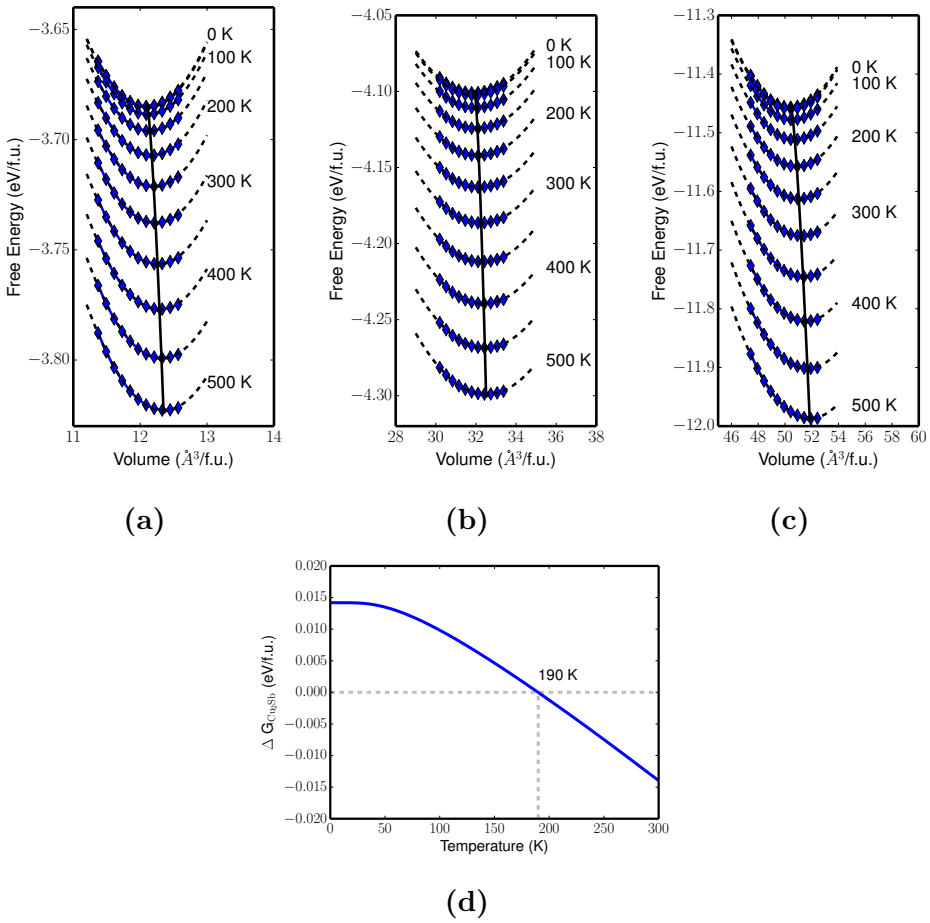

Figure B.**2.** Quasi-harmonic free energy curves for (a) Cu (b) A7-Sb and (c) Cu_2Sb. Volume-free energy curves are shown at increments of 50 K between 0 - 500 K. (d) The formation energy $\Delta G_{Cu_2Sb} = G_{Cu_2Sb} - 2G_{Cu} - G_{Sb}$ is plotted, showing that at 190 K, Cu_2Sb is stabilized relative to a decomposition to Cu and Sb.

APPENDIX C

The Effect of U on the Li-Fe-F Ternary System

While studying Li intercalation into trirutile $LiFe_2F_6$ presented in Chapter VI, we examined the broader Li-Fe-F ternary system. Iron fluoride compounds FeF_2 and FeF_3, both conversion cathode candidate materials, are known experimentally to be insulators and thus have wide bandgaps. The density of states of FeF_2 and FeF_3 were calculated using GGA Perdew-Wang pseudopotentials [42], and while FeF_3 had a negligible bandgap, FeF_2 had no bandgap. We then calculated the densities of states using DFT+U to account for the correlated electronic states around Fe. Figure C.1 shows the partial density of states of FeF_2 and FeF_3 with varying U_{eff}. As we would expect from DFT+U calculations, as the U_{eff} value is increased, so does the bandgap.

The zero-Kelvin Li-Fe-F phase diagram we calculated using PBE pseudopotentials is shown in Figure C.2 and largely agrees with one published previously by Doe *et al.* [110]. The ground states of a zero-Kelvin phase diagram calculated using PW91 pseudopotentials [120] are also consistent. As we saw, exclusion of U_{eff} values incorrectly predicts FeF_2 and FeF_3 to be metallic. We therefore calculated the Li-Fe-F ternary phase diagram with varying U values using the PW91 pseudopotential to see how the ground states may be affected. The results are shown in Figure C.2. With a value of $U_{eff} = 1$, several of the rutile-based ground states disappear. For FeF_2 to appear as a ground state, the reference state of Fe has to be raised about 2.86 eV. Changing the U_{eff} value to 2 results in many of the original ground states reappearing, and the Fe reference state only needs to be raised 0.36 eV to stabilize FeF_2. The Fe reference states of the phase diagrams with $U_{eff} = 3, 4, 5$ had to be raised by 0.3, 0.33 and 0.34 eV, respectively, in order for FeF_2 to be stabilized. Many of the other ground states, however, disappear. While the trirutile $LiFe_2F_6$ ground state is not present with $U_{eff} = 1$, it persists for $U_{eff} = 2$ up until $U_{eff} = 4$.

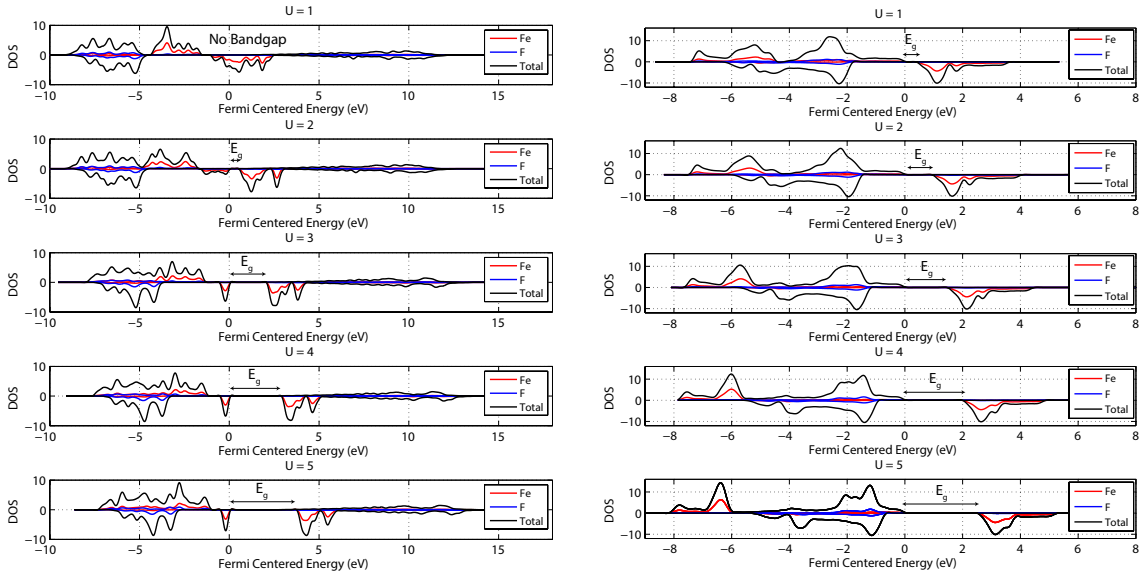

Figure C.1. Density of states of (a) FeF_2 and (b) FeF_3 with varying U values. The energy scale is centered around the Fermi level

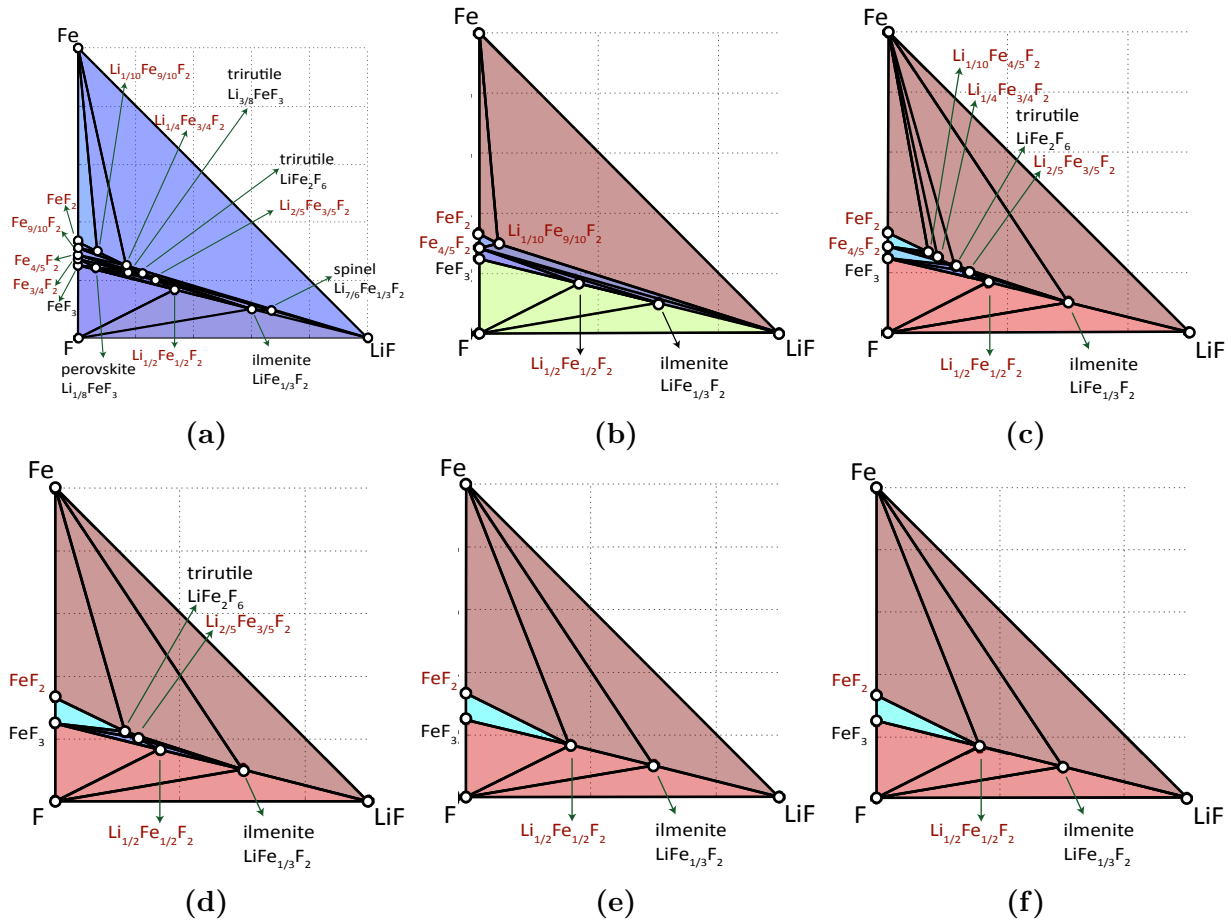

Figure C.2. The Li-Fe-F phase diagram with varying U_{eff} values: (a) $U_{eff} = 0$ (b) $U_{eff} = 1$ (c) $U_{eff} = 2$ (d) $U_{eff} = 3$ (e) $U_{eff} = 4$ (f) $U_{eff} = 5$.

BIBLIOGRAPHY

BIBLIOGRAPHY

[1] B. Puchala and A. Van der Ven, "Thermodynamics of the Zr-O system from first-principles calculations," *Phys. Rev. B*, **88**, p. 094108, (2013).

[2] J. Sanchez, F. Ducastelle, and D. Gratias, "Generalized cluster description of multicomponent systems," *Physica A: Statistical Mechanics and its Applications*, **128**, no. 12, pp. 334 – 350, (1984).

[3] D. B. Laks, L. G. Ferreira, S. Froyen, and A. Zunger, "Efficient cluster expansion for substitutional systems," *Phys. Rev. B*, **46**, pp. 12587–12605, (1992).

[4] D. D. Fontaine, "Cluster approach to order-disorder transformations in alloys," in *Advances in Research and Applications, 47* (H. Ehrenreich and D. Turnbull, eds.), vol. 47 of *Solid State Physics*, pp. 33 – 176, Academic Press, (1994).

[5] A. van de Walle and G. Ceder, "The effect of lattice vibrations on substitutional alloy thermodynamics," *Rev. Mod. Phys.*, **74**, pp. 11–45, (2002).

[6] Y. Zhao and L. L. Daemen, "Superionic conductivity in lithium-rich anti-perovskites," *Journal of the American Chemical Society*, **134**, no. 36, pp. 15042–15047, (2012). PMID: 22849550.

[7] A. Emly, E. Kioupakis, and A. Van der Ven, "Phase stability and transport mechanisms in antiperovskite Li_3OCl and Li_3OBr superionic conductors," *Chemistry of Materials*, **25**, no. 23, pp. 4663–4670, (2013).

[8] M.-H. Chen, A. Emly, and A. Van der Ven, "Anharmonicity and phase stability of antiperovskite Li_3OCl," *Phys. Rev. B*, **91**, p. 214306, (2015).

[9] B. Cox, "Some thoughts on the mechanisms of in-reactor corrosion of zirconium alloys," *Journal of Nuclear Materials*, **336**, no. 23, pp. 331 – 368, (2005).

[10] A. Motta, "Waterside corrosion in zirconium alloys," *JOM*, **63**, no. 8, pp. 59–63, (2011).

[11] K. Negita, "Lattice vibrations and cubic to tetragonal phase transition in ZrO_2," *Acta Metallurgica*, **37**, no. 1, pp. 313 – 317, (1989).

[12] K. Parlinski, Z. Q. Li, and Y. Kawazoe, "First-principles determination of the soft mode in cubic ZrO_2," *Phys. Rev. Lett.*, **78**, pp. 4063–4066, (1997).

[13] F. Detraux, P. Ghosez, and X. Gonze, "Long-range coulomb interaction in ZrO_2," *Phys. Rev. Lett.*, **81**, pp. 3297–3297, (1998).

[14] A. Kuwabara, T. Tohei, T. Yamamoto, and I. Tanaka, "Ab initio lattice dynamics and phase transformations of ZrO_2," *Phys. Rev. B*, **71**, p. 064301, (2005).

[15] M. Sternik and K. Parlinski, "Lattice vibrations in cubic, tetragonal, and monoclinic phases of ZrO_2," *The Journal of Chemical Physics*, **122**, no. 6, (2005).

[16] G. Fadda, G. Zanzotto, and L. Colombo, "First-principles study of the effect of pressure on the five zirconia polymorphs. I. structural, vibrational, and thermoelastic properties," *Phys. Rev. B*, **82**, p. 064105, (2010).

[17] M. Born and K. Huang, *Dynamical theory of crystal lattices*. International series of monographs on physics, Clarendon Press, (1954).

[18] S. Wei and M. Y. Chou, "*Ab initio* calculation of force constants and full phonon dispersions," *Phys. Rev. Lett.*, **69**, pp. 2799–2802, (1992).

[19] G. Kresse, J. Furthmller, and J. Hafner, "Ab initio force constant approach to phonon dispersion relations of diamond and graphite," *EPL (Europhysics Letters)*, **32**, no. 9, p. 729, (1995).

[20] A. van de Walle, M. Asta, and G. Ceder, "The alloy theoretic automated toolkit: A user guide," *Calphad*, **26**, no. 4, pp. 539 – 553, (2002).

[21] D. Alfé, "Phon: A program to calculate phonons using the small displacement method," *Computer Physics Communications*, **180**, no. 12, pp. 2622 – 2633, (2009). 40 YEARS OF CPC: A celebratory issue focused on quality software for high performance, grid and novel computing architectures.

[22] A. Togo, F. Oba, and I. Tanaka, "First-principles calculations of the ferroelastic transition between rutile-type and $CaCl_2$-type SiO_2 at high pressures," *Phys. Rev. B*, **78**, p. 134106, (2008).

[23] M. Born and R. Oppenheimer, "Zur quantentheorie der molekeln," *Annalen der Physik*, **389**, no. 20, pp. 457–484, (1927).

[24] R. M. Martin, "Hermitian character of the dynamical matrix - a comment on non-hermitian dynamical matrices in the dynamics of low symmetry crystals," *Solid State Communications*, **9**, no. 24, pp. 2269 – 2270, (1971).

[25] K. Negita and H. Takao, "Condensations of phonons at the tetragonal to monoclinic phase transition in ZrO_2," *Journal of Physics and Chemistry of Solids*, **50**, no. 3, pp. 325–331, (1989).

[26] N. Drummond and G. Ackland, "*Ab initio* quasiharmonic equations of state for dynamically stabilized soft-mode materials," *Phys. Rev. B*, **65**, p. 184104, (2002).

[27] L. Elcoro and J. Etxebarria, "Common misconceptions about the dynamical theory of crystal lattices: Cauchy relations, lattice potentials and infinite crystals," *European Journal Of Physics*, **32**, pp. 25–35, (2011).

[28] W. Frank, C. Elsässer, and M. Fähnle, "*Ab initio* force-constant method for phonon dispersions in alkali metals," *Phys. Rev. Lett.*, **74**, pp. 1791–1794, (1995).

[29] R. Lyddane, R. Sachs, and E. Teller, "On the polar vibrations of alkali halides," *Phys. Rev.*, **59**, pp. 673–676, (1941).

[30] W. Cochran and R. Cowley, "Dielectric constants and lattice vibrations," *Journal of Physics and Chemistry of Solids*, **23**, no. 5, pp. 447 – 450, (1962).

[31] X. Gonze and C. Lee, "Dynamical matrices, born effective charges, dielectric permittivity tensors, and interatomic force constants from density-functional perturbation theory," *Phys. Rev. B*, **55**, pp. 10355–10368, (1997).

[32] K. Parlinski, Z. Q. Li, and Y. Kawazoe, "Parlinski, li, and kawazoe reply:," *Phys. Rev. Lett.*, **81**, pp. 3298–3298, (1998).

[33] Y. Wang, S. Shang, Z.-K. Liu, and L.-Q. Chen, "Mixed-space approach for calculation of vibration-induced dipole-dipole interactions," *Phys. Rev. B*, **85**, p. 224303, (2012).

[34] S. Wei and M. Y. Chou, "Phonon dispersions of silicon and germanium from first-principles calculations," *Phys. Rev. B*, **50**, pp. 2221–2226, (1994).

[35] P. Giannozzi, S. de Gironcoli, P. Pavone, and S. Baroni, "*Ab initio* calculation of phonon dispersions in semiconductors," *Phys. Rev. B*, **43**, pp. 7231–7242, (1991).

[36] S. Baroni, S. de Gironcoli, A. Dal Corso, and P. Giannozzi, "Phonons and related crystal properties from density-functional perturbation theory," *Rev. Mod. Phys.*, **73**, pp. 515–562, (2001).

[37] D. Sholl and J. Steckel, *Density Functional Theory: A Practical Introduction*. Wiley, (2011).

[38] P. Hohenberg and W. Kohn, "Inhomogeneous electron gas," *Phys. Rev.*, **136**, pp. B864–B871, (1964).

[39] W. Kohn and L. J. Sham, "Self-consistent equations including exchange and correlation effects," *Phys. Rev.*, **140**, pp. A1133–A1138, (1965).

[40] J. P. Perdew and A. Zunger, "Self-interaction correction to density-functional approximations for many-electron systems," *Phys. Rev. B*, **23**, pp. 5048–5079, (1981).

[41] D. C. Langreth and J. P. Perdew, "Theory of nonuniform electronic systems. I. analysis of the gradient approximation and a generalization that works," *Phys. Rev. B*, **21**, pp. 5469–5493, (1980).

[42] J. P. Perdew and Y. Wang, "Accurate and simple analytic representation of the electron-gas correlation energy," *Phys. Rev. B*, **45**, pp. 13244–13249, (1992).

[43] J. P. Perdew, K. Burke, and M. Ernzerhof, "Generalized gradient approximation made simple," *Phys. Rev. Lett.*, **77**, pp. 3865–3868, (1996).

[44] J. P. Perdew, A. Ruzsinszky, G. I. Csonka, O. A. Vydrov, G. E. Scuseria, L. A. Constantin, X. Zhou, and K. Burke, "Restoring the density-gradient expansion for exchange in solids and surfaces," *Phys. Rev. Lett.*, **100**, p. 136406, (2008).

[45] J. C. Phillips and L. Kleinman, "New method for calculating wave functions in crystals and molecules," *Phys. Rev.*, **116**, pp. 287–294, (1959).

[46] M. C. Payne, M. P. Teter, D. C. Allan, T. A. Arias, and J. D. Joannopoulos, "Iterative minimization techniques for *ab initio* total-energy calculations: molecular dynamics and conjugate gradients," *Rev. Mod. Phys.*, **64**, pp. 1045–1097, (1992).

[47] P. E. Blöchl, "Projector augmented-wave method," *Phys. Rev. B*, **50**, pp. 17953–17979, (1994).

[48] G. Kresse and D. Joubert, "From ultrasoft pseudopotentials to the projector augmented-wave method," *Phys. Rev. B*, **59**, pp. 1758–1775, (1999).

[49] G. Kresse and J. Furthmüller, "Efficient iterative schemes for *ab initio* total-energy calculations using a plane-wave basis set," *Phys. Rev. B*, **54**, pp. 11169–11186, (1996).

[50] A. van de Walle and G. Ceder, "Automating first-principles phase diagram calculations," *Journal of Phase Equilibria*, **23**, no. 4, pp. 348–359, (2002).

[51] A. Van der Ven, J. C. Thomas, Q. Xu, B. Swoboda, and D. Morgan, "Nondilute diffusion from first principles: Li diffusion in Li_xTiS_2," *Phys. Rev. B*, **78**, p. 104306, (2008).

[52] A. V. der Ven, J. Thomas, Q. Xu, and J. Bhattacharya, "Linking the electronic structure of solids to their thermodynamic and kinetic properties," *Mathematics and Computers in Simulation*, **80**, no. 7, pp. 1393 – 1410, (2010). Multiscale modeling of moving interfaces in materials.

[53] N. Metropolis, A. W. Rosenbluth, M. N. Rosenbluth, A. H. Teller, and E. Teller, "Equation of state calculations by fast computing machines," *The Journal of Chemical Physics*, **21**, no. 6, pp. 1087–1092, (1953).

[54] Y. Zhang, Y. Zhao, and C. Chen, "*Ab initio* study of the stabilities of and mechanism of superionic transport in lithium-rich antiperovskites," *Phys. Rev. B*, **87**, p. 134303, (2013).

[55] Z. Deng, B. Radhakrishnan, and S. P. Ong, "Rational composition optimization of the lithium-rich $Li_3OCl_{1-x}Br_x$ anti-perovskite superionic conductors," *Chemistry of Materials*, **27**, no. 10, pp. 3749–3755, (2015).

[56] M. A. Carpenter and C. J. Howard, "Symmetry rules and strain/order-parameter relationships for coupling between octahedral tilting and cooperative Jahn-Teller transitions in ABX_3 perovskites. I. theory," *Acta Crystallographica Section B*, **65**, no. 2, pp. 134–146, (2009).

[57] A. M. Glazer, "The classification of tilted octahedra in perovskites," *Acta Crystallographica Section B*, **28**, no. 11, pp. 3384–3392, (1972).

[58] C. J. Howard and H. T. Stokes, "Group-theoretical analysis of octahedral tilting in perovskites," *Acta Crystallographica Section B*, **54**, no. 6, pp. 782–789, (1998).

[59] N. A. Benedek and C. J. Fennie, "Why are there so few perovskite ferroelectrics?," *The Journal of Physical Chemistry C*, **117**, no. 26, pp. 13339–13349, (2013).

[60] M. A. Islam, J. M. Rondinelli, and J. E. Spanier, "Normal mode determination of perovskite crystal structures with octahedral rotations: theory and applications," *Journal of Physics: Condensed Matter*, **25**, no. 17, p. 175902, (2013).

[61] K. Z. Rushchanskii, N. A. Spaldin, and M. Ležaić, "First-principles prediction of oxygen octahedral rotations in perovskite-structure $EuTiO_3$," *Phys. Rev. B*, **85**, p. 104109, (2012).

[62] G. Gou, I. Grinberg, A. M. Rappe, and J. M. Rondinelli, "Lattice normal modes and electronic properties of the correlated metal $LaNiO_3$," *Phys. Rev. B*, **84**, p. 144101, (2011).

[63] M. Gajdoš, K. Hummer, G. Kresse, J. Furthmüller, and F. Bechstedt, "Linear optical properties in the projector-augmented wave methodology," *Phys. Rev. B*, **73**, p. 045112, (2006).

[64] H. T. Stokes and D. M. Hatch, "*FINDSYM*: program for identifying the space-group symmetry of a crystal," *Journal of Applied Crystallography*, **38**, pp. 237–238, (2005).

[65] P. E. Blöchl, O. Jepsen, and O. K. Andersen, "Improved tetrahedron method for brillouin-zone integrations," *Phys. Rev. B*, **49**, pp. 16223–16233, (1994).

[66] P. V. Balachandran and J. M. Rondinelli, "Interplay of octahedral rotations and breathing distortions in charge-ordering perovskite oxides," *Phys. Rev. B*, **88**, p. 054101, (2013).

[67] K. Persson, M. Ekman, and V. Ozoliņš, "Phonon instabilities in bcc Sc, Ti, La, and Hf," *Phys. Rev. B*, **61**, pp. 11221–11224, (2000).

[68] G. Grimvall, B. Magyari-Köpe, V. Ozoliņš, and K. A. Persson, "Lattice instabilities in metallic elements," *Rev. Mod. Phys.*, **84**, pp. 945–986, (2012).

[69] W. Zhong, D. Vanderbilt, and K. M. Rabe, "Phase transitions in $BaTiO_3$ from first principles," *Phys. Rev. Lett.*, **73**, pp. 1861–1864, (1994).

[70] W. Zhong, D. Vanderbilt, and K. M. Rabe, "First-principles theory of ferroelectric phase transitions for perovskites: The case of $BaTiO_3$," *Phys. Rev. B*, **52**, pp. 6301–6312, (1995).

[71] J. Bhattacharya and A. Van der Ven, "Mechanical instabilities and structural phase transitions: The cubic to tetragonal transformation," *Acta Materialia*, **56**, no. 16, pp. 4226 – 4232, (2008).

[72] J. C. Thomas and A. Van der Ven, "Finite-temperature properties of strongly anharmonic and mechanically unstable crystal phases from first principles," *Phys. Rev. B*, **88**, p. 214111, (2013).

[73] B. Monserrat, N. D. Drummond, and R. J. Needs, "Anharmonic vibrational properties in periodic systems: energy, electron-phonon coupling, and stress," *Phys. Rev. B*, **87**, p. 144302, (2013).

[74] H. Sim and B. G. Kim, "First-principles study of octahedral tilting and ferroelectric-like transition in metallic $LiOsO_3$," *Phys. Rev. B*, **89**, p. 201107, (2014).

[75] V. Goldschmidt, "Die gesetze der krystallochemie," *Naturwissenschaften*, **14**, no. 21, pp. 477–485, (1926).

[76] R. D. Shannon, "Revised effective ionic radii and systematic studies of interatomic distances in halides and chalcogenides," *Acta Crystallographica Section A*, **32**, no. 5, pp. 751–767, (1976).

[77] T. Ahmed and L. Keys, "The breakaway oxidation of zirconium and its alloys a review," *Journal of the Less Common Metals*, **39**, no. 1, pp. 99 – 107, (1975).

[78] J. Abriata, J. Garcs, and R. Versaci, "The O-Zr (oxygen-zirconium) system," *Bulletin of Alloy Phase Diagrams*, **7**, no. 2, pp. 116–124, (1986).

[79] R. Arroyave, L. Kaufman, and T. W. Eagar, "Thermodynamic modeling of the Zr-O system," *Calphad*, **26**, no. 1, pp. 95 – 118, (2002).

[80] B. P. Burton, A. van de Walle, and H. T. Stokes, "First principles phase diagram calculations for the octahedral-interstitial system ZrO_x, $0 \leq x \leq 1/2$," *Journal of the Physical Society of Japan*, **81**, no. 1, p. 014004, (2012).

[81] N. Ni, S. Lozano-Perez, J. Sykes, and C. Grovenor, "Quantitative EELS analysis of zirconium alloy metal/oxide interfaces," *Ultramicroscopy*, **111**, no. 2, pp. 123 – 130, (2011).

[82] Y. Dong, A. T. Motta, and E. A. Marquis, "Atom probe tomography study of alloying element distributions in Zr alloys and their oxides," *Journal of Nuclear Materials*, **442**, no. 13, pp. 270 – 281, (2013).

[83] R. J. Nicholls, N. Ni, S. Lozano-Perez, A. London, D. W. McComb, P. D. Nellist, C. R. Grovenor, C. J. Pickard, and J. R. Yates, "Crystal structure of the ZrO phase at zirconium/zirconium oxide interfaces," *Advanced Engineering Materials*, **17**, no. 2, pp. 211–215, (2015).

[84] X. Zhao and D. Vanderbilt, "Phonons and lattice dielectric properties of zirconia," *Phys. Rev. B*, **65**, p. 075105, (2002).

[85] G. Ceder, "A derivation of the ising model for the computation of phase diagrams," *Computational Materials Science*, **1**, no. 2, pp. 144 – 150, (1993).

[86] C. Carbogno, C. G. Levi, C. G. Van de Walle, and M. Scheffler, "Ferroelastic switching of doped zirconia: Modeling and understanding from first principles," *Phys. Rev. B*, **90**, p. 144109, (2014).

[87] H. J. Monkhorst and J. D. Pack, "Special points for brillouin-zone integrations," *Phys. Rev. B*, **13**, pp. 5188–5192, (1976).

[88] A. V. der Ven, B. Puchala, and T. Nagase, "Ti- and Zr-based metal-air batteries," *Journal of Power Sources*, **242**, pp. 400 – 404, (2013).

[89] A. P. Mirgorodsky, M. B. Smirnov, and P. E. Quintard, "Lattice-dynamical study of the cubic-tetragonal-monoclinic transformations of zirconia," *Phys. Rev. B*, **55**, pp. 19–22, (1997).

[90] A. Mirgorodsky, M. Smirnov, and P. Quintard, "Phonon spectra evolution and soft-mode instabilities of zirconia during the c-t-m transformation," *Journal of Physics and Chemistry of Solids*, **60**, no. 7, pp. 985 – 992, (1999).

[91] S. Fabris, A. T. Paxton, and M. W. Finnis, "Free energy and molecular dynamics calculations for the cubic-tetragonal phase transition in zirconia," *Phys. Rev. B*, **63**, p. 094101, (2001).

[92] C.-J. Chan, F. F. Lange, M. Rhle, J.-F. Jue, and A. V. Virkar, "Ferroelastic domain switching in tetragonal zirconia single crystalsmicrostructural aspects," *Journal of the American Ceramic Society*, **74**, no. 4, pp. 807–813, (1991).

[93] C. Mercer, J. Williams, D. Clarke, and A. Evans, "On a ferroelastic mechanism governing the toughness of metastable tetragonal-prime (t') yttria-stabilized zirconia," *Proceedings of the Royal Society of London A: Mathematical, Physical and Engineering Sciences*, **463**, no. 2081, pp. 1393–1408, (2007).

[94] A. V. Virkar and R. L. K. Matsumoto, "Ferroelastic domain switching as a toughening mechanism in tetragonal zirconia," *Journal of the American Ceramic Society*, **69**, no. 10, pp. C–224–C–226, (1986).

[95] E. H. Kisi, C. J. Howard, and R. J. Hill, "Crystal structure of orthorhombic zirconia in partially stabilized zirconia," *Journal of the American Ceramic Society*, **72**, no. 9, pp. 1757–1760, (1989).

[96] J. E. Jaffe, R. A. Bachorz, and M. Gutowski, "Low-temperature polymorphs of ZrO_2 and HfO_2: A density-functional theory study," *Phys. Rev. B*, **72**, p. 144107, (2005).

[97] X. Zhao, D. Ceresoli, and D. Vanderbilt, "Structural, electronic, and dielectric properties of amorphous ZrO_2 from *ab initio* molecular dynamics," *Phys. Rev. B*, **71**, p. 085107, (2005).

[98] Z. Bazant, "Easy-to-compute tensors with symmetric inverse approximating Hencky finite strain and its rate," *Journal of Engineering Materials and Technology-Transactions of the ASME*, **120**, pp. 131–136, (1998).

[99] J. M. Sanchez and D. de Fontaine, "Model for anomalous self-diffusion in group-IVB transition metals," *Phys. Rev. Lett.*, **35**, pp. 227–230, (1975).

[100] N. D. Reca and y C.M. Libanati, "Autodifusion de titanio beta y hafnio beta," *Acta Metallurgica*, **16**, no. 10, pp. 1297 – 1305, (1968).

[101] A. E. Pontau and D. Lazarus, "Diffusion of titanium and niobium in bcc Ti-Nb alloys," *Phys. Rev. B*, **19**, pp. 4027–4037, (1979).

[102] U. Khler and C. Herzig, "On the anomalous self-diffusion in B.C.C. titanium," *physica status solidi (b)*, **144**, no. 1, pp. 243–251, (1987).

[103] H. M. Gilder and D. Lazarus, "Role of vacancy anharmonicity on non-arrhenius diffusional behavior," *Phys. Rev. B*, **11**, pp. 4916–4926, (1975).

[104] P. Varotsos, W. Ludwig, and K. Alexopoulos, "Calculation of the formation volume of vacancies in solids," *Phys. Rev. B*, **18**, pp. 2683–2691, (1978).

[105] S. K. Kim and C. S. Hwang, "Atomic layer deposition of ZrO_2 thin films with high dielectric constant on tin substrates," *Electrochemical and Solid-State Letters*, **11**, no. 3, pp. G9–G11, (2008).

[106] H. Kim, P. C. McIntyre, and K. C. Saraswat, "Microstructural evolution of ZrO_2-HfO_2 nanolaminate structures grown by atomic layer deposition," *Journal of Materials Research*, **19**, pp. 643–650, (2004).

[107] H. Kim, C. O. Chui, K. C. Saraswat, and P. C. McIntyre, "Local epitaxial growth of ZrO_2 on Ge (100) substrates by atomic layer epitaxy," *Applied Physics Letters*, **83**, no. 13, pp. 2647–2649, (2003).

[108] H. Arai, S. Okada, Y. Sakurai, and J. ichi Yamaki, "Cathode performance and voltage estimation of metal trihalides," *Journal of Power Sources*, **68**, no. 2, pp. 716 – 719, (1997). Proceedings of the Eighth International Meeting on Lithium Batteries.

[109] F. Badway, F. Cosandey, N. Pereira, and G. G. Amatucci, "Carbon metal fluoride nanocomposites: High-capacity reversible metal fluoride conversion materials as rechargeable positive electrodes for Li batteries," *Journal of The Electrochemical Society*, **150**, no. 10, pp. A1318–A1327, (2003).

[110] R. E. Doe, K. A. Persson, Y. S. Meng, and G. Ceder, "First-principles investigation of the Li-Fe-F phase diagram and equilibrium and nonequilibrium conversion reactions of iron fluorides with lithium," *Chemistry of Materials*, **20**, no. 16, pp. 5274–5283, (2008).

[111] P. Liao, J. Li, and J. R. Dahn, "Lithium intercalation in $LiFe_2F_6$ and $LiMgFeF_6$ disordered trirutile-type phases," *Journal of The Electrochemical Society*, **157**, no. 3, pp. A355–A361, (2010).

[112] J. Strempfer, U. Rütt, S. P. Bayrakci, T. Brückel, and W. Jauch, "Magnetic properties of transition metal fluorides MF_2 (M=Mn, Fe, Co, Ni) via high-energy photon diffraction," *Phys. Rev. B*, **69**, p. 014417, (2004).

[113] E. O. Wollan, H. R. Child, W. C. Koehler, and M. K. Wilkinson, "Antiferromagnetic properties of the iron group trifluorides," *Phys. Rev.*, **112**, pp. 1132–1136, (1958).

[114] J. M. Greneche, A. L. Bail, M. Leblanc, A. Mosset, F. Varret, J. Galy, and G. Ferey, "Structural aspects of amorphous iron(iii) fluorides," *Journal of Physics C: Solid State Physics*, **21**, no. 8, p. 1351, (1988).

[115] G. Hart, V. Blum, M. Walorski, and A. Zunger, "Evolutionary approach for determining first-principles hamiltonians," *Nature Materials*, **4**, pp. 391–394, (2005).

[116] P. Liao, R. A. Dunlap, and J. R. Dahn, "In situ mössbauer effect study of lithium intercalation in $LiFe_2F_6$," *Journal of The Electrochemical Society*, **157**, no. 10, pp. A1080–A1084, (2010).

[117] T. Amemiya, *Advanced Econometrics*. Harvard University Press, (1985).

[118] L. Fransson, J. Vaughey, R. Benedek, K. Edstrm, J. Thomas, and M. Thackeray, "Phase transitions in lithiated Cu_2Sb anodes for lithium batteries: an in situ X-ray diffraction study," *Electrochemistry Communications*, **3**, no. 7, pp. 317 – 323, (2001).

[119] D. Chang, M.-H. Chen, and A. Van der Ven, "Factors contributing to path hysteresis of displacement and conversion reactions in Li ion batteries," *Submitted*, (2015).

[120] F. Wang, H.-C. Yu, M.-H. Chen, L. Wu, N. Pereira, K. Thornton, A. der Ven, Y. Zhu, G. G. Amatucci, and J. Graetz, "Tracking lithium transport and electrochemical reactions in nanoparticles," *Nature Communications*, **3**, (2012).